DEPARTAMENTO DE ASTROFISICA

Universidad de La Laguna

Naturaleza de Estrellas Calientes de Rama Horizontal en Cúmulos Globulares Galácticos

On the nature of hot horizontal branch stars in Galactic globular clusters.

Tesis doctoral presentada por
Alejandra Recio Blanco
Directores de tesis:
Antonio Aparicio Juan y Giampaolo Piotto

Directores de tesis:

- Prof. Giampaolo Piotto
  Dipartimento di Astronomia
  Università di Padova, Padova, Italia

- Prof. Antonio Aparicio Juan
  Departamento de Astrofísica
  Universidad de La Laguna, Tenerife, España

Resumen

El objetivo de esta tesis es el estudio de las estrellas calientes de rama horizontal (HB) en cúmulos globulares Galácticos. Estas estrellas, cuyo origen aún es objeto de debate, pierden, en la fase de gigante roja, hasta dos veces más masa que las estrellas normales de HB y pueblan las llamadas colas azules en los diagramas color-magnitud de los cúmulos globulares. Pueden alcanzar temperaturas de hasta 35000 K y se cree sean las responsables del exceso ultravioleta en las galaxias elípticas.

En primer lugar, se ha analizado, mediante espectroscopía de alta resolución con UVES+VLT, las características rotacionales de 61 estrellas de HB, con temperaturas effectivas, T_{eff}, entre 7000 K y 25000 K, pertenecientes a los cúmulos M15, M79, M80 y NGC 2808. Dicho estudio ha revelado la existencia de una discontinuidad en la distribución de la velocidad de rotación con la temperatura: las estrellas con $T_{eff} < 11000$ K alcanzan valores de $v\sin i$, la velocidad de rotación proyectada, de hasta 30 km/s. Por su parte, las estrellas con $T_{eff} > 11000$ K presentan sólo valores de rotación lenta ($v\sin i < 8$ km/s). Esta discontinuidad parece coincidir con el comienzo de los procesos difusivos en la atmósfera de la estrella, que dan lugar a anomalías de abundancias en las estrellas más calientes: sobreabundancias de metales y disminución del helio. Asílo demuestra también el análisis realizado de las abundancias químicas de 10 de las estrellas observadas en el cúmulo M79, donde se han encontrado signos de levitación radiativa de metales y sedimentación gravitacional de helio a temperaturas superiores a 11000 K.

En segundo lugar, con el objetivo de descifrar el origen de las estrellas calientes de HB (el llamado problema del segundo parámetro), se ha estudiado la dependencia de la extensión en temperatura de la rama horizontal con los distintos parámetros del cúmulo. Mediante un análisis multivariable de 63 diagramas color-magnitud, basados en fotometría B, V con el Hubble Space Telescope, se ha encontrado que dicha extensión en temperatura depende, no

sólo de la metalicidad del cúmulo, como ya predicho por los modelos canónicos de evolución estelar, sino tambien, en manera considerable, de la luminosidad total de éste, dejando abierta la posibilidad de otras dependencias de grado inferior. Por último, como subproducto de la fotometría de campo amplio realizada para la seleción de los candidatos espectroscópicos, se ha encontrado una característica nueva de la rama horizontal extendida del cúmulo NGC 6752: un salto de luminositad en las estrellas con $T_{eff} > 23000$ K.

Abstract

The goal of this thesis is to study the nature of hot horizontal branch (HB) stars in Galactic globular clusters. These stars, whose origin is still under debate, loose up to a factor of two more mass than normal HB stars, during the red giant branch phase, and populate the so called blue tails in the colour-magnitude diagramms of globular clusters. They can reach temperatures up to 35,000 K and they are now considered the prime contributors to the ultraviolet emission in elliptical galaxies.

In the first part of the thesis, we have analized the rotational properties of 61 HB stars in the clusters M15, M79, M80 and NGC 2808, with effective temperatures, T_{eff}, between 7000 K and 25000 K. To this purpose, we have used high resolution spectroscopy with UVES+VLT. Our study has revealed the existence of a discontinuity in the rotational rate distribution with temperature: stars with $T_{eff} < 11000$ K show a range of $v\sin i$ values (the projected rotational velocity) up to 30 km/s. However, all the stars with $T_{eff} > 11000$ K are slow rotators, with $v\sin i < 12$ km/s. This discontinuity seems to coincide with the onset of diffusive processes in the stellar atmosphere, which cause abundance anomalies in the hotter stars: overabundances of metals and helium depletion. This is confirmed also by the chemical analysis performed in 10 of our M79 targets, in which we have found evidences of radiative levitation of metals and gravitational settling of helium, for stars with temperatures hotter than 11000 K.

In the second part of the thesis, trying to disentangle the origin of hot HB stars (the so called second parameter problem), we have investigated the dependence of the HB temperature extension on the different cluster parameters. A multivariate analysis of 63 colour-magnitude diagrams based on Hubble Space Telescope B, V photometry has been performed. We find that such HB temperature extension depends, not only on cluster metallicity, as already predicted by canonical stellar evolution models, but also, in a sizeable way, on

its total luminosity (with more luminous clusters having longer HBs) and on the collisional parameter (with cluster with higher collision rates having longer HBs).

Finally, as a by-product of the wide field photometry performed for spectroscopic target selection, we have found a new feature along the extended horizontal branch of NGC 6752: a luminosity jump for stars with $T_{eff} > 23000$ K.

Contents

Resumen **v**

Abstract **vii**

1 Introduction. **1**

I Theoretical and observational framework. **5**

2 Hot Horizontal Branch stars **7**

2.1 Globular Cluster Horizontal Branches: general review. 8

2.1.1 The evolutionary context. 8

2.1.2 Hot HB stars and the second parameter problem. 9

2.2 The recent observational framework 16

2.2.1 Stellar distributions along HB Blue Tails 16

2.2.2 Atmospheric Parameters: effective temperature and gravities. 19

2.2.3 The luminosity jump in blue bands. 20

2.2.4 Abundance variations along the HB. 22

2.2.5 Rotational velocity distribution of HB stars. 24

2.2.6 Binary frequency in the blue HB. 25

2.2.7 Tilted HBs in metal-rich clusters. 27

2.2.8 Hot HB stars and the UV excess in elliptical galaxies. . . 28

II Spectroscopy: Rotation and abundances of Hot Horizontal Branch Stars **31**

3 Target selection: observations and data reduction. **33**
3.1 Target selection 33
3.1.1 Colour-magnitude diagrams and finding charts. 35
3.2 UVES+VLT spectroscopy: observations and reduction. 35
3.2.1 Instrument configuration and observing runs. 35
3.2.2 Reduccion 36

4 Analysis procedures: rotation and abundances. **43**
4.1 Rotational velocity measurements 43
4.1.1 Cross-correlation analysis 43
4.1.2 Projected rotational velocity measurements 45
4.2 Abundance measurements 47
4.2.1 Line selection, oscillator strengths, and solar abundances 48
4.2.2 Equivalent Widths 48
4.2.3 Atmospheric parameters 49

5 Results and Discussion. **55**
5.1 Rotational velocity. 55
5.1.1 Results. 55
5.1.2 Distribution of rotational velocity along the blue HB and from cluster to cluster. 59
5.2 Abundance measurements. 60
5.3 Theoretical implications. 64

III Photometric Properties of Hot Horizontal Branch Stars 77

6 HST data: searching for the second parameter. **79**
6.1 The database. 79
6.2 Observations and pre-reduction of the images 80
6.3 Reduction procedures. 85
6.3.1 Instrumental magnitudes 85
6.3.2 The correction for CTE 87
6.3.3 Transformation to the standard photometric systems . . 88
6.4 What determines the HB morphology in globular clusters? . . . 89
6.4.1 Determination of effective temperature along the HBs. . 91
6.4.2 Considered cluster parameters. 97
6.4.3 Monovariate correlations. 98
6.4.4 A multivariate approach. 102

6.5 Summary and discussion: theoretical implications. 106

7 A new feature along the BT of NGC6752. 125
7.1 Observations and data reductions. 125
7.2 The Colour-Magnitude Diagrams. 126
7.3 The second jump. 129

IV Conclusions and Future Work. 133

8 Conclusions and Future Work. 135
8.1 Conclusions. 135

V Appendix : Abundance measurements 137

Bibliography 157

1

Introduction.

GLOBULAR clusters are gravitationally bound concentrations of approximately ten thousand to one million stars, spread over a volume of several tens to about 200 light years in diameter. Globular clusters (GCs) are the closest approximation to a physicist's laboratory in astronomy. Their properties (i.e. luminosity, mass, central concentration and chemical composition) cover a wide range of values. They account for $\sim \frac{1}{1000}$ of the Galaxy total mass (Hut et al. 1992) and their orbits show remarkable differences (Djorgovski 1993).

The first discovered globular cluster, although mistaken for a nebula, was M22 in Sagittarius, probably identified by Abraham Ihle in 1665. M22 was followed by the southern Omega Centauri (NGC 5139) discovered by Edmond Halley in 1677 on his journey to St. Helena. This "nebula" had been known since ancient times but classified as a star. Next followed the discovery of M5 in Serpens Caput by Gottfried Kirch in 1702, and that of M13 in Hercules, again by Halley, in 1714. Charles Messier was the first to resolve into single stars one globular cluster, M4. By the time William Herschel started his comprehensive deep sky survey with large telescopes in 1782, 33 globular clusters were already known. Herschel discovered 37 new globulars, bringing the number of known globulars to 70. He also resolved virtually all of them into stars, and coined the term "globular cluster". All these early known globulars belonged to our Milky Way Galaxy, with the exception of M54, presumably belonging to the Sagitarius dwarf spheroidal (Ibata, 1994). We currently know about 150 Milky Way globular clusters, 147 of them included in the W.E. Harris'1999 database.

Globular cluster's dimensions are small compared to their distances from us: half of the light is generally emitted within a radius of less than 10 pc, whereas the closest globular cluster (M4) is at distance of 2 kpc, and 90 % of

them lie more than 5 kpc away. We can thus safely assume that all stars within a globular cluster lie at the same distance from us. Moreover, because of their luminosity, they trace the structure of the Galactic halo up to large distances (Zinn, 1985) and can be used as extragalactic distance indicators. Contrary to the Galactic field, GCs formed stars only once in the beginning. Since the duration of that star formation episode is short compared to the current age of the globular clusters, the stars within one globular cluster can be considered essentially coeval. In addition, all stars within one GC, with few exceptions, show the same initial abundance pattern, which may differ from one cluster to another.

Therefore, GCs are comprised of chemically homogeneous and coeval populations of stars, and they represent excellent systems for testing stellar models. The various sequences that appear in a cluster's colour-magnitude diagram (CMD) can be compared to the predicted isochrones and theoretical loci. In this way, the properties of stars at different stages of evolution, and fundamental characteristics of the clusters themselves, such as cluster distance and age, can be derived. With ages of the order of 10^{10} years, globlular clusters are the brightest fossils of our galaxy formation epoch. They are thought to be made up of the oldest stars of the Universe for which we can measure an age, so they can shed some light on the processes of formation and evolution of galaxies. On the other hand, the determination of their ages gives a lower limit to the age of the Universe (Fall & Rees 1985). For all these reasons, it is not surprising that the study of GCs has played a pivotal role in the development of stellar astrophysics.

The stellar population of globular clusters is the target of the present thesis. In particular, I will focus on one evolutionary stage: the horizontal branch (HB). HB stars are characterized by core-helium burning and shell-hydrogen burning. The star location in effective temperature along the Zero Age Horizontal Branch (ZAHB) depends on virtually all stellar parameters (composition, age, rotation, etc..., see e.g. Rood 1973). The wide colour distribution of the HB, called the HB morphology, *is the result of large differences in the envelope mass of stars having the same core mass, at the same evolutionary stage.* The HB behaves as an amplifier, displaying the record of both initial conditions and of any variations and perturbations in the evolution of the star from its birth up to the HB stage. Hence, reading properly the HB morphologies can yield a better understanding of Population II stellar evolution in general, and the specific stellar systems, clusters or galaxies, in particular.

However, it appears that our comprehension of the HB phase and its precursors is incomplete. Canonical stellar theory can not adequately explain the wide variety of HB morphologies observed in Galactic GCs, ranging from short

red HBs to long extended "blue tails". In particular, blue tails still represent a puzzle in the stellar evolution model, in the sense that we know what the stars in blue tails are, but we do not know how stellar evolution can create them. These hot blue HB stars have lost a significant fraction of their envelopes, up to a factor with respect to "normal" HB stars. For this reason, they allow us to gain insight of their internal structure and dynamics. Understanding the origin of hot HB stars is not only important for our fine-tuning the stellar evolution theory, as it has a more general relevance in astrophysics. Indeed, these stars are now considered to be the prime contributors to the ultraviolet emission in elliptical galaxies (Greggio & Renzini 1990; Brown et al. 2000). Furthermore, hot HB stars play an important role in population synthesis of extragalactic *non resolved* systems; as these *old* hot stars can be easily confused with *young* hot stellar population. For the same reason, they can also affect the modeling of the star formation history in dwarf galaxies of the Local Group, which tries to reproduce their colour-magnitude diagrams (Tolstoy et al. 1998).

The primary aim of this thesis is to cast some light on the nature of hot horizontal branch stars in Galactic globular clusters. Physical properties, such us rotation rates, abundances, temperature and mass distribution, of a representative sample of hot HB stars are analyzed. To this purpose, high resolution spectroscopy with the Very Large Telescope (VLT), Space Telescope (HST) photometry are used.

In chapter 2 we provide the evolutionary context of horizontal branch and prior observational work on blue HB stars. Chapters 3 and 4 describe the spectroscopic observations, analysis procedures and final results on rotational velocity and abundance measurements. Chapters 4 and 5 present the photometric data and their analysis. Finally, in chapter 6 I summarize the findings and their implications, and offer some suggestions for future research.

.

Part I

Theoretical and observational framework.

2

Hot Horizontal Branch stars

In 1900, Barnard published the detection of globular cluster stars that were much brighter on blue-sensitive photographic plates than visually: "*Of course the simple explanation of this peculiarity is that these stars, so bright photographically and so faint visually, are shining with a much bluer light than the stars which make up the main body of the clusters.*"

A few years later, Shapley, found a double-peaked distribution of colours in the cluster M3, with a red maximum and a blue secondary peak (Shapley, 1915b). He reported that, at variance with the field dwarf main-sequence stars, the stars in M3 became bluer as they became fainter. Later on, Ten Bruggencate (1927) used Shapley's data to plot magnitude versus colour, finding the existence of a *red giant branch*, becoming bluer toward fainter magnitudes, and, in addition, the presence of a *horizontal branch*, extending far to the blue at constant brightness from the red giant branch.

Therefore, the existence of hot horizontal branch stars in globular clusters was noticed since the first colour-magnitude diagrams were produced. However, as pointed out in the Introduction, many questions about their nature and their origin remain unsolved. In the following sections, the observational and theoretical context on hot horizontal branch stars will be presented. For an extense review on hot stars in globular clusters see Moehler (2001), from which many of the citations in this chapter are taken.

The discovery of hot horizontal branch stars in globular clusters is

2.1 Globular Cluster Horizontal Branches: general review.

2.1.1 The evolutionary context.

Soon after being formed, a star regulates it's internal density and temperature structure until fusion of hydrogen into helium in the stellar core provides a rate of energy production enough to support itself against gravitational contraction. Over approximately the 90% of a star's total lifetime is spent in the Main Sequence phase. During this stage, the star gradually becomes more luminous and slightly hotter, in response to the changing chemical structure of its interior. The stellar evolution of the stars after the Main Sequence is very different depending on the mass of each star. In the following, we will concentrate in low mass stars, which are the only ones still alive in globular clusters. After the available hydrogen fuel at the center is exhausted , the inert helium core, containing some 10% of the star's mass, shrinks to a volume of about the dimension of the Earth. A thin shell around the core is heated up by the core's contraction, until its temperature reaches the hydrogen burning ignition. Due to the energy generation in the H-burning shell, the outer layers of the star expand and their temperature decreases. This large but cool star is now a red giant, with a surface temperature of 3500 degrees and a radius of about 100 solar radii. The helium core contracts until its temperature reaches about 100 million degrees. At this point, helium burning ignites in degenerated conditions, producing the so-called helium flash.

Hoyle & Schwarzschild (1955) were the first to identify the horizontal branch stars with post-red giant branch stars that burn helium in the central regions of their cores. But horizontal branch morphology was discovered to change quite considerably from cluster to cluster, as the number of analized CMDs increased. Arp (1955) studied clusters which exhibited blue HB extensions toward bluer colours and fainter visual magnitudes, i.e. toward hotter temperatures. The change in slope of the HB toward higher temperatures is caused by, on one hand, the decreasing sensitivity of $(B-V)$ to temperature and, on the other hand, by the increasing bolometric correction for hotter stars. For effective temperatures higher than 10.000 K the ultraviolet radiation constitutes the main part of the energy flux coming from the stellar surface, making stars fainter in V, and the HB, in practice, vertical in the classical V vs. $(B-V)$ plane. Figure 2.1 shows the CMD of NGC 2808 with the names of the principal evolutionary sequences of low mass stars, from the Main Sequence (MS) to the White Dwarf sequence.

Sandage & Wallerstein (1960) reported a correlation between the metal abundance and the horizontal branch morphology seen in globular cluster CMDs: **the horizontal branch (HB) becomes bluer with decreasing metallicity**, the so called first parameter. This result follows quite naturally from

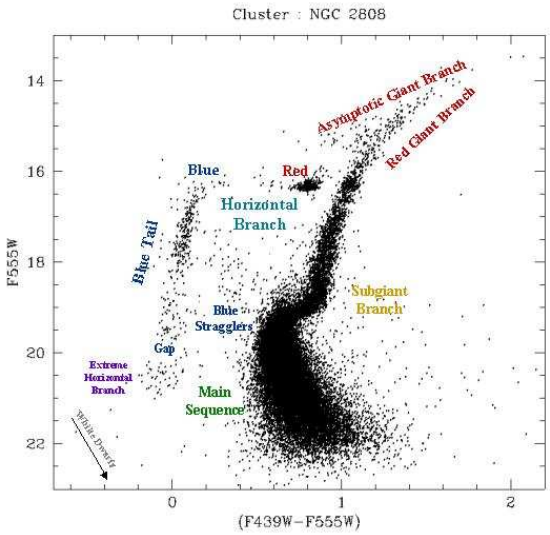


FIGURE 2.1— The CMD of NGC 2808 (from Piotto et al. 2002) with the names of the principal sequences: main sequence (MS), subgiant branch (SGB), red giant branch (RGB), red and blue horizontal branch (HB), blue tail (BT), extreme horizontal branch (EHB), asymptotic giant branch (AGB) and white dwarfs.

canonical models. A more metal-rich envelope would present a larger opacity per unit mass, and will expand to a larger radius, decreasing the surface temperature. Therefore, metal-rich clusters should have only a red HB. An example of the first parameter effect in shown in Figure 2.2, which contrasts the CMDs of three typical clusters: a metal-poor one, an intermediate-metallicity one, and a metal-rich one.

2.1.2 Hot HB stars and the second parameter problem.

For the first time, Faulkner (1966) succeeded in reproducing the trend of HB morphology with metallicity. He computed zero-age HB (ZAHB) models, without taking into account any mass loss, and adopting a rather high helium abundance (Y = 0.35). In fact, **ZAHB models are bluer with increasing helium abundance**, since a higher helium fraction (and thus a lower hydrogen fraction) contributes fewer electrons per unit mass to the stellar envelope. The lower ensuing opacity leads to a smaller stellar radius and thus a bluer colour.

Iben & Rood (1970), however, found that "*for the values of Y and Z most favored (Y 0.25 0.28, Z = 10^{-3} 10^{-4}), individual tracks are the stubbiest. We can account for the observed spread in colour along the horizontal branch by*

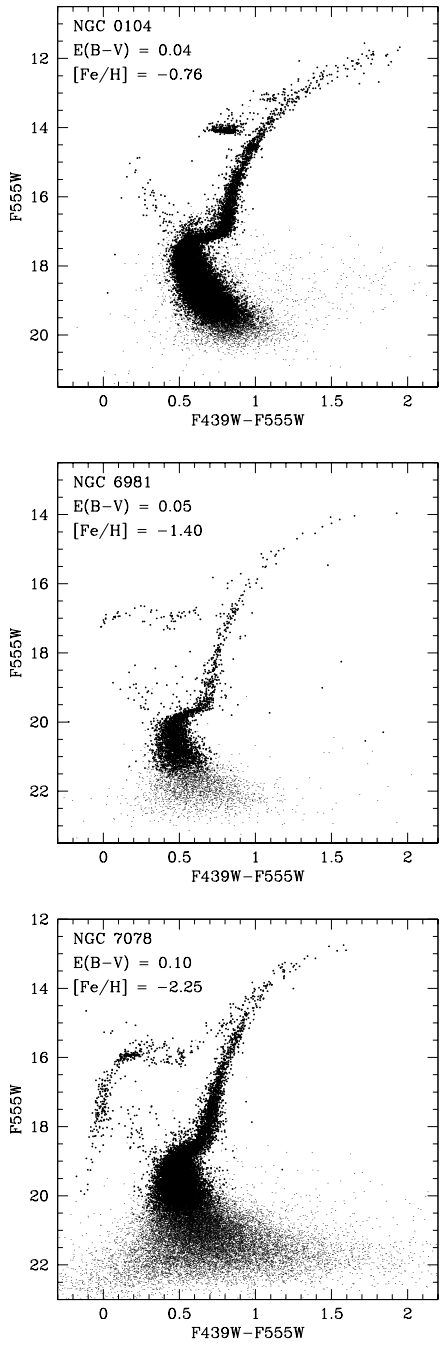


FIGURE 2.2— Colour-magnitude diagrams of three globular clusters: metal-rich NGC 104, intermediate-metallicity M72 (NGC 6981), and metal-poor M15 (NGC 7078). The bluewards extent of the HB increases as metallicity decreases, according to the first parameter effect (from Piotto et al. 2002).

accepting that there is also a spread in stellar mass along this branch, bluer stars being less massive (on the average) and less luminous than redder stars." Comparing HB models to observed globular cluster CMDs, Rood (1973) discovered that an HB which " *is made up of stars with the same core mass and slightly varying total mass, produces theoretical c-m diagrams very similar to those observed.A mass loss of perhaps 0.2 $M_{\odot}$ with a random dispersion of several hundredths of a solar mass is required somewhere along the giant branch.*" The need for very high helium abundances decreased with the assumption of mass lass on the red giant branch. Actually, with a more massive and thus physically larger envelope, the luminosity generated in the stellar interior is distributed over a large surface area, such a smaller photospheric effective temperature is required. In general, for any metallicity and for a fixed helium abundance and core mass, **ZAHB models are bluer with decreasing total mass.**

Caloi (1972) found that stars with very low envelope masses (0.02 $M_{\odot}$) lying along the extended or "extreme HB" (EHB) at high effective temperatures (>20,000 K), can be identified with the subdwarf B stars known in the field (Greenstein 1971). Sweigart, Mengel, & Demarque (1974) and Gingold (1976) investigated the post-HB evolution and noticed that, at variance with the more massive blue HB stars, EHB models do not ascend the second (asymptotic) giant branch (AGB), evolving directly to the white dwarf domain. Figure 2.3 shows the Sweigart, Mengel, & Demarque (1974) evolutionary tracks for the advanced evolution of three stars with composition (X,Z)=(0.732, 0.001), and with total masses of 0.453, 0.51 and 0.60 $M_{\odot}$. The star with $M_{\odot} = 0.51$, an EHB model, does not move back to the asymptotic branch after the formation of a helium-burning shell, but it proceeds blueward at a luminosity of about $\log L \simeq 2.2$.

Therefore, at present we know the horizontal branch hosts stars powered by a triple alpha helium burning core of about 0.5 $M_{\odot}$, and a hydrogen burning shell. The more massive the hydrogen envelope is, the cooler is the resulting star. The masses of the hydrogen envelopes vary from 0.02 $M_{\odot}$ to more than 0.2 $M_{\odot}$ for metal-poor hot HB stars. Hot HB stars eventually evolve up the AGB. The less massive envelopes of the even hotter EHB stars ($M_{env} \leq 0.02$ $M_{\odot}$, $T_{eff} \geq$ 20,000 K) do not support hydrogen shell burning. EHB stars do not climb the AGB but evolve directly to the white dwarf phase. For this reason, they are also called AGB manquè stars (Greggio & Renzini 1990). Hot HB stars populate the blue HB and the brighter part of the blue tail. The transition from hot to extreme HB stars occurs at the fainter part of the blue tail at $M_V \geq 3$ mag.

To a first approximation, the different location, extension, and morphology

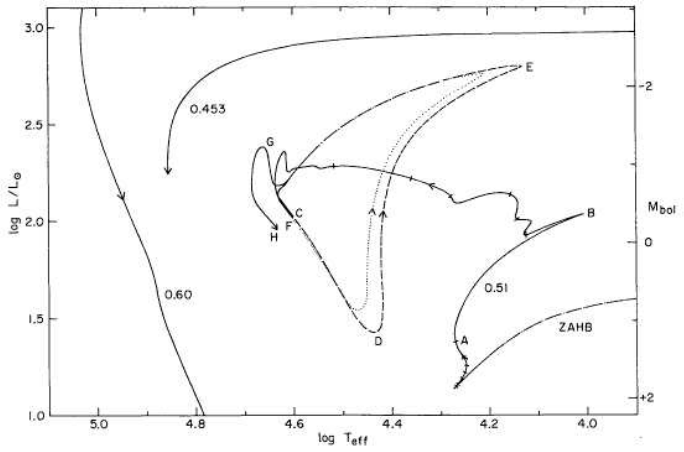


FIGURE 2.3— The Sweigart, Mengel, & Demarque (1974) evolutionary tracks for the advanced evolution of three stars with composition (X,Z)=(0.732, 0.001), and with total masses of 0.453, 0.51 and 0.60 $M_\odot$. The star with $M_\odot = 0.51$ is an EHB model.

of the observed HBs were described in terms of the variation of metal abundance, the *first parameter*: metal-rich clusters tend to have short red HBs, while metal-poor ones exhibit predominantly blue HBs. However, the previous approximation turned out to be too rough very soon. Some other parameter (or set of parameters) was evidently also at work, as clusters with nearly identical metallicities could show very different HB colour distributions (van den Berg 1967, and Sandage & Wildey 1967). This phenomenon is illustrated in figures 2.4 and 2.5, showing two groups of clusters. The first one is the pair formed by M3 and M13: they have [Fe/H]=-1.57 and [Fe/H]=-1.54 respectively, but they clearly show very different HB morphologies. The other group is formed by NGC 6341 (M92), NGC5466 and NGC7078 (M15) (with [Fe/H]= -2.29, -2.25 and -2.22 respectively). NGC 5466 has a blue HB populated up to $T_{eff} \simeq 10000$ K, M92 has a blue HB extended to $T_{eff} \simeq 12000$ K, and the HB of M15 extends up to $T_{eff} \simeq 40000$ K (cf. Buonanno et al. 1985 for a detailed discussion of the differences in HB morphologies of the three clusters).

Consequently, *HB morphology has to be ruled, apart from metallicity, by some other parameter or set of parameters.* Such mixed bag of HB anomalies is usually lumped under the term "second-parameter problem" (cf. Catelan et al. 1998):

On the other hand, blue tails and EHB stars still represent a puzzle in the stellar evolution theory. Furthermore, anomalous BTs can be found at any metallicity, even in metal-rich GCs like NGC 6388 ([Fe/H]=-0.6) and NGC 6441

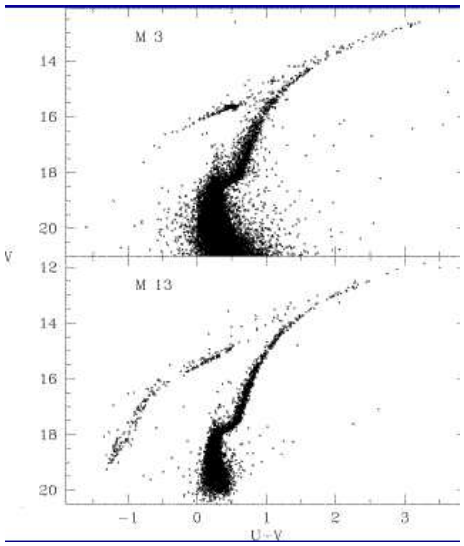


FIGURE 2.4— The CMDs of M3 and M13 (from Ferraro et al. 1997)

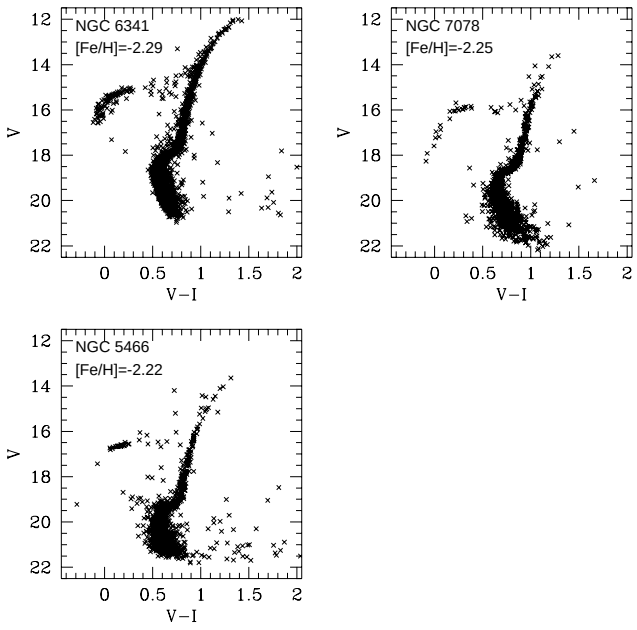


FIGURE 2.5— The CMDs of NGC5466, M92 and M15 from Rosenberg et al 2000. Note the rather different HBs, despite the very similar metal content.

(Rich et al. 1997). As explained above, we already know that blue tails host He-core H-shell burning stars which have lost up to a factor of two more mass, during the Red Giant Branch (RGB) ascent, than other HB stars in the same cluster (D'Cruz et al. 1996). However, *we still lack of an explanation for such a sizable mass loss.* In other words, we can say that blue tails are the most extreme expression of the second parameter problem.

Second parameter candidates.

The following paragraphs describe the many non-canonical scenarios proposed to explain the second parameter phenomenon. Most of these mechanisms influence the HB morphology by regulating either the core mass or the amount of mass loss that a star experiences on the upper red giant branch.

- **Cluster Age**.- It was initially suggested to justify the HB morphological differences between clusters with almost identical metallicity (Searle 1978; Lee et al. 1994; Stetson et al. 1995). Actually, for a fixed chemical composition and assuming identical mass-loss, that may be zero, during the RGB phase, the stars evolving from the RGB toward the ZAHB have smaller initial masses with increasing cluster age (although the He core, at the He flash is nearly constant). Consequently, ZAHB models are expected to be bluer with increasing age. However, this explanation is still controversial. Rosenberg et al. (2000) conclude that the GC formation process started at the same time throughout the halo, at least out to ~20 kpc from the Galactic center (Rosenberg et al. 2000). Their conclusions are based in measurements of the relative ages of 34 GGCs. Age differences are not enough to justify the colour spread among the observed HBs.

- **Helium Mixing**.- Helium mixing in red giants enriches the red giant's envelope with helium freshly produced in the hydrogen-burning shell. A red giant undergoing helium mixing will evolve to higher luminosities, and thus loosing more mass than canonically expected, producing a hotter HB star (see Sweigart 1997a, 1997b, for more details). Only part of the helium produced in the hydrogen shell of the helium-mixed models is added to the core. As a result, the core grows and heats up more slowly, delaying the helium flash. Therefore, different amounts of mixing in the red giant precursors could lead to HB stars with different temperatures. At the same time, this would explain some of the anomalous abundance distributions observed in globular cluster red giants (see Kraft 1994; Kraft et al. 1997 for reviews, and Gratton et al. 2001 for most recent evidence of primordial abundance variations). Charbonnel, Denissenkov, & Weiss

(2000) and Caloi (2001), however, argue that current observational results for both HB stars and red giants do not support the idea of helium mixing being active in globular cluster red giants.

- **[CNO/Fe] abundance**.- For hot HB stars, a decrease in CNO abundances results in bluer colours at a given envelope mass. This is a similar effect to that seen for a decrease in overall metallicity (Rood & Seitzer 1981), as CNO abundance controls opacity and energy generation within horizontal branch stars. Nevertheless, Suntzeff (1981) measured carbon and nitrogen abundances in about 30 red giants in each of the two clusters M3 and M13. The combination of their C and N abundances with published O measurements showed that the difference in Z(CNO) between the two clusters is too small to account for the difference in horizontal branch morphologies.

- **Cluster concentration**.- There are evidences that cluster density can be related to BTs extension (Fusi Pecci et al. 1993). Close encounters in the high density environments of GCs could increase mass loss by tidal stripping during the RGB phase, thus generating bluer HB stars. However, the results of Bedin et al. (2000) on NGC 2808, which shows BT stars even in the outer envelope, seem to question the influence of stellar density on the formation of hot HB stars.

- **Rotation**.- Rotation would delay the helium core flash in a red giant, increasing the helium core mass and the mass loss rate. This would result in bluer and brighter HB stars (see also Buonanno, Corsi, & Fusi Pecci 1985; Peterson, Rood, & Crocker 1995; Sills & Pinsonneault 2000). Nonetheless, this scenario predicts that higher rotation rates in hotter HB stars should be observed, which is not confirmed by observations (Behr el al. 2000 and the present thesis).

- **Planets**.- Soker (1998) proposed that fast HB rotators could have spun up by swallowing close planetary companions during the RGB phase, thereby increasing mass loss and the temperature of the resulting HB star. However, no planetary companions have been found in a very intense search for them in the GC 47 Tuc (Gilliland et al. 2000), which on the other hand, does not have a blue tail (see also Soker & Hadar, 2001).

- **Cluster self-enrichment**.- Recently, D'antona et al. 2002 proposed a scenario that connects the O-Na anticorrelation detected among non evolved stars in GCs (see Gratton et al. 2001, Thévenin et al2001) and blue tails. If a second generation of stars formed within GCs from kinematically cool

ejecta of massive asymptotic giant branch stars (Cottrell & Da Costa 1981), the age difference between the original and the second population (a few 10^8 yr) is too small to be directly detectable as different turn-offs. However, this second generation of O-poor, Na-rich stars should also be enriched in He. He-rich stars evolve faster on the Main Sequence, so that stars currently at the turn-off should also be less massive (by about 0.05 $M_\odot$) than "normal" He-poor stars. If these stars loose mass at the same rate as normal stars on the RGB, their descendants should start their HB evolution with a considerable smaller mass, and hence should be much hotter.

2.2 The recent observational framework

2.2.1 Stellar distributions along HB Blue Tails

Blue tails often display gaps, i.e. regions underpopulated in stars, at varying brightness. Such gaps, also detected for field HB stars (Newell 1973; Heber et al. 1984), were already noticed in some of the clusters observed by Arp in 1955. Ferraro et al. (1998) argue that all intermediate-metallicity globular clusters ([Fe/H] -1.5) with a very long blue tail show a gap at about 18,000 K. Piotto et al. (1999b) extend the discussion to include metal-rich globular clusters, suggesting a gap *at constant mass*, which will result in gaps at different temperatures, for differing metallicities (see Figure 2.6).

As the gaps are not expected from canonical evolutionary scenarios, various non-canonical explanations have been suggested during the past 25 years (see again S. Moehler, 2001 review):

Diverging evolutionary paths.- Newell (1973) suggested the evolution away from the ZAHB as an explanation for the gap seen in UBV photometry of field HB stars at temperatures corresponding to $\simeq$ 12,900 K. In addition, Heber et al. (1984) argued that the small gap at 20,000 K between field horizontal branch B (HBB) type and sdB stars could be interpreted by diverging evolution (see also Lee, Demarque, & Zinn, 1994). Other calculations show, however, that the effect is not large enough to account for the gaps along the HBs (see, e.g., Dorman, Lee, & VandenBerg 1991; Catelan et al. 1998).

Variations in mass loss.- D'Cruz et al. (1996) argue that bimodal HBs become more probable for increasing metallicity as the range in mass-loss efficiency necessary to produce an EHB star stays constant (i.e., independent of metallicity), while only a very narrow range of mass-loss efficiency can produce mid-HB stars at high metallicities. Therefore, the number of mid-HB stars is expected to decrease with increasing metallicity, opening a wide gap between cool HB stars and EHB stars at high metallicity. On the other hand, Yong,

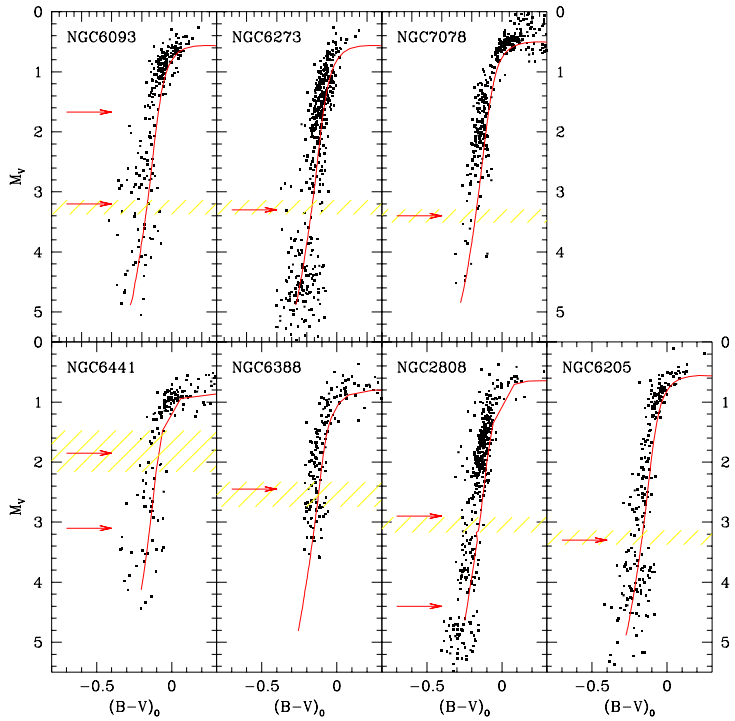


FIGURE 2.6— The BTs of the clusters studied in Piotto et al. (1999b) are matched with the models by Bono et al. (1999). Metallicity increases from the lower-left box to the upper-right. Note that the distribution of the gaps is not uniform, the visible gaps are marked with arrows. The shaded regions identify the magnitude intervals that, according to the models, correspond to $0.53 < M/M_{\odot} < 0.54$.

Demarque, & Yi (2000) suggest that mass loss on the HB could lead to EHB stars in very metal-rich environments, as for the open cluster NGC 6791 ([Fe/H] = +0.5). These scenarios offer good interpretations for the sdB stars and the large gap discovered in the metal-rich open cluster NGC 6791 (Kaluzny & Udalski 1992; Liebert, Saffer, & Green 1994), but they cannot explain the smaller gaps seen in the mostly rather metal-poor globular clusters. Rood, Whitney, & D'Cruz (1997) and Ferraro et al. (1998) also propose variations in mass loss on the red giant branch as possible causes for gaps along the HB. Caloi (1999), however, finds that HB evolution would tend to fill in gaps in the initial ZAHB distribution.

Differences in [CNO/Fe], He mixing or rotation.- Bimodal distributions in any of these previously mentioned second parameter candidates may create gaps along the HB.

Dynamical interactions.- A gap could be interpreted as a separation beween stars generated by different mechanisms. This would be the case if the stars below the gaps do not descend from red giants. The better candidates for such different formation mechanisms are binary interactions such as common-envelope evolution, merging of stars, etc. (see Bailyn et al. 1992; Bailyn 1995; Moehler, Heber, & Rupprecht 1997b). Binary scenarios create stars similar to the sdB, sdOB, and sdO stars, known from the field of the Milky Way, but no hot mid-HB stars woulf be generated. The main objection to the dynamical scenarios is that the numbers of red giant (RGB/AGB) stars relative to those of "true" HB stars, which give an estimate of the cluster's original helium abundance, would vary from cluster to cluster, pretending different primordial helium abundances (see Buonanno et al. 1985; Fusi Pecci et al. 1993). Observations show, however, that only including all the HB stars we can obtain normal helium contents (Zoccali et al. 1999). Another objection is the tight sequence in temperature and surface gravity reported by Heber et al. (1986) and Moehler et al. (1997b) for stars below the faint gap in NGC 6752. In addition, dynamically very different clusters, as M15 and NGC 288, can show very similar blue tails, suggesting to rule out production of BT stars by dynamical interactions like merging (Crocker et al., 1988). This is also the case of M13 and M3, which are dynamically very similar but have very different HB morphologies (Ferraro et al., 1997). Bedin et al. (2000; NGC 2808) and D'Cruz et al. (2000; ΩCen) find no radial gradient in the ratio of very faint blue stars to blue HB stars, arguing against dynamical interactions as the cause for the extremely faint blue stars. Chapter 6 in the present thesis also investigates HB morphology dependence on cluster density.

Atmospheric processes.- Caloi (1999) suggested the onset of diffusion in the stellar atmospheres as an explanation for the gaps around $(B\text{-}V)_0 = 0$.

This scenario would predict chemical peculiarities in bluer stars. Nevertheless, Grundahl et al. (1999) propose radiative levitation of heavy elements in the atmosphere as the cause for the u-jump observed in many globular clusters (see section 2.5 in this thesis) at $T_{eff} \simeq 11{,}500$ K, which does not always coincides with a stellar distribution gap along the BT (see for example the Bedin et al. 2000 CMDs of NGC 2808).

Statistical fluctuations.- Catelan et al. (1998), via synthetic HB simulations, show that at least some of the gaps may be caused by statistical fluctuations. Ferraro et al. (1998) and Piotto et al. (1999), however, report gaps at physically similar positions (i.e., temperature or mass) in several globular clusters.

Helium variations due to self-pollution.- In the D'Antona et al. (2002) scenario described in section 2.1.2, gaps in the HB stellar distribution could reflect content of the constituent matter, due to the difference in the helium abundance in the ejecta of AGBs of different mass (Ventura et al. 2002) and to some peculiar modalities of star formation from these ejecta.

2.2.2 Atmospheric Parameters: effective temperature and gravities.

Already in 1966, Graham & Doremus reported that the comparison of the Strömgren parameter $(c1)_0$ versus $(b\text{-}y)_0$ for 50 BHB stars in NGC 6397 with models by Mihalas (1966) indicated low surface gravities, compared to theoretical expectations: "*It is clear that the accurate fixing of this parameter [log g] is of the greatest importance for fixing limits to the masses of the horizontal branch stars since there seems no other way, at present, of determining them more directly.*"

Later spectroscopic analyses of HB stars in GCs with and without gaps along their HBs and/or BTs reproduced this effect. Figure 2.7 shows the surface gravities (log g) plotted against the temperature (log Teff) for 6 globular cluster horizontal branches: M5, M92, NGC288 (Crocker et al. 1998), NGC 6397 (de Boer et al. 1995), M15 (Moehler et al. 1995 and 1997a) and NGC 6752 (Moehler et al. 1997b). They are compared to evolutionary tracks from Dorman et al. (1993). The ZAHB, the Terminal-Age Horizontal Branch (TAHB) (defined by the core helium exhaustion) and the helium main sequence are indicated.

For temperatures between 11,500 and 20,500 K, the observed positions in the (log g, Teff) diagram fall mostly above the ZAHB. Similary, field HBB stars show a larger scatter away from the ZAHB in Teff, log g than sdB stars (Saffer et al., 1997).

In addition, masses for the stars can be inferred via their atmospheric parameters and the distances to the globular clusters (cf. Moehler, Heber, & de

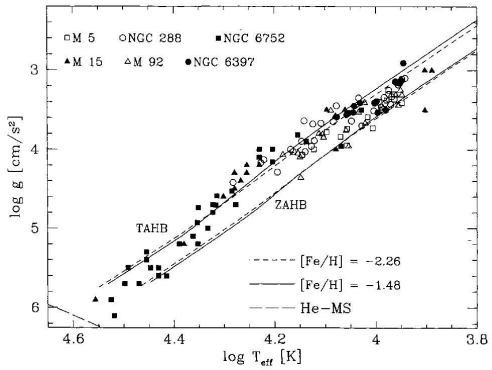


FIGURE 2.7— Results of Crocker et al. (1988; M3, M5, M92, NGC 288), de Boer et al. (1995; NGC 6397), and Moehler et al. (1995, 1997a; M15; 1997b; NGC 6752) compared to evolutionary tracks from Dorman, Rood, & O'Connell (1993). The ZAHB, the TAHB and the helium main sequence are indicated.

Boer 1994, 1995; Moehler et al. 1997b; de Boer et al. 1995). With the exception of M3, M5, and NGC 6752, which have mean stellar masses consistent with the canonical values, the hot HB stars in all the other clusters show masses that are significantly lower than predicted by canonical HB evolution, even for temperatures cooler than 11,500 K where the stars do not deviate from the canonical tracks in surface gravity.

2.2.3 The luminosity jump in blue bands.

A "jump" in the blue horizontal-branch distribution in the $(V, u-y)$ colour-magnitude diagram was first detected in the globular cluster M13 (NGC 6205) by Grundahl et al. (1998). Such an effect is morphologically best characterized as a discontinuity in the $(u, u-y)$ locus, with stars in the range 11,500 K $\leq T_{eff} \leq$ 20,000 K deviating systematically from (in the sense of appearing brighter and/or hotter than) canonical zero-age HB models. Grundahl et al. (1999) presented Strömgren u, y photometry of 14 GCs and demonstrated that the jump in Strömgren u is present in every GC whose HB extends beyond $T_{eff} \simeq$ 11,500 K, irrespective of metallicity, mixing history on RGB, or any other parameter. They thus suggested that the u jump is an ubiquitous feature, intrinsic to all HB stars hotter than $T_{eff} \simeq$ 11,500 K. Figure 2.8 shows the Grundahl et al. photometry for the BT cluster M13.

Furthermore, they inferred a parallel between the ubiquitous nature of the u jump and the previously described problem of low measured gravities among blue HB stars in GCs and in the field. The "gravity jump" occurs over the same

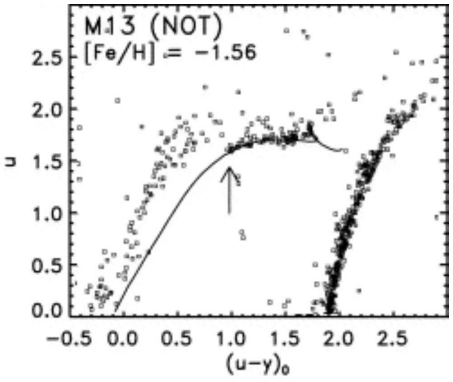


FIGURE 2.8— The $(u, u-y)$ CMD of M13 by Grundahl at al. (1999), around the HB region. The canonical ZAHB model is from VandenBerg et al. (1999) The onset of the jump is indicated by a vertical arrow.

temperature range as the u jump, and, in addition, it appears in every metal-poor cluster for which gravities have been determined, again irrespective of metallicity, mixing history on the RGB, or any known parameter characterizing the surveyed GCs. The u jump and the gravity jump are connected on a star-by-star basis, suggesting that most likely the two are different manifestations of the same physical phenomenon. For that reason, Grundahl et al. (1999) proposed radiative levitation of heavy elements to suprasolar abundances as the cause for the u-jump. They argued that "*the Strömgren u bandpass is located just shortward of the Balmer jump, and thus the emergent flux is dominated by the hydrogen opacity. Atmospheric effects (related, e.g., to an increase in the metal opacity) that decrease the relative importance of the hydrogen opacity should result in a brighter Strömgren u flux.*" This luminosity jump is also visible in the Johnson U band (Bedin et al. 2000, Momany et al. 2002).

The effective temperature of the jump coincides with the region where surface convection zones due to hydrogen and He I ionization disappear in HB stars. Figure 2.9, taken from Sweigart (2001) shows the variation of the envelope convection with T_{eff} along the canonical ZAHB for [Fe/H] = -1.6. Shaded areas are convective. The ordinate gives the depth in radius r into the models.

Later on, Moehler et al. (2000) derived atmospheric parameters (T_{eff}, log g), masses and helium abundances for 42 hot horizontal branch stars in the globular cluster NGC 6752. Taking into account the enrichment of heavy elements resulting from their spectroscopic analyses, they found that high iron abundances could explain part, but not all, of the problem of anomalously low gravities along the blue HB. The blue HB stars cooler than about 15,100 K

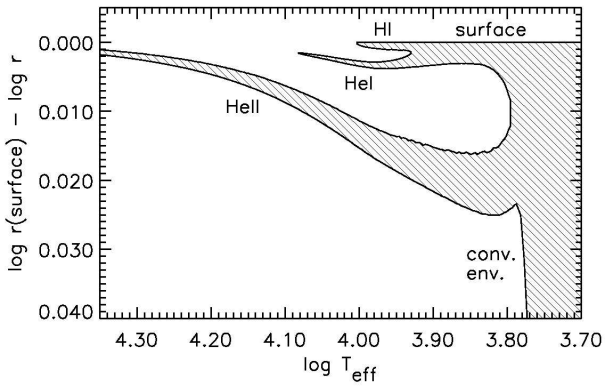


FIGURE 2.9— Sweigart (2001) graph of the variation of the envelope convection with T_{eff} along the canonical ZAHB for [Fe/H] = -1.6.

and the sdB stars (T_{eff} > 20,000 K) agree well with canonical theory when analyzed with metal-rich ([M/H] = +0.5) model atmospheres, but the stars in between these two groups remain offset toward lower gravities and masses. He mixing combined with radiative levitation may also be necessary. Vink and Cassisi (2002), on the other hand, argue that mass loss in HB may - together with the enhancement of heavy element abundances due to radiative levitation - provide an explanation for the so-called "low gravity" problem.

An attempt to reproduce gaps and overluminosities has already been done by Hui Bon Hoa et al. (2000), adding diffusion + stratification to their model atmospheres.

2.2.4 Abundance variations along the HB.

Thanks to observations of NGC 6397, M13, M15 and M92, Searle & Rodgers (1966) and Sargent (1967), had already found that blue HB and BT stars show weaker helium lines than field main-sequence B stars of similar temperatures. Greenstein, Truran, & Cameron (1967) suggested diffusion to explain this He deficiency.

Michaud, Vauclair, & Vauclair (1983) presented the first theoretical analysis of diffusion effects in hot and extreme HB stars. Using the evolutionary tracks of Sweigart & Gross (1976), they found for the metal-poor models that "in most of the envelope, the radiative acceleration on all elements [i.e., C, N, O, Ca, Fe] is much larger than gravity which is not the case in main-sequence stars." The elements are thus pushed toward the surface of the star. Turbulence affects the different elements to a varying extent but generally reduces the overabundances.

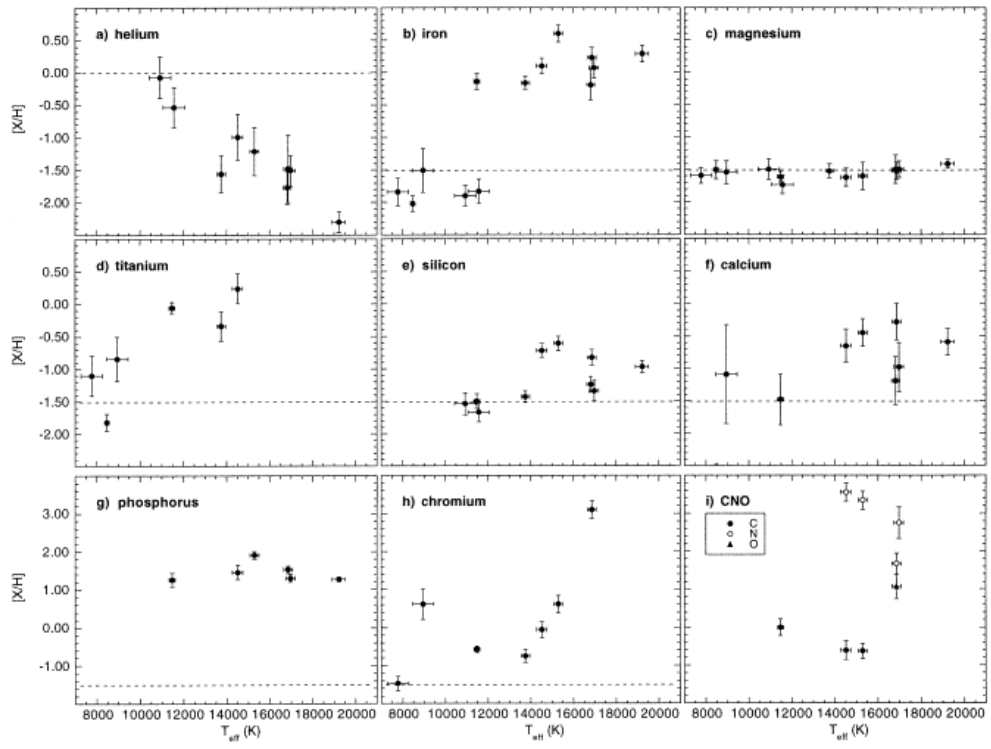


FIGURE 2.10— Behr et al. (1999) abundance measurements of blue HB stars in M13. The dotted line represents the expected value of [X/H] for stars in M13 (ignoring dredge-up of fusion-processed or -enhanced material): -1.51 dex from solar for the metals and the solar ratio for helium.

Models without turbulence and/or mass loss (which may reduce the effects of diffusion) predict stronger He depletions than were observed, but a weak stellar wind could explain this discrepancy (Heber 1986; Michaud et al. 1989; Fontaine & Chayer 1997; Unglaub & Bues, 1998).

The predicted abundance variations changes with effective temperature, rangin from none, in HB stars cooler than about 5800 ± 500 K (due to the very long diffusion timescales), to 2-4 dex in the hotter stars (the hottest model has Teff = 20,700 K). This also depends on the considered element. The over-abundances in the two hottest models (12,500 and 20,700 K) are limited to 3 dex for relatively abundant elements by the saturation of lines. Less abundant elements such as P, Eu, Ga could show much larger overabundances before their lines saturate (up to 5 dex for original values of [M/H] = -2).

Observations of BHB and BT stars in globular clusters confirm the onset of

diffusion being active above a certain temperature. Detailed abundance analysis of blue HB (BHB) stars in globular clusters was first attempted by Glaspey et al. (1986, 1989) in NGC 6397 and NGC 6752. They found evidence of helium depletion and metal enhancement in one blue tail star, while stars populating the cool part of the BHB presented abundances fully in agreement with canonical cluster metallicities. Later on, the analysis by Lambert, McWilliam, & Smith (1992) in M4 and NGC 6397, Peterson et al. (1995) in NGC 288 and M13, Cohen & McCarthy (1997) in M92, Behr et al. (1999) in M13, Behr et al. 2000a in M15 and Peterson et al. (2000) and Moehler et al. (2000c) in NGC 6752 showed that *BHB stars cooler than 11,000-12,000 K in general show no deviations from the globular cluster abundances derived from red giants. Nevertheless, stars hotter than 11,000-12,000 K, show remarkable over-abundances of heavy elements (Fe, Ti, N, P, etc.) and a strong helium depletion.* Figure 2.10 presents the Behr et al. (1999) results for M13, where metal enhancements and helium depletion are very clearly detected.

All these observational evidences support the Grundahl et al. (1999) suggestion, previously mentioned, that the onset of diffusion in stellar atmospheres may play a role in explaining the jump along the HB, toward brighter u-magnitudes, at effective temperatures of about 11,500 K.

2.2.5 Rotational velocity distribution of HB stars.

High-resolution spectroscopic studies of BHB stars in M3, M4, M5, M13, and NGC 288 by R. Peterson et al(1983, 1985a, 1985b) seemed to suggest that clusters with bluer HB morphologies show higher HB rotational velocities. Their observations were limited to the cool side of the blue HB, that is, to stars with $8.000 < T_{eff} < 11.000$ K, but they contributed to the idea that rotation affects the distribution of stars along the HB. In M13, which has a long blue tail, some of the stars were presented $v\sin i$ values (the projected rotational velocity) as high as 40 km/s. The peaks of rotation in other clusters were smaller, 20 km/s, but still unexpectedly high. The progenitors of these low mass blue HB stars are expected to have lost most of their angular momentum via magnetically-coupled winds during their main sequence lifetime. Therefore, they should present modest rotation rates, of the order of 2 km/s, like the Sun. Moreover, we would expect a further slowing down of those stars, as they loose mass in the red giant branch (RGB) ascent. Even taking into account the increase in radius and the redistribution of moment of inertia, as a star evolves from the main sequence to the HB, it is difficult to increase the surface velocity beyond 10 or 12 km/s, in order to explain the observed rotations.A rapidly rotating core in the main-sequence stars (which would in any

case violate the helioseismological results for the Sun), or an additional source of angular momentum on the RGB (e.g., mass transfer in close binaries, or due to planets as described by Soker & Harpaz 2000) is required to explain the rotation of BHB stars.

Behr et al. (2000b) confirmed these results for BHB and BT stars in M13, where they measured rotational velocities for stars as hot as 15,000 K (Behr, 2002). In addition, their observations revealed that stars hotter than about 11,000 K have significantly lower rotational velocities than cooler stars. This abrupt change in mean rotational velocity seemed to coincide with the gap seen along the BHB of M13. Support to this result came from the results of Cohen & McCarthy (1997) for M92 and Behr, Cohen, & McCarthy (2000a) for M15, which show that HB stars cooler than 11,000-12,000 K in general rotate faster than hotter stars. The results by Behr et al. (2000b) for M13 are presented in figure 2.11.

Theoretical models by Sills & Pinsonneault (2000) for the rotation of HB stars suggest that the observed rotation of cool BHB stars in M13 can be explained assuming that RGB stars have rapidly rotating cores and differential rotation in their convective envelopes, if the angular momentum is redistributed from the rapidly rotating core to the envelope, probably already on the HB. The change in rotation rates toward higher temperatures is not predicted by the models but could be understood as a result of gravitational settling, which creates a mean molecular weight gradient that then inhibits angular momentum transport in the star. Moreover, Sweigart (2001) argues that the drop in rotational velocity for temperatures hotter than $\sim$ 11500 could also be explained by the weak stellar wind invoked to reconcile the observed abundances in hot and extreme HB stars with diffusion calculations, as it could also carry away angular momentum from the surface layers.

Other possible interpretations call for the role of low-mass companions, mainly gas giant planets, brown dwarfs or even low-mass main-sequence stars, in post-RGB stellar evolution. Soker & Harpaz (2000) suggest that the distribution of rotational velocities along the HB can be explained by spin-up of the progenitors due to interaction with a low-mass companion. In their scenario, the slower rotation of the hotter stars is explained by mass loss on the HB, which is accompanied by efficient angular momentum loss.

2.2.6 Binary frequency in the blue HB.

A number of investigations have shown that a large fraction of field sdB stars are binary systems. Maxted et al. (2001) estimated that $(69 \pm 9)\%$ sdBs are short period ($0.03 \leq P \leq 10$ days) binaries. Very similar conclusions are

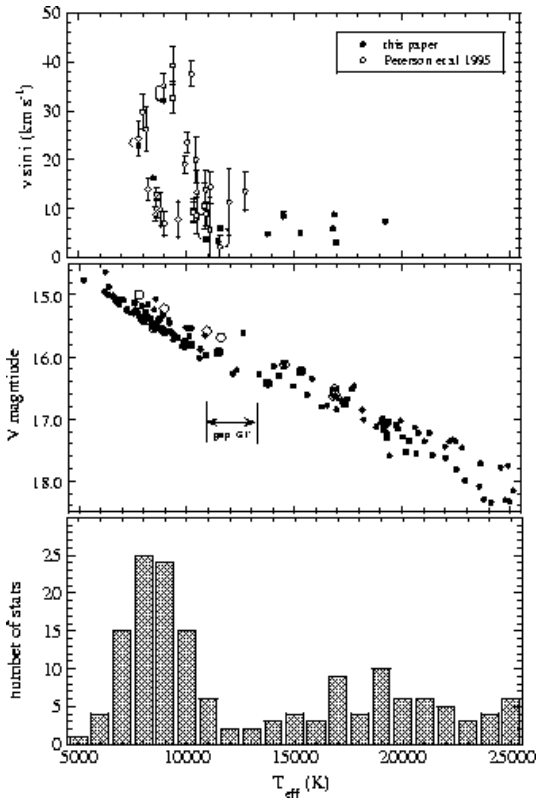


FIGURE 2.11— Projected rotational velocities and temperature distribution of stars along the HB of M13. In the top panel, the $v\sin i$ for the 13 stars observed by Behr et al. (1999a, *solid symbols*) and the 29 stars from P95 (*open symbols*) is plotted. In the middle panel there is the V - T_{eff} colour-magnitude diagram showing the gap at $T_{eff} \sim 12000$. The open symbols in this panel identify the stars observed by Behr et al. In the bottom panel there is a histogram of star counts. Note the abrupt change in rotational velocity in correspondence to the gap.

reached by Saffer et al. (2001). The orbital separation of the stars in these binaries is much less than the size of the red giants from which the EHB star has formed (Maxted et al. 2001). These results are strong evidence that binary star evolution is fundamental to the formation of the majority of sdB stars in the field.

An argument against binary evolution of EHB stars comes from the lack of clear evidence, in globular clusters, of radial gradients in their distribution. Nevertheless, incompleteness in cluster centers and the rarity of EHB stars may have masked such gradients. Indeed, radial-velocity variations have been directly observed among EHB stars in the globular cluster NGC 6752. Peterson et al. (2001) measured velocities at 1 Å resolution in 49 blue tail stars in NGC 6752, taking spectra over a 6hr period during each of two consecutive nights. Of the 25 EHB stars with $16.4 < V < 18.0$ and $B - V \leq -0.10$, eleven show a radial-velocity variation greater than three times the joint standard deviation between spectra taken three hours apart, and a twelfth shows a similar variation from one night to the next. Among the remaining 24 cooler blue tail stars, only one shows a similar variation. As in the field, then, the EHB stars in this globular cluster are largely short-period binaries.

2.2.7 Tilted HBs in metal-rich clusters.

Recent Hubble Space Telescope observations (Piotto et al. 1997; Rich et al. 1997) have found that the horizontal branches in the metal-rich globular clusters NGC 6388 and NGC 6441 slope upward with decreasing B-V. Canonical models account for a tilt of the order of $\Delta V \simeq 0.1$ mag, due to the behaviour of the bolometric correction (Brocato et al. 1999): thus, of the same order of magnitude as the tilted HB already observed in NGC 1851 (Walker 1998), possibly in NGC 6229 (Borissova et al. 1999), and in NGC 6712 (Ortolani et al. 2000). Much larger tilts ($\Delta V \simeq 0.5$ mag) as those observed in NGC 6388 and NGC 6441, could not in principle be explained by canonical scenarios. On the other hand, such a slope cannot be produced by either a greater cluster age or enhanced mass loss along the red giant branch.

In both NGC 6441 and NGC 6388, the evidence for the tilt is accompanied by the parallel and unexpected occurrence of an extended, extremely blue HB, against the general red morphology of metal-rich HBs (see Figure 2.12). Thus, one is tempted to speculate whether the tilt and the "blue tail" both originate from a common mechanism. As a matter of fact, Sweigart & Catelan (1998) already suggested three noncanonical scenarios accounting for these features, as given by (1) abnormally high original Y abundances, (2) a spread in He cores due to stellar rotation, and (3) differential deep mixing along the RGB.

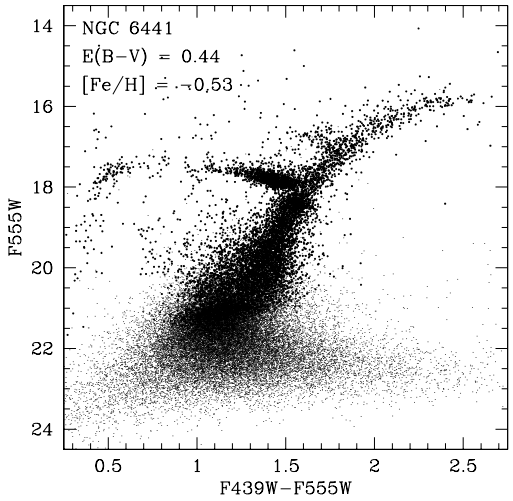


FIGURE 2.12— The metal-rich cluster NGC 6441 from Piotto et al. (2002).

However, the occurrence of an extremely high original Y in this cluster has been already discarded by Layden et al. (1999) on the basis of the R method, whereas Moehler, Sweigart, & Catelan (1999) found that spectroscopic results for blue HB stars in these clusters are inconsistent with all three of these noncanonical scenarios.

In the recent literature, it has been repeatedly suggested that the peculiar HB in the two clusters could be connected with a spread in the metallicity of cluster stars (Piotto et al. 1997; Sweigart 2002; Pritzl et al. 2001). The role of differential reddening in NGC 6441 has already been suggested by Piotto et al. (1997) and Layden et al. (1999). However, Raimondo et al. (2002) argue against both possibilities analyzing the HST snapshot photometry of NGC 6441 from Piotto et al. (2002). In addition, the evidence for a sloping red HB in clusters such as NGC 6356 or NGC 6624 (Piotto et al. 2002), with a rather well-defined red giant sequence, suggests that the sloping red HB is a real feature of metal-rich clusters.

2.2.8 Hot HB stars and the *UV* excess in elliptical galaxies.

Bertola et al. (1980) showed that the visual and UV energy distribution of the nucleus of M87 reveals an essentially continuous curve from 1300 to 10,500 A, and a turnup in flux below 2200 $\mathring{A}$.This intriguing phenomenon, called the UV upturn in elliptical galaxies (see also Code and Welch, 1979) is plausibly

connected with GC EHB stars.

Elliptical galaxies, which, as the strength of the Mg_2 indicates, are in general even more metal-rich than metal-rich globular clusters. UV observations showed that such old, metal-rich systems contain hot stars (Burstein et al. 1988). Stellar evolution models performed by Greggio & Renzini (1990, 1999) yield the maximum lifetime UV output for EHB stars with envelope masses $M_{env} \leq 0.02\ M_{\odot}$, while post-AGB stars do not live long enough at high temperatures to play a significant role for the UV flux. Brown et al. (1997) presented further observational support of hot subdwarfs as the cause for the UV excess in elliptical galaxies Their analysis of HUT spectra of six elliptical and S0 galaxies shows that models with supersolar metal and helium abundances provide the best fit to the flux distribution of the observed spectra. In addition, EHB stars are required in all fits. Most absorption line features (of C, N, Si, i.e., light elements), however, are consistent with [M/H] = -1, in contrast to the energy distribution. This may be due to selective diffusion in the atmospheres of the EHB stars.

A detailed discussion of the observational evidence for UV excess in elliptical galaxies is presented by Dorman et al. (1995). Comparing the UV-visual colour $(15\text{-}V)_0$ for galaxies and globular clusters to the Mg_2 metallicity index (see Fig. 2.13, 15 being the observed brightness at 1500), they find that, while the globular clusters and the galaxies have different ranges in Mg_2, they overlap in $(15\text{-}V)_0$, with the globular clusters being bluer on average. Metal-rich globular clusters as 47 Tuc, NGC 6388, and NGC 6441 and the small elliptical galaxy M32 are placed in a region between globular clusters and galaxies in Mg_2. Therfore, the analysis of hot HB stars can provide additional information on the nature of the UV excess in elliptical galaxies, as suggested by their finding in the metal-rich "transition" globular clusters.

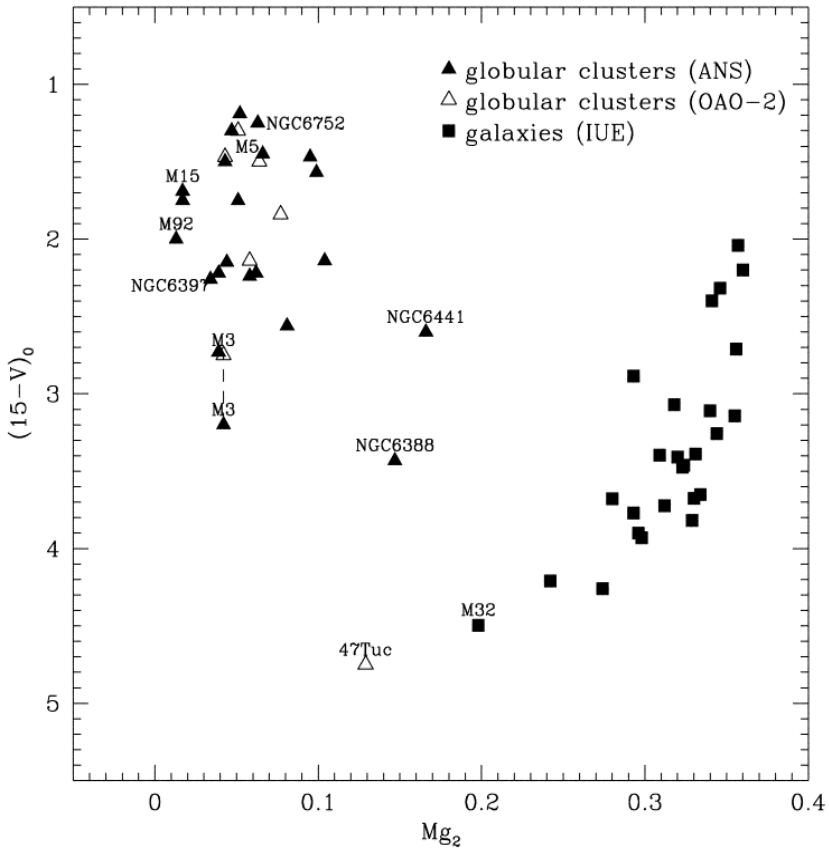


FIGURE 2.13— UV-visual colour (15-V)$_0$ vs. metallicity index Mg2 for globular clusters and elliptical galaxies (adapted by Moehler (2001) from Dorman et al. 1995. 15 is the brightness at 1500 .

Part II

Spectroscopy: Rotation and abundances of Hot Horizontal Branch Stars

3

Target selection: observations and data reduction.

In the following sections, the dataset, collected for the spectroscopic analysis of BT stars, is presented. To this purpose, we review the target selection, the observations and the data reduction.

3.1 Target selection

In this part of our investigation, we were interested to investigate all the possible connections between the HB morphology and the rotation rate and atmospheric abundances of HB stars. Therefore, we selected clusters with different blue tail extensions.

Our targets, NGC 1904 (M79), NGC 2808, NGC 6093 (M80) and NGC 7078 (M15), can be considered to be representative of blue tail clusters, as their horizontal branches have different extensions: the HB of M79 reaches $T_{eff} \sim$ 23,000 K, while the HB in NGC 2808 goes up to $T_{eff} \sim$ 37,000 K. The target clusters have different metallicities. They are all high concentrated clusters, though only one of our targets, M15, is core collapsed. Their main parameters are summarized in Table 3.1. The total number of target stars for each cluster and magnitude interval along the HB is also presented. Note that, as the measurement of the projected rotational velocity ($v \sin i$) is inherently statistical, we have observed at least 14-15 stars per cluster.

The properties of the specific clusters are outlined in the following paragraphs:

- **NGC 1904 (M79)**.- It is an intermediate metallicity cluster with a blue

Cluster	**[Fe/H]**	**E(B-V)**	**(m-M)$_V$**	**log(r_t/r_c)**	**R_{GC} (Kpc)**	ΔV	**Stars**
NGC 1904	−1.37	0.01	15.59	1.72	18.8	16.2 - 16.5 16.5 - 17.0 17.0 - 17.5 17.5 - 18.0	8 6 4 2
NGC 2808	−1.21	0.23	15.56	1.77	11.0	16.3 - 18.0 18.7 - 19.0	13 7
NGC 6093	−1.43	0.18	15.56	1.95	3.8	16.5 - 17.0 17.0 - 17.5 17.5 - 18.0 18.0 - 18.5	5 3 2 4
NGC 7078	−2.12	0.10	15.37	2.50*c*	3.9	16.0 - 16.5 17.0 - 17.5	9 7

TABLE 3.1— The target clusters and stars. [Fe/H] is from Carretta et al. (2001). The reddening, distance modulus, central concentration and Galactocentric distance are taken from Harris (1999).

tail reaching $T_{eff} \sim 23{,}000$ K, the stubbiest HB of our sample. Situated at 18.8 Kpc of the Galactic center, it is the most external cluster among the targets, and the less concentrated one. Hill et al. (1996) give a $T_{\rm eff} = 9{,}900$ K for a possible gap along the M79 BT. Grundahl et al. (1999) measured a u jump of 0.71 ± 0.04 magnitudes at $(u-y)$=0.99 ± 0.05, corresponding to $T_{\rm eff} = 11{,}500$ K. Moreover, the analysis of radiative levitation effects on the HB of this cluster can be directly compared with the Behr et al. (1999) results in M13, as these clusters have very similar metallicity ($[{\rm Fe/H}]_{M13}$= -1.39). Thirteen stars cooler and seven hotter than the jump are included in our program. Eleven of them are taken from Stetson & Harris (1977), and they are located in the external regions of the cluster. The other nine were selected from the HST-WFPC2 F439W and F555W photometry by Piotto et al. (2002, cf. http://menhir.pd.astro.it) in a more central region. In addition, we have also identified our target stars in the Strömgren u, y photometry by Grundahl et al. (1999) (kindly provided by F. Grundahl), for a better determination of their effective temperatures.

- **NGC 2808** .- Its bimodal HB ends in a BT extending at least to V = 21.1 ($T_{\rm eff}$ = 37,000 K) (Sosin et al. 1997). This BT is present even beyond 400 arcsec from the cluster center, corresponding to more than nine times the half mass radius (Bedin et al., 2000, B00). It also shows, at least out to 400 arcsec from the cluster center and possibly beyond that, two statistically significant gaps at $T_{\rm eff}$ = 15,900K and $T_{\rm eff}$ = 25,400 K (B00). Because of these properties, and of its considerable mass ($M_{V_{tot}}$=

-9.36 mag), NGC 2808 is an interesting target from the dynamical point of view. A jump in the Johnson U,B,V photometry has been observed in its HB at (U-B)= -0.11 ± 0.03, corresponding to T_{eff} = 11,600 ± 350 K (B00). The 16 stars included in our program were also selected from B00.

- **NGC 6093 (M80).**- It is another well known BT cluster, with an HB reaching about T_{eff} = 30,000 K. Three gaps at T_{eff}= 9,500 K, T_{eff}= 11,000 K and T_{eff}= 18,000 K are clearly visible in the ultraviolet photometry of Ferraro et al. (1998). The cooler one, labeled G0 by Ferraro et al. (1998) is also present at the same temperature (or mass) in other BT clusters as M13 and M15. Nine stars among our M80 targets were taken from the Piotto et al. (2002) photometry. Five additional stars of M80 were selected from the Johnson VI photometry by Rosenberg et al. (2000) in more external regions.

- **NGC 7078 (M15).**-This cluster is the most metal poor target ([Fe/H]= -2.2) in our sample, and the only one which has undergone core collapse (Djorgovski et al. 1989). Its BT reaches effective temperatures around 30,000 K and presents a gap at T_{eff} = 9,000 K (Ferraro et al. 1998). Behr at al. (2000b) have already analyzed 18 HB stars in this cluster with the purpose of measuring stellar rotations and abundances. We have re-observed two of the stars in their sample in order to test the consistency between the two sets of observations and the different methods adopted for the rotational velocity measurements. Furthermore, as the gap in the M15 BT is quite cooler than the temperature of the jump, improving statistics in this cluster can allow us to explore if the abrupt change in the $v\sin i$ distribution along the BT is related to the first or to the second feature, which can lead to very quite different theoretical interpretation.

3.1.1 Colour-magnitude diagrams and finding charts.

The CMDs of each of the four target clusters of our program are shown in Figure 3.1, with the selected stars marked. The related finding charts for each of them are sumarized in Table 3.2. Figure 3.2 labels the target stars in NGC 2808. Figure 3.3 is a zoomed finding chart for the star n2808-3841. The orientation and dimensions of the UVES slit are marked.

3.2 UVES+VLT spectroscopy: observations and reduction.

3.2.1 Instrument configuration and observing runs.

The UV-Visual Echelle Spectrograph (UVES) is mounted on the VLT telescope Kueyen (UT2), at the European Southern Observatory of Cerro Paranal,

Cluster	**Reference**
M79	Stetson & Harris (1977) Piotto et al. (2002) Grundahl et al. (1999)
NGC 2808	Bedin et al. (2000)
M80	Rosenberg et al. (1999) Piotto et al. (2000)
M15	Piotto et al. (2002)

TABLE 3.2— Finding charts for program stars.

Chile. UVES is a two-arm crossdispersed echelle spectrograph, covering the wavelength range 300 - 500 nm (blue) and 420 - 1100 nm (red). The spectral resolution for a 1 arcsec slit (as the one used in our observations) is about 40 000. Four different cross-disperser gratings (two for the "blue arm" and two for the "red arm") are available. For this program, we are using the UVES blue arm, with the CD2 cross-disperser grating: 660 g/mm, blaze waveleght 460 nm; so the spectral coverage of the data is within 373 - 499 nm.

The observations were carried out with the 2K x 4K, 15 μm pixel size blue CCD, with a readout noise of 3.90 e^- and a conversion factor of 2.04 e^-/ADU. Using the UVES blue arm combined with a slit width of 1.0 arcsec, we achieved a resolution of $\sim$ 0.1 $\mathring{A}$ (7.5 km/s). The spectra were obtained during 3 observing runs: July 30–August 2 2000, January 19–23 2001, and March 1–7 2002 (service mode). Signal to noise ratios (S/N) were always $\geq$ 10 per resolution element. In general, all the targets lie in the low-crowding outskirts of the parent cluster, to avoid contamination from other stars. In general, we limited individual exposure times to 1800-2700 seconds to minimize cosmic ray accumulation, and then coadded three to four frames per star (see Table 3.3). During each observing run, we also collected high S/N spectra of a set of field rotational velocity standards (Peterson 1983), with spectral types close to those of our program stars: HD74721 ($v\sin i$=3$\pm$3 km/s), HD130095 ($v\sin i$=3$\pm$3 km/s), HD117880 ($v\sin i$=12$\pm$3 km/s), HD19445 ($v\sin i$=13$\pm$3 km/s), and HD109995 ($v\sin i$=27$\pm$3 km/s).

Tabel 3.3 gives the exposure times for each of the target stars, and their magnitude in the u, V, or $F555W$ filter.

3.2.2 Reduccion

Standard IRAF procedures were used to reduce the UVES echellograms to one-dimensional spectra. The frames, bias-subtracted, flat-fielded, and cleaned of

cosmic-ray hits, were treated in a uniform way.

Order tracing and extraction: For each echellogram image the IRAF procedure APTRACE, determines the position of the spectrum within each aperture (previously identificated using APFIND) at a number of points along the dispersion axis and a high-order polynomial is fit to these positions. The fitted curve defines a shift to be added to the aperture center at each wavelength. The scattered light outside the apertures defining the two dimensional spectra is extracted, smoothed, and subtracted from each input image. Finally, using APSUM, each order is extracted into a one-dimensional spectrum, by summing the pixels within a box centered on the order trace. The task APFIND allows to adjust the box width depending on the the star's spatial profile, which is a function of seeing and telescope focus. We traced orders on each target exposure separately, instead of coadding multiple exposures, because the exact shape and position of each order depends on the telecope pointing and amount of atmospheric dispersion.

Calibration: For the wavelenght calibration we fitted 4^{th} order polynomials to the dispersion relations of the ThAr calibration spectra, which resulted in residuals $\leq 3{\cdot}10^{-4}$ Å. To this purpose, we used the ECREIDENTIFY, REFSPECTRA and DISPCOR procedures within IRAF.

Preparation for cross-correlation analysis: Each spectrum was divided into sections of about 40 Å, which, avoiding hydrogen and helium lines, in general coincided with the echelle UVES orders. Finally, each spectrum was normalized using a polimomial fitting.

Figure 3.4 shows a section of the normalized spectra of the target star n2808-2333 and the field standard HD74721.

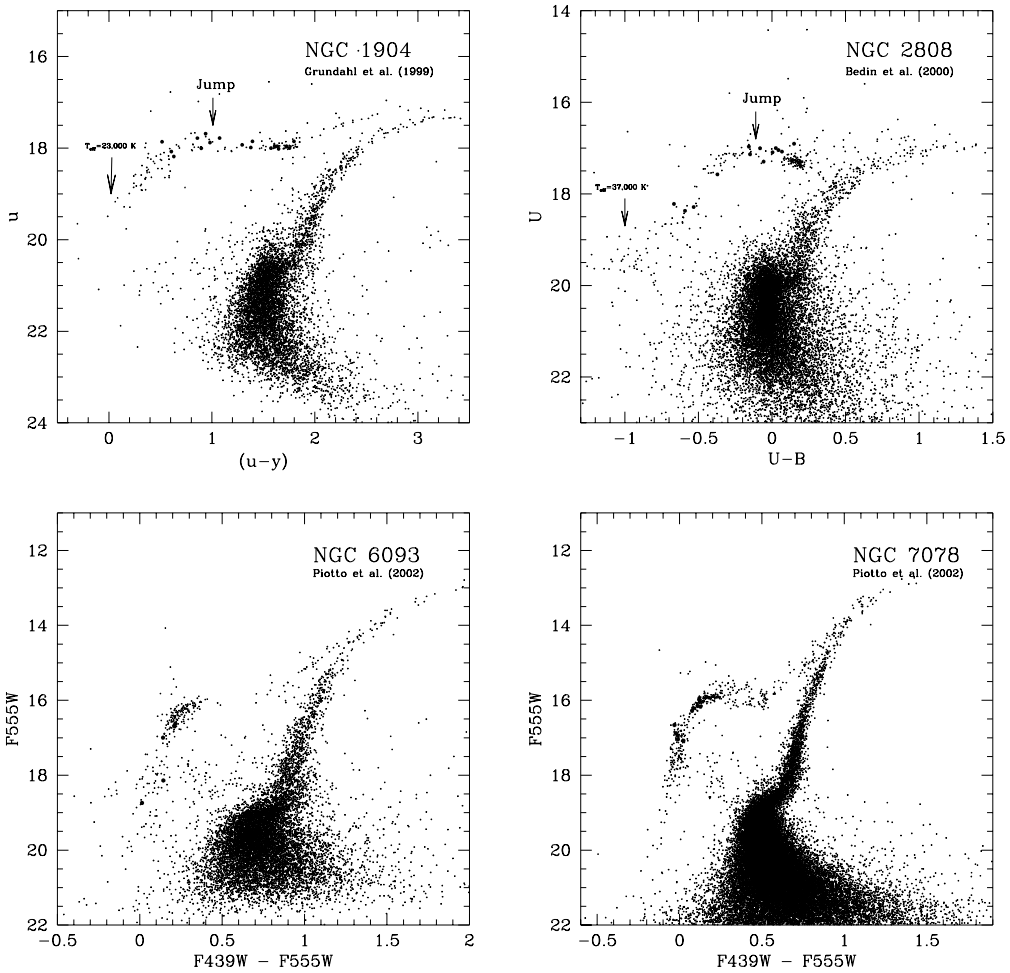


FIGURE 3.1— The target cluster CMDs with their corresponding selected stars.

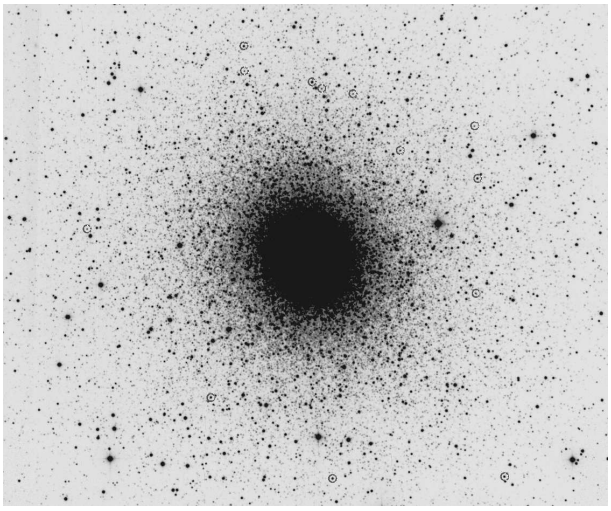


FIGURE 3.2— Finding chart for the NGC 2808 targets. North is up, east is left.

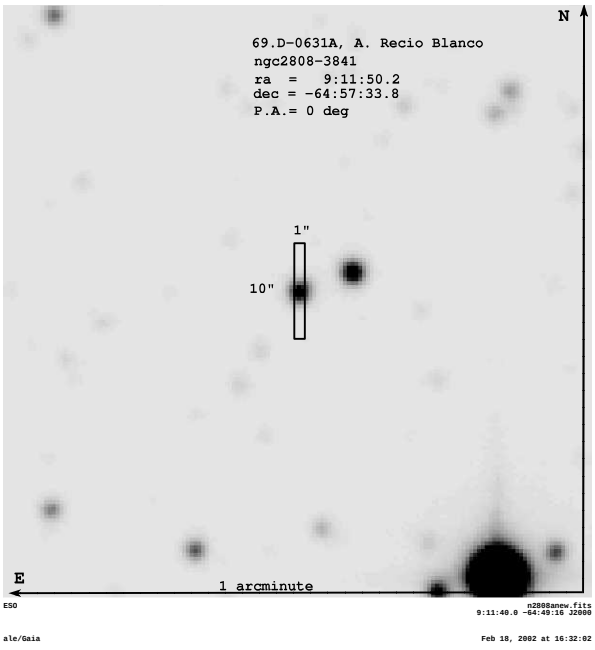


FIGURE 3.3— Finding chart for the star NGC2808-3841, with the UVES slit position and dimensions.

Star	u	$\mathbf{t}_{exp}$ **(s)**	**Star**	u	$\mathbf{t}_{exp}$ **(s)**
m79-489	17.86	2 x 1250	m79-327	18.00	800
m79-535	18.08	2900	m79-281	17.96	800
m79-555	18.18	2 x 1200	m79-298	17.97	800
m79-434	17.78	2300	m79-289	17.96	800
m79-469	18.00	2000	m79-295	18.02	1080
m79-392	17.68	4000	m79-275	17.97	600
m79-363	17.88	2800	m79-243	17.96	800
m79-389	17.78	2000	m79-294	18.00	600
m79-354	17.93	1360	m79-209	17.85	800
m79-366	17.99	1400	m79-297	17.85	900
Star	U	$\mathbf{t}_{exp}$ **(s)**	**Star**	U	$\mathbf{t}_{exp}$ **(s)**
n2808-7596	17.71	4 x 1650	n2808-4991	17.29	2500
n2808-9432	18.22	3 x 2840	n2808-2909	16.90	2700
n2808-11222	18.37	3 x 2700	n2808-3721	17.09	2700
n2808-9655	18.29	3 x 2660	n2808-3435	17.00	2700
n2808-6427	17.57	2 x 1900	n2808-3841	17.04	2700
n2808-3159	16.97	2500	n2808-3949	17.08	1800
n2808-4512	17.14	2500	n2808-2333	16.80	2700
n2808-3715	17.00	1800	n2808-2445	16.85	2700
Star	$F555W$	$\mathbf{t}_{exp}$ **(s)**	**Star**	V	$\mathbf{t}_{exp}$ **(s)**
m80-509	16.62	1800	m80-107	16.88	1100
m80-820	16.68	1800	m80-109	16.86	1100
m80-1400	18.14	3 x 1800	m80-83	16.57	900
m80-2044	17.00	2 x 1200	m80-1149	18.15	2 x 1800
m80-2242	18.74	3 x 1800	m80-454	18.70	4 x 1800
m80-938	16.89	1800			
Star	V	$\mathbf{t}_{exp}$ **(s)**	**Star**	V	$\mathbf{t}_{exp}$ **(s)**
m15-1813	16.04	1200	m15-5168	16.88	1500
m15-5516	16.28	800	m15-768	16.94	1500
m15-6143	16.21	900	m15-817	17.04	1500
m15-2700	16.66	1500	m15-b130	15.96	900
m15-2917	15.98	800	m15-b218	15.99	1200
m15-3333	16.17	1200	m15-1048	16.79	1500
m15-4047	16.15	800	m15-699	16.63	1500
m15-4536	17.08	1500	m15-788	15.94	900

TABLE 3.3— Photometric information and exposure times for the target stars.

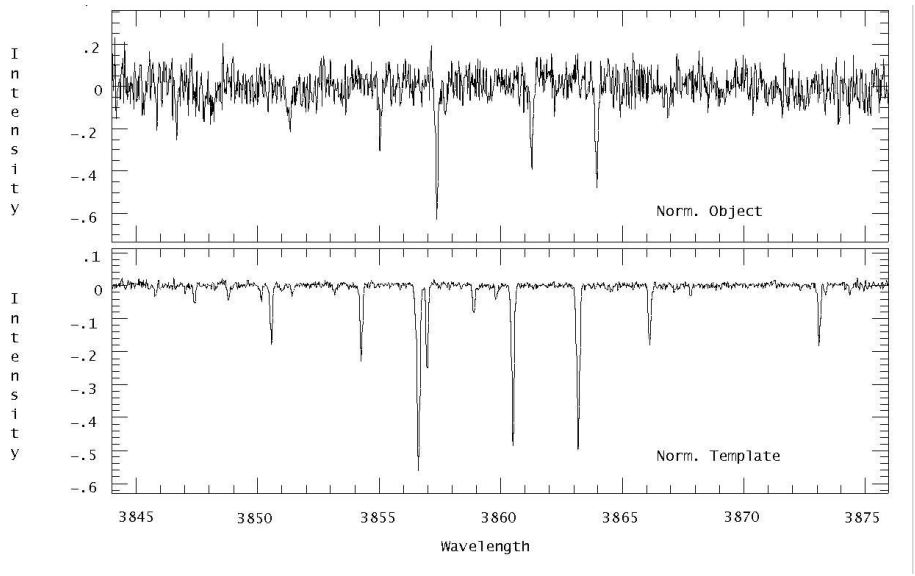


FIGURE 3.4— Normalized section of the spectrum of the target star n2808-2333 (top pannel) and the template HD74721 (bottom pannel).

4

Analysis procedures: rotation and abundances.

OUR analysis techniques for the rotational velocity and abundance measurements are reviewed in the following sections.

4.1 Rotational velocity measurements

We determined the radial velocity (v_{rad}) and the projected rotational velocity ($v\sin i$) for each of our program stars using the cross-correlation technique described by Tonry & Davis (1979,TD79). This method is well suitable to measure v_{rad} and rotational broadening in low signal-to-noise spectra (Dubath et al. 1990).

4.1.1 Cross-correlation analysis

The analysis procedure computes (in the Fourier domain) the cross-correlation function (CCF) of the object spectrum versus that of a template, fits a gaussian to the highest peak, and finds the radial velocity and the line broadening from the peak's central position (δ) and width (σ). If both spectra are very narrow-lined, there is little tolerance for radial velocity displacements, and the peak falls off rapidly; if one or the other is somewhat broad-lined, the falloff is gradual, and the correlation peak is broader. The cross-correlation procedure was performed using the task *fxcor* within IRAF. For the gaussian fit of the CCF peak the parameters used were the center position, amplitude, width and background level. The heliocentric correction for each spectrum was also computed on the basis of its observational coordinates and time. We used the slow rotating

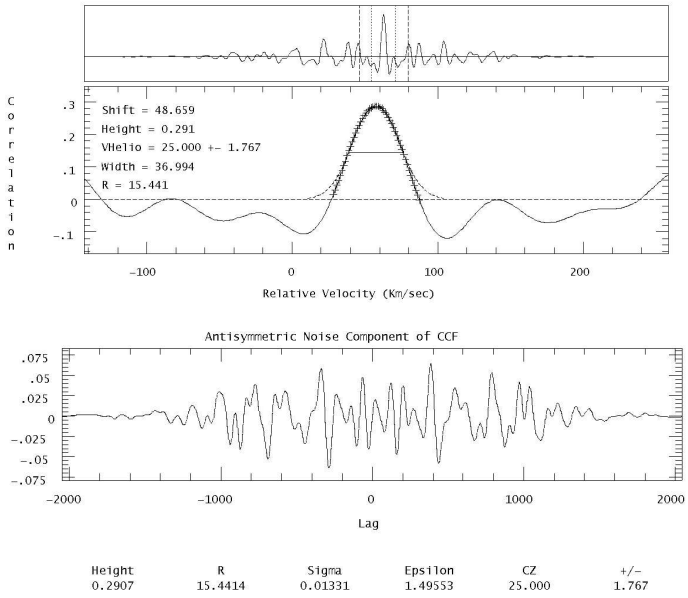


FIGURE 4.1— Example of a cross-correlation function (top panel) and its antisymmetric part (bottom panel) between the target star n2808-2333 and the template HD74721. The values of the r, ϵ, σ_a parameters are also provided.

($v\sin i < 6$ km/s) blue HB field stars HD74721 (v_{rad}=30.7 km/s) and HD130095 (v_{rad}=66.0 km/s) as templates for the cross-correlation. Those CCFs for which the peak's central position did not agree with the correct stellar radial velocity, relative to the template, were rejected. In this way, we avoided the errors due to line mismatch or to the lack of spectral features, especially for the hottest stars and the reddest sections of the spectra. A mean of 15 different CCFs could be used for each program star, each of them providing a value of δ and σ. In addition, using δ as the center position, the antisymmetric part of the correlation function is calculated, and its rms (σ_a) is derived. This allows the calculation of the velocity error (ϵ) via the "r" parameter, as described by TD79:

$$\mathrm{r}= h/(\sqrt{2}\sigma_a)$$
$$\epsilon = N/(8B(1+r))$$

where h is the height of the cross-correlation peak, N is the number of bins in which the spectrum is mapped (2048 in our case) and B is the highest wave number where the Fourier transform of the CCF has appreciable amplitude (e.g. the half-maximum point).

To calculate the radial velocity of each program star, we computed the mean (δ_{mean}) of the δ values of all the good CCFs involving that star, weighted to the inverse of their errors ($1/\epsilon$). The final v_{rad_o} of the object star is:

$$v_{rad_o} = v_{rad_t} + \delta_{mean}$$

where v_{rad_t} is the radial velocity of the template taken form the literature (Kinman et al 2000). Hence, the error:

$$\epsilon(v_{rad_o}) = \sqrt{\epsilon^2(v_{rad_t}) + \epsilon^2(\delta_{mean})}$$

Similarly, after the appropriate calibration, we obtained the $v\sin i$ for each target from the value of σ, as explained in the following section. Figure 4.1 shows an example of the CCFs obtained and fitted. The target star is n2808-2333, and the template is HD74721. The corresponding normalized spectra sections were presented in Figure 3.3.

4.1.2 Projected rotational velocity measurements

The width (σ) of the CCF of a star results from several broadening mechanisms which depend on, for instance, gravity, turbulence, magnetic fields, effective temperature, metallicity, rotation. In addition, the instrumental profile also contributes to the broadening of the spectrum and therefore to the CCF. Thus, in order to correctly measure the rotational contribution to the width of the

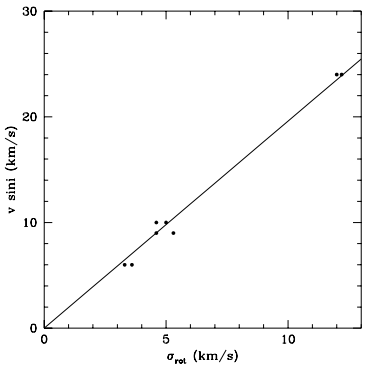


FIGURE 4.2— Calibration of the differential broadening of the CCF to the projected rotational velocity $v\sin i$ for the standard stars taken from Peterson et al. (1983).

CCF, we must model the contributions of the broadening mechanisms other than rotation, that is, calibrate the σ - $v\sin i$ relation for the instrument and the stars we are working with. In the case of a gaussian fit of the CCF peak, the rotational broadening will correspond to a quadratic broadening of the CCF:

$$\sigma^2 = \sigma_{rot}^2 + \sigma_o^2 \Rightarrow \sigma_{rot}^2 = \sigma^2 - \sigma_o^2$$

where σ is the width of the CCF, σ_{rot}^2 is the rotational broadening, and σ_o^2 is the width of the CCF of the non rotating star. Therefore, the projected rotational velocity $v\sin i$ is given by (Benz & Mayor 1984):

$$v\sin i = A \cdot \sqrt{\sigma^2 - \sigma_o^2} = A \cdot \sigma_{rot} \quad (1)$$

where A is a constant coupling the differential broadening of the CCF to the $v\sin i$ of the stars. The value of A in the previous equation was found by fitting a straight line to the relation, $v\sin i$ versus σ_{rot}, for all the field standards of rotation. The slope gives A. The mean value $< A > = 1.8 \pm 0.7$ km/s was adopted (see Figure 4.3).

As explained by Melo et al (2001), there is also a smooth dependence on σ_o on the stellar colour and luminosity class. However, the variation of σ_o within the range of our program and template stars is expected to be very small (< 0.1 km/s) compared to the accuracy of our σ measurements ($\sim$ 3-6 km/s), due to the relatively small number of lines and the low S/N for our spectra. Moreover, we have an error of 3 km/s in the $v\sin i$ values of the templates. For this reason, we decided to estimate the value of σ_o by correlating one template with the other, for each one of the orders used to measure the $v\sin i$ of the target stars.

In order to derive the final $v\sin i$ for each program star, we calculated the mean of the $v\sin i$ values given by the individual σ determinations for all the good CCFs (15 on average) involving that star. We used as weight the height of the cross-correlation peak.

The error of each $v\sin i$ measurement can be obtained by error propagation from Eq. 1:

$$|\Delta(v\sin i)|_{mes} = A^2\sqrt{(\epsilon\sigma)^2 + (\epsilon_o\sigma_o)^2}/v\sin i$$

where ϵ and ϵ_o are the velocity errors for the CCF and the template to template CCF respectively and we have neglected the error in A. To this we have to add the error in the $v\sin i$ of the templates.Thus, the total error on $v\sin i$ is:

$$|\Delta(v\sin i)|_{tot} = \sqrt{|\Delta(vsini)|^2_{mes} + |\Delta(vsini)|^2_t}$$

with $|\Delta(v\sin i)|_t$ being 3 km/s in the case of HD74721 and HD130095.

4.2 Abundance measurements

We have performed an abundance analysis of 10 stars in M79. The S/N of the analyzed spectra was $\sim$ 25 per pixel (as for the star m79-392), or this value was achieved by rebinning 2x2 the spectra (for the errors in this procedure see Cayrel, 1988). The abundance measurements were obtained using the program WIDTH3, developed by R. Gratton, and adapted by D. Fabbian for temperatures up to $T_{eff} \simeq$ 20,000 K (see D. Fabbian graduate thesis). The procedure establishes the abundances of chemical species by reproducing the observed equivalent widths. Once a starting set of values for the effective temperature, the surface gravity, and the model metal abundance are derived (see section 4.2.3), an appropriate model for each star is obtained from the grid of model atmospheres by Kurucz (1998) by interpolating lineary in the temperature and logarithmically to get the Rosseland opacity, electronic and gaseous pressure and density. The abundances are then derived by computing the continuum opacity, taking into account all the important continuum opacity sources for stars as hot as $T_{\rm eff} = 20,000$ K: HI, H^-, H^{++}, HeI, CI, AlI, MgI, SiI, Rayleigh and Thomson diffusion. The opacity contribution due to the atomic lines is considered via the *Opacity Sampling* technique, using the line lists by R. Kurucz. Collisional damping constants are computed with the Unsöld formula. The equation of transfer is then integrated through the atmosphere and theoretical equivalent widths of the lines computed and compared with the observed ones. The consistency of the program and the reliability of its results has been tested by D. Fabbian on 4 M13 stars, previously observed by Behr et al. (1999), using

their equivalent widths measurements and atmospheric parameters and yielding the same abundance results.

4.2.1 Line selection, oscillator strengths, and solar abundances

Only lines clean from blends were considered in the analysis. The line list was extracted from the solar spectrum lines included in Moore et al. (1966), and the atomic line lists by Hambly et al. (1997) and Kurucz & Bell (1995).

For the determination of the oscillator strength values (*gf*s), laboratory strengths were considered whenever possible. For Fe I lines they were taken from papers of the Oxford group (Simmons & Blackwell 1982) and Bard & Kock (1994). The *gf*s for the FeII lines were taken from Heise & Kock (1990) and Biemont et al. (1991). *gf*s for the MgI and MgII lines come from Gratton (2002). Finally, for the rest of the lines, the *gf*s are the ones provided by Kurucz (1998) and the National Institute of Standards and Technology (NIST) atomic spectra database.

The solar abundances are taken from Grevesse & Sauval (1998).

4.2.2 Equivalent Widths

Equivalent Widths (EWs) were measured on the unidimensional, extracted spectral orders using an automatic routine within the ISA package, prepared by R. Gratton (see Bragaglia et al. 2001). The routine works as follows. First, removal of the blaze function response is performed using a spline interpolating function. Then, a local continuum level is determined for each line by an iterative clipping average over a fraction (the highest ones) of the 200 spectral points centered on the line to be measured. Second, the equivalent width for each line from an extensive list is tentatively measured using a Gaussian fitting routine. Measures are rejected according to several criteria (e.g., if the central wavelength does not agree with that expected from a preliminary measure of the geocentric radial velocity or if the lines are too broad or too narrow).

Only lines with EW $>$ 10 m$\AA$ were considered. The number of measured lines depends on the S/N and on the star metallicity. In appendix, we show the equivalent width measurements for each of the lines considered in the target spectra, with the corresponding abundance derived by WIDTH3.

Due to the quality of the spectra, the most important error in the abundance determination comes from the equivalent width uncertainties. If we evaluate this error via the Cayrel (1988) formula:

$\Delta(EW) = 1.6\sqrt{(wdx)}/(S/N)$

with w being the full width at have maximum (FWHM) typical of the lines, in this case $\sim$ 0.12 $\AA$, and dx being the dispersion, about 0.03 $\AA$. With a

(S/N)$\simeq$10, we get $\Delta(EW))\simeq$10 m$\AA$. Although none of the target spectra is repeated, we can test this result by comparing the equivalent width measurements of the stars m79-209 and m79-281. These stars have almost equal atmospheric parameters, with differences inside the errors. In addition, they do not present signs on diffusive effects in their atmospheres. An analysis of 22 lines measured in both spectra, indicates that the mean difference between the two equivalent width measurements is -1.1 m$\AA$, with a standard deviation of 14.7 m$\AA$. Therefore, assuming that equivalent width errors for both stars are the same, the error for each measurement is 14.7 / $\sqrt{2}$ = 10.4 m$\AA$, thus, more or less the same value obtained via Cayrel's formula.

Consequently, we have calculated the abundance errors, derived from an equivalent width uncertainty of 10.4 m$\AA$, comparing the element abundances derived for a measured equivalent width, EW, and those with EW + 10.4 m$\AA$. The resulting errors for the star m79-392, $\sigma_{log\epsilon}(\Delta EW)$, are shown in Table 4.1, column 2.

Element	$\sigma_{log\epsilon}(\Delta EW)$	$\sigma_{log\epsilon}(\Delta T)$	$\sigma_{log\epsilon}(\Delta g)$	$\sigma_{log\epsilon}(\Delta \xi)$	$\sigma_{(}\Delta z)$
HeI	0.3	0.11	0.06	0.02	0.09
MgII	0.2	0.02	0.01	0.08	0.00
SiII	0.2	0.02	0.03	0.03	0.01
PII	0.2	0.02	0.03	0.05	0.01
CaII	0.4	0.05	0.04	0.22	0.01
TiII	0.2	0.09	0.00	0.05	0.02
CrII	0.2	0.04	0.02	0.03	0.02
MnII	0.2	0.03	0.02	0.02	0.01
FeI	0.2	0.10	0.03	0.05	0.04
FeII	0.2	0.02	0.03	0.09	0.01
YII	0.2	0.10	0.02	0.04	0.03

TABLE 4.1— Abundance errors for the star m79-392, due to an uncertain of 10.4 m$\AA$ in equivalent width, σ_{EW}, 200 K in effective temperature, σ_T, 0.1 in log g, σ_g, and 0.3 dex in [A/H], σ_z.

4.2.3 Atmospheric parameters

Model atmospheres appropriate for each star were extracted from the grid of Kurucz (1998). T_{eff} values are determined from the position of the stars in the u,$(u-y)$ CMD by Grundahl et al. (1999), and the position in a Johnson U,$(U-V)$ CMD by Momany (2003), using the models by Cassisi et al. (1999), as shown in Figure 4.3.

Table 4.2 presents the photometric parameters for all the target stars in M79 and the corresponding temperature values derived from the Grundahl et al. (1999) CMD, T_{effg}, and the Momany (2003) CMD, T_{effm}. Only 10 of

these stars, selected among the slow rotating ones, were used in the abundance analysis.

Effective temperature.

To derive the final effective temperature of the program stars, we calculate the mean of the Momany's temperatures and the Grundahl temperatures reported to the Momany's scale. The final error is the scatter of the temperatures involved in the mean. We decided to report T_{effg} to T_{effm} mainly because the T_{effg} scale presented a number of problems. First, the T_{effg} temperature for the coolest stars would place them inside the RRLyrae instability strip, and the corresponding metallicity for such a cool temperature would be lower than what reported for the RGB stars in the cluster. On the other hand, apart from this shift to cooler temperatures, probably due to the ZAHB model fit, all of our targets were well identified in the Grundahl et al. photometry, at variance with the Momany's photometry, where 3 of the stars were blended. For this reason, and to be sure of an internal consistency of all the temperature measurements, we decided to report the T_{effg} values to the Momany's scale, and then calculate the mean, for each star, of the new T_{effg} obtained and the T_{effm} value.

The relation between T_{effg} and T_{effm} has been found by first fitting T_{effg} to T_{effm} and inverting the relation:

$T_{effg} = (1.339 \pm 0.071)\ T_{effm}$ - (3890 ± 483) K

$T_{effm} = (0.746 \pm 0.040)\ T_{effg} + (2905 \pm 361)$ K (4.1)

And then fitting T_{effm} to T_{effg} directly :

$T_{effm} = (0.716 \pm 0.038)\ T_{effg} + (3205 \pm 353)$ K (4.2)

We've used this method because, in principle, we did not have an idea of the individual errors in T_{effm} or T_{effg}. So the corrected temperature in the Grundahl's scale is the mean of 4.1 and 4.2:

$T_{effgc} = (0.731 \pm 0.039)\ T_{effg} + (3055 \pm 357)$ K

Finally, we adopted our target star's effective temperatures as the mean of T_{effgc} and T_{effm} (see Table 4.3).

Gravity and microturbulence.

We have then derived, from Behr et al. (1999) measurements of blue HB stars in M13, a relation between $\log(T_{\rm eff})$ and gravity ($\log g$):

$$\log g = 4.83 \cdot \log(T_{\rm eff}) - 15.74$$

And a relation between $\log(T_{\rm eff})$ and the microturbolence velocity, ξ:

$$\xi = -4.7 \cdot \log(T_{\rm eff}) + 20.9$$

ID	y	b	v	u	V	B	U	T_{effg} (K)	T_{effm} (K)
243	16.23	16.29	16.47	17.96	16.29	16.31	16.44	7700	8500
209	16.06	16.14	16.34	17.85	16.11	16.16	16.29	7500	8400
294	16.24	16.31	16.49	18.00	16.30	16.32	16.46	7600	8600
295	16.37	16.41	16.56	18.02	-	-	-	8000	-
289	16.32	16.37	16.52	17.96	16.37	16.36	16.45	8100	9000
275	16.25	16.31	16.48	17.97	16.32	16.32	16.44	7700	8800
297	16.46	16.47	16.57	17.85	16.51	16.43	16.39	9300	10200
327	16.43	16.46	16.61	18.00	16.48	16.45	16.50	8400	9400
292	16.25	16.32	16.50	18.00	16.29	16.37	16.49	-	8400
281	16.35	16.38	16.53	17.96	16.36	16.41	16.49	8200	8800
298	16.35	16.38	16.53	17.97	16.37	16.40	16.48	8200	8900
489	17.34	17.31	17.35	17.86	17.42	17.24	16.72	14500	13000
354	16.64	16.67	16.79	17.93	16.73	16.67	16.58	9800	10600
469	17.11	17.10	17.16	18.00	17.17	17.03	16.71	12300	12200
434	16.92	16.92	16.99	17.78	16.99	16.86	16.61	12300	11600
389	16.71	16.70	16.77	17.78	16.77	16.65	16.43	11000	11200
363	16.90	16.92	17.01	17.88	17.45	17.32	17.07	11800	-
366	16.61	16.62	16.74	17.99	16.67	16.61	16.56	9400	10200
555	17.55	17.51	17.56	18.18	17.60	17.44	16.99	13700	13800
392	16.74	16.74	16.81	17.68	16.82	16.67	16.37	12100	11500
535	17.47	17.47	17.54	18.08	18.07	18.14	17.50	13700	-

TABLE 4.2— photometric parameters for all the target stars in M79 and the corresponding temperature values derived from the Grundahl et al. (1999) CMD, T_{effg}, and the Momany (2003) CMD, T_{effm}.

The above relations were used to determine the gravity and the microturbulence for our target stars, with the corresponding temperature values previously calculated. The resulting values are presented in Table 4.3.

Metallicities were obtained varying the metal abundance [A/H] of the model until it was equal to the derived [Fe/H] value. The adopted atmospheric parameters are listed in Table 4.2.

Once, T_{eff}, log g, ξ and atmospheric [Fe/H] (which we will called z) are determined, we calculate the mean abundance and dispersion for each element. Since the log ϵ for each element is dependent upon the adopted parameters, we recalculate the abundances while varying each of these parameters in turn, and seeing how much the abundances change as a result. More specifically, we determined:

$$\begin{aligned}
\sigma_{log\epsilon}(\Delta T) &= log\epsilon(T_{eff}+\sigma_T, g, \xi, z) - log\epsilon(T_{eff}, g, \xi, z) \\
\sigma_{log\epsilon}(\Delta g) &= log\epsilon(T_{eff}, g+\sigma_g, \xi, z) - log\epsilon(T_{eff}, g, \xi, z) \\
\sigma_{log\epsilon}(\Delta \xi) &= log\epsilon(T_{eff}, g, \xi+\sigma_\xi, z) - log\epsilon(T_{eff}, g, \xi, z) \\
\sigma_{log\epsilon}(\Delta z) &= log\epsilon(T_{eff}, g, \xi, z+\sigma_z) - log\epsilon(T_{eff}, g, \xi, z)
\end{aligned}$$

for each element. And example of the resulting errors for the star m79-392 are shown in Table 4.1, columns 3 to 6.

star	$T_{\rm eff}$	$\log g$	ξ
m79-209	8469 ± 200	3.2 ± 0.2	2 ± 1
m79-281	8925 ± 200	3.3 ± 0.2	2 ± 1
m79-354	10409 ± 200	3.7 ± 0.1	2 ± 1
m79-389	11148 ± 200	3.8 ± 0.1	2 ± 1
m79-363	11681 ± 300	3.9 ± 0.1	2 ± 1
m79-392	11700 ± 200	3.9 ± 0.1	2 ± 1
m79-434	11823 ± 200	3.9 ± 0.1	2 ± 1
m79-469	12123 ± 200	4.0 ± 0.1	2 ± 1
m79-535	13070 ± 300	4.1 ± 0.1	1 ± 1
m79-489	13327 ± 200	4.2 ± 0.1	1 ± 1

TABLE 4.3— Photospheric parameters for the program stars for which an abundance analysis has been performed.

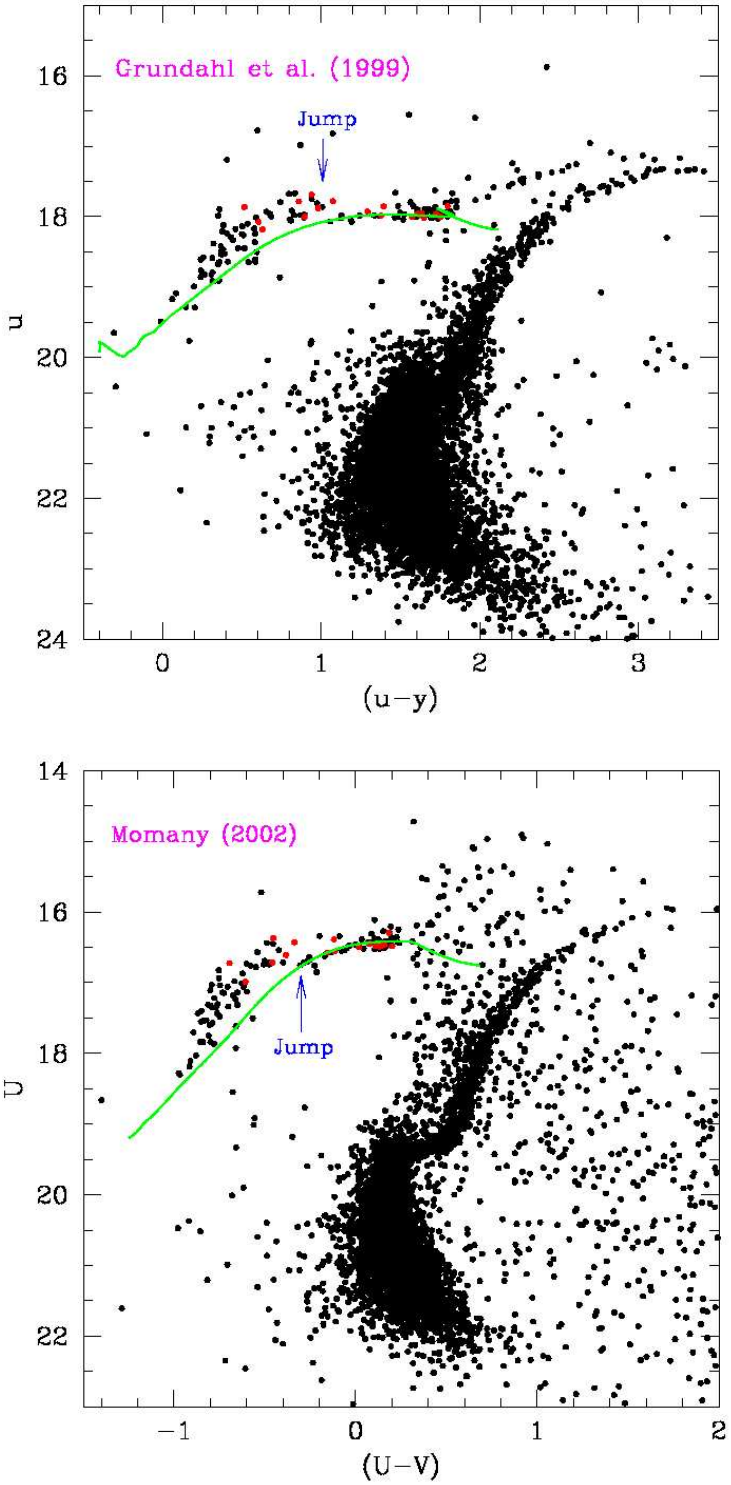


FIGURE 4.3— All the target stars (red dots) identified in the M79 colour-magnitude diagrams by Grundahl et al. (1999) and Momany (2003). ZAHB models by S. Cassisi are plotted in green. The location of the luminosity jump is marked with an arrow in both CMDs.

5

Results and Discussion.

In this chapter, we present the results of the rotation and abundance analysis. We indicate trends and patterns in these data and we discuss their possible theoretical implications.

5.1 Rotational velocity.

5.1.1 Results.

The final results for a dataset of 61 stars in the clusters NGC 1904 (M79), NGC 2808, NGC 6093 (M80) and NGC 7078 (M15) are presented in Table 5.1. For each target star (Column 1), the position (Columns 2 and 3), the photometric information (Columns 4 and 5), the effective temperature (Column 6), the radial velocity (Column 7), and the projected rotational velocity (Column 8) are given. The stars m15-b130 and m15-b218 are in common with Behr et al. (2000b). Our $v\sin i$ measurements and Behr et al. (2000b) values for this two stars are in agreement within the errors (5 $\pm$ 3 vs. 5.07 $\pm$ 0.24 and 13 $\pm$ 3 vs. 14.88 $\pm$ 0.69). This shows a consistency between the two sets of observations, and the two independent methods adopted for the rotational velocity measurement.

Figures 5.1 and 5.2 show the projected rotation results in our 4 GCs, plus the previous measurements in M13 (from Behr et al. 2000a and Peterson et al. 1995). For M15, we plot both ours and Behr et al. (2000b) data. An estimate of the $T_{\rm eff}$ for each star has been obtained by comparing the Cassisi et al. (1999) models with observed CMDs. In particular, we used the *uy* Strömgren photometry for M79 (Grundahl et al. 1999, G99); the Johnson *UB* for NGC 2808 (Bedin et al. , 2000), and the HST F439W and F555W for M80 and M15 (Piotto et al. 2002). Hence, there might be some offset in the temperature scale from

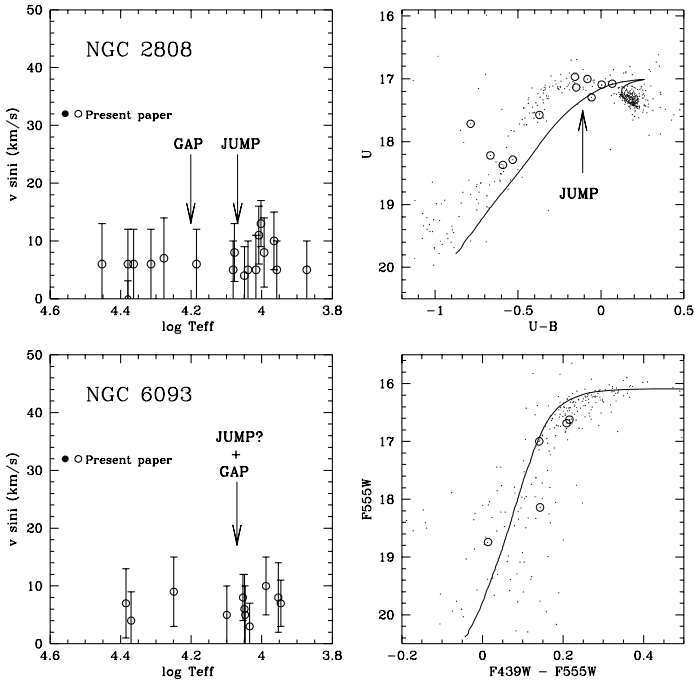


FIGURE 5.1— Left panel: Projected rotational velocities as a function of the temperature for our targets in NGC 2808 and M80 (open circles). The vertical arrows indicate the positions of the "gaps" (from Ferraro et al. 1998 and Piotto et al. 1999) and of the "jump" (from Grundahl et al. 1999). The position for the jump in M80 has not been confirmed by observations, yet. We just put the arrow in correspondence of $T_{\rm eff} = 11,500$K where all the HBs of Grundahl et al. (1999) GCs show this feature. Right panel: location of the target stars in the CMD. The full line represent the best fitting ZAHB from Cassisi et al. (1999).

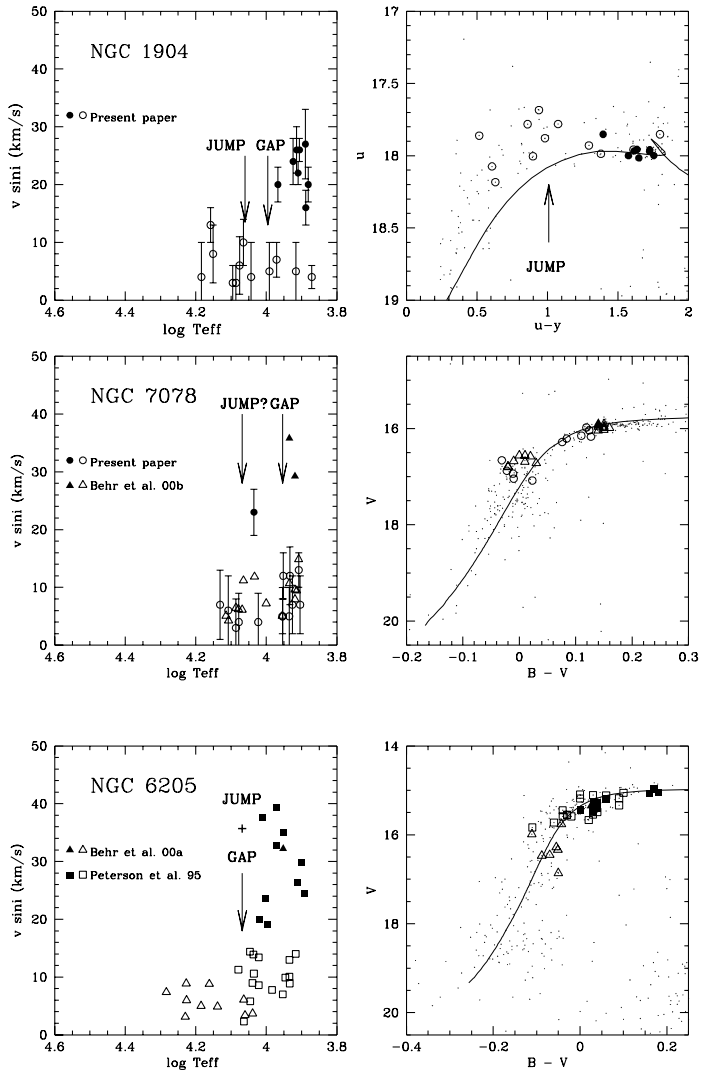


FIGURE 5.2— As in Fig. 5.1 for M79, M15, and M13. Full symbols show $v\sin i \geq 15$ km/s stars.

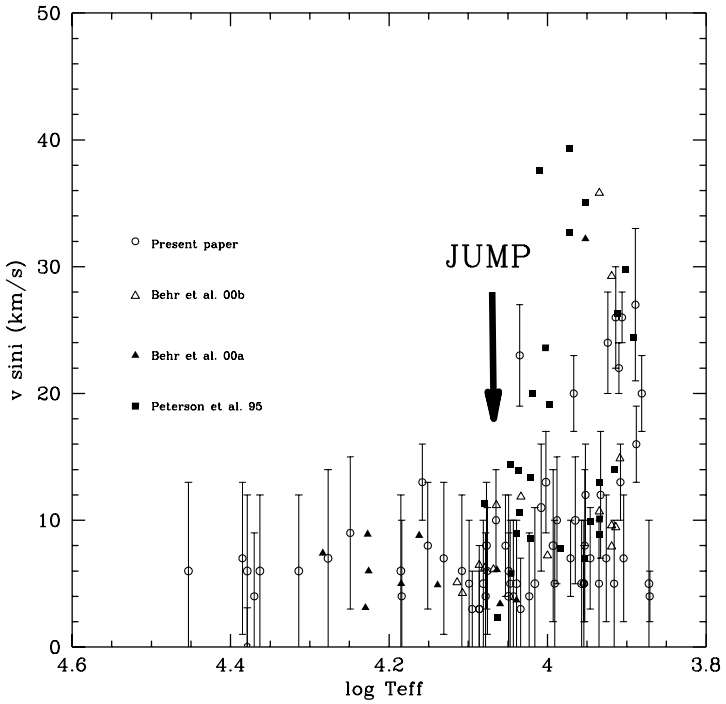


FIGURE 5.3— Projected rotational velocities as a function of the temperature for our targets (open circles) and the B00b (open triangles), B00a (full triangles) and P95 (full squares) measurements in M15 and M13. The vertical arrow indicates the position of the "jump" (from G99) in correspondence of $T_{\rm eff} = 11,500$K where all the HBs of G99 GCs show this feature.

GC to GC, in view of the different photometric systems (the temperatures for the M80 and M15 stars being the most uncertain ones), but for the purpose of this thesis only the relative position with respect to the HB gaps is relevant. It worths to point out, however, that a cross-check between our the Piotto et al. (2002) photometry, and the Grundahl et al. (1999) one, for the stars in M79, reveals that temperatures derived from both photometries are in agreement within the errors. The gaps on each GC HB are marked with arrows at the positions suggested by Hill et al. (1996) for M79 (T_{eff} = 9,900K), and F98 and P99 for the other GCs, i.e T_{eff}= 11,000K for M80; T_{eff} = 9,000K for M15; T_{eff} = 11,000K for M13. For NGC 2808 we adopted T_{eff} = 15,900K for the gap position, following Bedin et al. (2000). A second vertical arrow marks the position of the luminosity jump, taken from Grundahl et al. (1999).

Figure 5.3 shows, in a single graphic, the complete set of projected rotational velocity data from the previous 5 clusters: M79, NGC1904, M80, M15 and M13. Again, besides the data from this thesis (circles), Fig. 5.3 includes the Behr et al. (2000b) data for M15 (open triangles), plus the Behr et al. (2000a) (full triangles) and Peterson et al. (1995) (full squares) measurements for M13.

5.1.2 Distribution of rotational velocity along the blue HB and from cluster to cluster.

A first result from this investigation is that in all GCs *all the stars hotter than* $T_{eff} \sim$ *11,500 K have* $v sini \leq$ *12 km/s* (see Fig 5.1, 5.2 and 5.3). This finding is based on 116 stars in 5 GCs (including the 31 stars in M13 and M15 from Behr et al. 2000a and Behr et al. 2000b, and the 29 stars in M13 from Peterson et al. 1995). The measurements obviously provide $v\sin i$, but for an isotropic distribution in rotational axis large $\sin i$ are more likely than small ones, being for example the probability that $\sin i \leq 0.25$ about 3%. Therefore, the bulk of these stars must be intrinsically slow rotators.

In addition, our data reveal for the first time the presence in NGC 1904 of a sizable population of fast HB rotators ($v\sin i \geq 20$ km/s) confined to the cool end of the blue HB. The fast rotators already observed by Behr et al. (2000b) in M15 are also confirmed. Among the cooler stars (T_{eff} < 11,500 K) in these three GCs there is a range of rotation rates, with a group of stars rotating at $\sim$ 15 km/s or less, and a fast rotating group at $\sim$ 30 km/s. Apparently, the fast rotators are relatively more abundant in M79 and M13, than in M15, where only 3 stars out of 22 rotate faster than 15 km/s. In M79 and M13, at least half of our stars cooler than 11,500K are fast rotators. This implies *a different intrinsic distribution in the rotation rates of the EHB stars in these 3 GCs.* Neither the $v\sin i$ distribution in M13 and M79 nor that in M15 are as we could

expect from a constant rotation rate and a random orientation of the axis.

On the other hand, neither NGC 2808 nor M80 show any fast rotator. This may well result from too few HB stars cooler than 11,500K being included in our sample. However, there are quite many stars cooler than the gap, hence this result does not confirm the Behr et al. (2000a) suggestion that the abrupt change in the rotational velocity distribution was coincident with the presence of the BT gap. All GCs in the present study have a BT, and in all of them there is at least one gap. We were careful in having in all cases approximately half of the stars on either side of the gap, but Fig. 5.2 clearly indicates that the presence of fast rotators *is not* related to the presence of the gap. Indeed, in NGC 2808 and M80 there are 13 and 8 stars respectively on the cool side of the gap, and none of them has a rotational velocity exceeding 13 km/s. The likelihood that the small $v\sin i$ values on the cool side of the gap in NGC 2808 and M80 are due to casual almost polar orientation is very small, and therefore these stars are most likely intrinsic slow rotators. Notice also that one star in M15 with $v\sin i = 23\pm 3$ km/s is located significantly bluewards of the gap.

Therefore, our results indicate that *BT gaps are not related to the abrupt change in the rotational velocity distribution of the HB stars.* On the other hand, Fig. 5.2 indicates that all the fast rotators in M15 are cooler than $T_{\rm eff}$ ~11,500K, i.e. cooler than the location of the Grundahl et al. (1999) jump, rather suggesting a link between the presence of the jump and the absence of fast rotators among stars hotter than this temperature.

5.2 Abundance measurements.

In this section we present the results of the performed abundance analysis for 10 HB stars of the cluster NGC 1904 (M79). Tables 5.2 and 5.3 contain the abundance values derived for each of our target stars, both on absolute scale, and relative to the solar abundances of Grevesse & Sauval (1998). The scatter of the measurements for the corresponding lines gives the quantity σ_N, which is added quadratically to the error contributions in EW, T_{eff}, g, ξ and [A/H] described in the previous chapter, to get the final error for each element in each target star.

Figure 5.4 shows an example of growth curve, corresponding to the FeII abundance measurements for the star m79-392. Clearly, only unsaturated lines were used. In addition, no trend has been detected in the number of Fe atoms, log n(Fe), with the excitation potential, as expected for the excitation equilibrium.

The abundance values for the key elements are plotted in Figures 5.5 to 5.9 (red dots) as a function of T_{eff} as log offsets from the solar abundances.

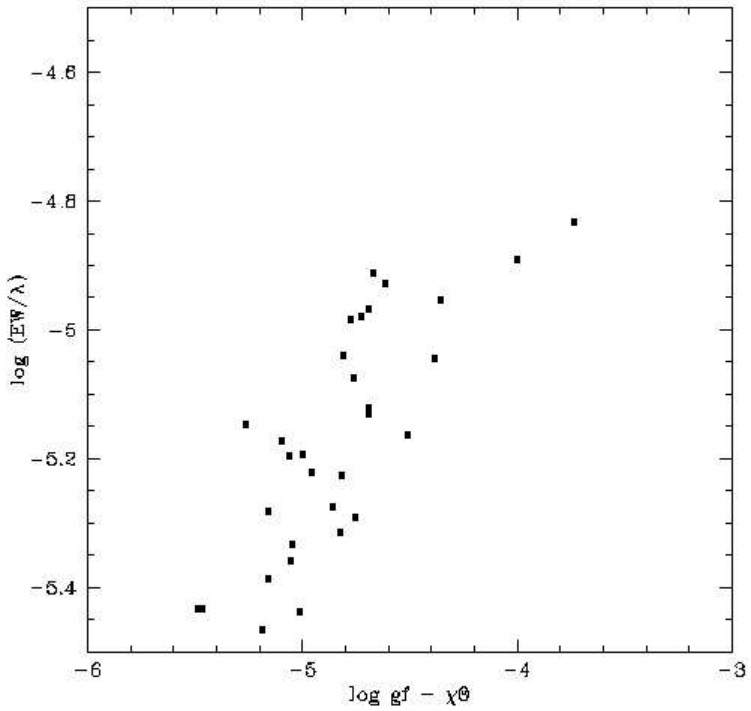


FIGURE 5.4— Curve of growth corresponding to the FeII abundance measurements for the star m79-392.

The abundance values from Behr et al. (2002) for M13 are also plotted for comparison as black circles and black stars. The last ones are data with an error in the effective temperature higher than 2000 K. The horizontal lines represent the expected value of [metal/H] from solar for M79 (in red) and M13 (in black), both in the Carretta & Gratton (1997) scale: dashed lines at -1.37 and -1.39, respectively; and in the Harris (1996) scale: solid lines at -1.54 and -1.57. For helium, the horizontal line represents the solar ratio. We used the abundance computed for the dominant ionization stage of each element, to minimize the possibility of non-LTE effects.

As we can see from Figures 5.5 to 5.9, we find remarkable enhancements of iron and other metal species among the blue HB stars hotter than $\sim$ 11000 K. The iron abundances of the coolest stars are close to the cluster metallicity. The first star with signs of radiative levitation is m79-354 at $T_eff = 10409 \pm 200$ K, with [Fe/H] $= -0.4 \pm 0.6$. All the stars hotter than $\sim$ 11000 K show iron content greater than that of the sun, [Fe/H]$\simeq$0.0 to +0.5. In a similar way, titanium is found a few tenths of a dex above the cluster baseline in the cooler stars, but then rises almost a factor of 100 in the hotter population. Some metals, such as phosphorus, display significantly larger enhancements than iron. We do not observe any PII lines among the cooler stars, but if we assume an appropriately-scaled solar composition for these stars, then the [P/H] $\simeq$ +1.5 that we find for the hot stars implies, in some cases, an enhancement of 3.5 orders of magnitude. In worths noting that a plethora of P II lines was found in the field HB stars Feige 86 and 3 Cen A by Sargent & Searle (1967) and Bidelman (1960), respectively, suggesting that the same mechanism may be at work in both cluster stars and field stars. On the other hand, Behr et al. (1999) found very similar P enhancements for hot HB stars in M13. Pronounced overabundances are also observed for chromium, manganese and yttrium. Silicon and calcium are also modestly enhanced to [X/H]$\simeq$-0.5 dex. The values for magnesium are also consistent with very little or no enhancement. On the other side, He abundance appears below the expected solar He/H ratio in the four stars with $T_{eff} > 11500$ K for which it has been measured.

The abundance anomalies in M79 are therefore likely to be due to the same diffusion processes that were invoked by Behr et al. (1999): radiative levitation of metals, and gravitational settling of helium, in the stable nonconvective atmospheres of the hotter, higher gravity stars, as hypothesized by Michaud et al. (1983). In addition, the jump in the u,$(u-y)$ diagram by Grundahl et al. (1999) for M79 is reported at $\log(T_{\rm eff})$=4.06 $\pm$ 0.01, in perfect agreement with the onset of the abundance anomalies observed here.

An underabundance of helium on the BHB was observed in several other previous instances (Baschek 1975; Heber 1987; Glaspey et al. 1989; among

others) and in fact appears to be typical for stars of this type. As pointed out in Chapter 2, Michaud, Vauclair, & Vauclair (1983), building on the original suggestion by Greenstein, Truran, & Cameron (1967), explain the underabundances as a result of the gravitational settling of helium, which can take place if the outer atmosphere of the star is sufficiently stable. Our current results confirm a distinct trend in [He/H] with T_{eff} and log g along the HB. Helium depletion is accompanied by photospheric enhancement of metals, since the same stable atmosphere that permits gravitational settling also permits the levitation of elements with large radiative cross sections. Elements which present sufficiently large cross-sections to the outgoing radiation field will experience radiative accelerations greater than gravity, and will diffuse upwards, enriching the photosphere. The gross behaviour of the diffusion models can be understood by considering the migration of chemical species in a stellar atmosphere (Gonzalez et al. 1995; Michaud, Vauclair, & Vauclair 1983 and Seaton 1997). The relative amount of levitation experienced by each element can be estimated by summing the predicted equivalent widths for every catalog line over the visible and near UV spectral range. The magnitudes of these net equivalent widths suggest that helium will experience only a weak levitation force, insufficient to oppose gravity, magnesium will be levitated by an intermediate amount, perhaps balanced by gravity, and iron will be strongly levitated. This is admittedly a crude approach to what we see in M79, and Behr et al. measurements in M13 and M15.

In general, our abundance measurements in M79 give very similar results to those obtained previously by Behr et al. (1999) in M13, which, on the other hand, has a very similar metallicity to that of M79. However, specially for the case of Fe, Ti and He, we obtain slightly higher abundances (about 0.5 dex higher) that what reported by Behr (2002) for M13. In the case of helium, most of our measurements are based on only a single line or two, and are therefore suspect. Nevertheless, the values for Fe and Ti are based on several separate spectral lines, in close agreement with each other. Therefore, differences between our M79 and the Behr (2002) values for M13 seem to exist. It worths to mention, however, that this disagreement can not be due to differences in the abundance analysis method. As pointed out in Chapter 4, our program, WIDTH3, has been tested by D. Fabbian with 4 M13 stars, previously observed by Behr et al. (1999), using their equivalent widths measurements and atmospheric parameters and yielding the same abundance results. This test rules out the possibility of abundance differences caused by the analysis technique. A possible origin for the abundance dissimilitude between the M79 and M13 measurements would be a systematic difference in the Behr (2002) temperature scale and ours. We have analyzed this possibility by comparing our (B-V),

T_{eff} relation with that of Behr (2002). They are in agreement for $T_{eff} <$ 11000 K, but they diverge non linearly at hotter temperatures. We feel quite confident of our temperature estimations, as they are based in two independent photometric measurements as explained in the previous chapter. However, there is no reason to state they are better of worse than the Behr (2002) ones for M13. On the other hand, the abundance differences in Fe and Ti would only be explained by decreasing our temperature estimations by about 4000 K, which seems completely unlikely. Moreover, correcting our helium abundances to the typical M13 values, would imply an opposite shift in temperature, increasing our estimations of about 2000 K.

Therefore, it is plausible that a real difference in the abundance values, for the hotter stars in M79 and M13, exists. A possible explanation could be rotational differences between their respective HB populations, which would be reflected directly in the diffusion effects. In fact, Michaud (2002, private communication), estimates that small differences in rotational velocity of about 2-3 km/s could generate sizable discrepancies in the radiative levitation and gravitational settling processes. Unfortunately, the accuracy of our rotational measurements in M79, with errors of the order of 4-5 km/s, do not allow us to explore this possibility.

5.3 Theoretical implications.

Along with similar previous studies, the present investigation demonstrates that HB stars in GCs rotate, and that they do so much faster than the Sun, in spite of braking mechanisms having been at work for $\sim$ one Hubble time. This suggests that either the stars are able to preserve part of their angular momentum all the way through very advanced evolutionary stages, or that they may re-acquire angular momentum, for example, as a result of tidal interactions in the high density environment offered by GCs.

It is quite possible that the envelope of stars is completely deprived of its angular momentum during the RGB phase, when at least half of this envelope is lost in a wind. Suffice indeed even a small magnetic field for efficiently transferring angular momentum from the whole convective envelope - which tends to rotate solid body - to the wind. However, the very small, degenerate core may still retain angular momentum, and on this hypothesis Mengel & Gross (1976) constructed evolutionary models with core rotation. In these models rotation has the effect of delaying the helium flash until the star reaches a slightly higher luminosity on the RGB. However small the effect, it would be sufficient to allow more mass to be lost by more rapidly rotating stars, offering an explanation for the origin of the mass dispersion along HB stars

(Renzini 1977). This scenario is in apparent conflict with the observations of stellar rotation among hot HB stars reported above, because one would expect the fast rotators to lose more mass than slow rotators, hence landing at higher temperatures on the HB. The opposite is instead observed: the hottest EHB stars are all slow rotators, while the fast rotators are found only below $\sim 11,000$K.

Another embarrassment comes from the mere fast rotation itself: what rotates is the stellar envelope, which should have lost all its angular momentum prior to the star beginning its HB phase. Sills & Pinsonneault (2000) proposed models for the angular momentum evolution in which no magnetic braking takes place, and stars retain some envelope rotation and a rapidly rotating core during the RGB phase. Once on the HB, angular momentum redistribution from the core to the envelope would spin up the envelope. However, in spite of being based on assumptions that favour angular momentum retention, these models fail to predict the high rotation observed below 11,500K, coupled with the low rotation observed at higher temperatures. So the puzzle remains.

Sills & Pinsonneault (2000) argue that diffusion of heavy elements in the hottest stars may prevent angular momentum transfer from the core, due to the build up of a gradient in mean molecular weight (μ). However, core and envelope have quite different μ anyway, hence diffusion does not look a viable alternative. Maybe core-envelope angular momentum transfer takes place after all, but in stars hotter than $\sim$ 11000K angular momentum is continuously removed via the radiatively accelerated wind typical of hot stars. An enhanced mass loss in higher metallicity atmospheres, as those of stars hotter than the jump where radiative levitation is at work, has been very recently calculated by Vink and Cassisi (2002), confirming this scenario. Radiative levitation and the "wind emission" effect is also the most likely explanation for the observed jump in the stellar gravities (Moehler et al. 2000, Vink and Cassisi 2002). As we have seen in the previous section, we have indeed detected radiative levitation among the stars hotter than the jump in M79.The fact that the change in the velocity distribution can be associated to the jump (instead of to the gap), as figure 5.3 clearly suggests, makes the entire scenario observationally consistent.

While also this remains a speculative solution to the puzzle of the hot slow rotators, still the cooler fast rotators seem to require a quite contrived angular momentum history. Angular momentum extraction from the core should be quite inefficient during the RGB (in order to maintain an angular momentum reservoir), and quite efficient during the HB (in order to promptly spin up the envelope). We also note that there is no apparent correlation between rotational velocity and luminosity *distance* from the ZAHB (cf. Fig. 5.1 and 5.2, right panels), as would result if the timescale of angular momentum diffusion were

comparable to the HB lifetime.

As already mentioned, besides all these complications the mere existence of fast rotators is not so obvious, given the ample opportunities to lose angular momentum along with mass during the RGB phase. Some recent papers (Soker 1998; Siess & Livio 1999; Soker & Harpaz 2000; Soker et al. 2001; Livio & Soker 2002) propose that fast HB rotators could have spun up by swallowing close planetary companions (Jovian planets or brown dwarfs) during the RGB phase. However, the major part of exoplanets found to date have host stars with significant higher metallicity than solar (Gonzalez & Laws 2000; Reid 2002). In addition, as pointed out in chapter 2, no planetary companions have been found in a very intense search for them in the GC 47 Tuc (Gilliland et al. 2000). However, Soker & Harpaz (2001) argue that, as 47 Tuc contains only a few blue HB stars (Rich et al. 1997), and planets should be related to the presence of blue tails, no stars in this globular cluster are expected to have massive and close planets around them

Quite more attractive is the hypothesis of an envelope spin up as a result of close tidal encounters of RGB stars with main sequence dwarfs. This scenario is circumstantially supported by the noted correlation of the presence of an extended BT with the cluster density (Fusi Pecci et al. 1993), with very extended BTs being found almost exclusively in the densest GCs. So, tidal encounters may account for both enhanced mass loss (e.g. stripping) responsible for the blue extension of the HB, and for the enhanced rotational velocities of some HB stars. We will come back latter to this hypothesis in Chapter 6, where the photometric results of this thesis are discussed.

Star	α_{2000}	δ_{2000}	u	(u-y)	**log (T_{eff})**	v_{rad} **(km/s)**	v**sin**i **(km/s)**
m79-489	05:24:10.6	-24:32:46	17.861	0.516	4.184	+196.1 ± 0.9	$\leq$ 10
m79-535	05:24:16.6	-24:31:59	18.075	0.607	4.158	+199.2 ± 0.8	13 ± 3
m79-555	05:24:15.8	-24:30:36	18.183	0.631	4.151	+201.5 ± 0.9	8 ± 5
m79-434	05:24:16.6	-24:31:37	17.782	0.859	4.095	+207.3 ± 1.0	$\leq$ 6
m79-469	05:24:08.2	-24:32:13	18.004	0.897	4.086	+202.6 ± 0.8	$\leq$ 6
m79-392	05:24:13.4	-24:30:25	17.684	0.939	4.076	+204.3 ± 0.8	6 ± 5
m79-363	05:24:13.4	-24:31:26	17.879	0.982	4.065	+198.7 ± 0.8	10 ± 4
m79-389	05:24:16.3	-24:31:30	17.781	1.075	4.043	+195.8 ± 0.9	$\leq$ 10
m79-354	05:24:07.9	-24:32:17	17.929	1.294	3.991	+209.0 ± 1.3	5 ± 5
m79-366	05:24:15.4	-24:31:26	17.987	1.378	3.971	+205.1 ± 1.1	7 ± 3
m79-297	05:24:17.2	-24:30:18	17.852	1.394	3.967	+202.2 ± 1.7	20 ± 3
m79-327	05:24:14.0	-24:29:54	18.000	1.574	3.924	+204.2 ± 1.6	24 ± 4
m79-281	05:24:27.2	-24:29:16	17.958	1.609	3.916	+213.1 ± 1.8	$\leq$ 10
m79-298	05:24:21.6	-24:28:59	17.967	1.615	3.914	+214.2 ± 2.2	26 ± 4
m79-289	05:24:17.5	-24:31:23	17.957	1.635	3.910	+205.5 ± 1.8	22 ± 2
m79-295	05:24:02.0	-24:31:35	18.016	1.648	3.906	+208.2 ± 1.1	26 ± 2
m79-275	05:24:17.9	-24:30:40	17.970	1.723	3.889	+206.5 ± 2.9	27 ± 6
m79-243	05:24:19.6	-24:32:26	17.959	1.725	3.888	+207.1 ± 0.6	16 ± 3
m79-294	05:24:18.9	-24:31:49	17.999	1.754	3.881	+208.9 ± 1.5	20 ± 3
m79-209	05:24:16.2	-24:32:16	17.852	1.797	3.871	+199.1 ± 0.4	$\leq$ 6

Star	α_{2000}	δ_{2000}	U	(U-B)	**log (T_{eff})**	v_{rad} **(km/s)**	v**sin**i **(km/s)**
n2808-7596	9:11:24.9	-64:52:46	17.714	-0.785	4.453	+101.6 ± 5.4	$\leq$ 13
n2808-9432	9:12:23.8	-64:52:08	18.219	-0.666	4.363	+104.5 ± 3.5	$\leq$ 12
n2808-11222	9:12:53.6	-64:51:05	18.370	-0.591	4.314	+105.7 ± 2.6	$\leq$ 12
n2808-9655	9:11:59.8	-64:47:45	18.287	-0.532	4.277	+106.3 ± 1.7	7 ± 7
n2808-6427	9:11:41.6	-64:49:16	17.574	-0.371	4.185	+102.7 ± 1.4	6 ± 6
n2808-3159	9:12:12.2	-64:58:23	16.967	-0.157	4.081	+102.4 ± 1.2	$\leq$ 10
n2808-4512	9:11:18.7	-64:57:14	17.136	-0.149	4.077	+101.1 ± 1.0	8 ± 5
n2808-3715	9:12:25.9	-64:55:13	17.003	-0.081	4.049	+101.3 ± 1.2	$\leq$ 9
n2808-4991	9:11:24.2	-64:49:59	17.294	-0.057	4.039	+102.9 ± 1.2	$\leq$ 10
n2808-3721	9:11:58.1	-64:57:09	17.092	0.004	4.016	+101.6 ± 1.2	$\leq$ 12
n2808-3435	9:12:18.3	-64:49:37	16.999	0.026	4.008	+114.5 ± 1.4	11 ± 5
n2808-3841	9:11:49.8	-64:57:30	17.043	0.044	4.002	+96.4 ± 1.2	13 ± 4
n2808-3949	9:12:17.2	-64:46:41	17.077	0.068	3.993	+103.3 ± 1.3	8 ± 6
n2808-2333	9:12:23.4	-64:52:00	16.804	0.174	3.957	+109.4 ± 0.6	5 ± 5
n2808-2445	9:11:42.3	-64:52:51	16.853	0.290	3.872	+85.7 ± 0.4	5 ± 5
n2808-2909	9:12:03.9	-64:49:27	16.904	0.150	3.965	+105.6 ± 1.2	10 ± 5

Star	α_{2000}	δ_{2000}	*F555W*	(*F439W-F555W*)	**log (T_{eff})**	v_{rad} (km/s)	v**sin**i (km/s)
m80-509	16:17:05.2	-22:58:47	16.622	0.216	3.946	+7.9 ± 0.5	7 ± 4
m80-820	16:17:08.2	-22:58:30	16.684	0.209	3.953	+8.6 ± 1.1	8 ± 6
m80-1400	16:17:08.5	-22:59:00	18.141	0.143	4.047	+5.7 ± 0.7	$\leq$ 10
m80-2044	16:17:05.8	-22:57:54	16.998	0.141	4.053	+23.5 ± 0.5	8 ± 4
m80-2242	16:17:07.2	-22:57:56	18.740	0.014	4.385	+26.6 ± 1.2	7 ± 6
m80-938	16:17:08.2	-22:58:30	16.886	-0.150	4.099	+17.8 ± 0.8	$\leq$ 10
			V	(*V-I*)			
m80-107	16:17:02.5	-23:02:25	16.88	0.221	4.049	+15.9 ± 0.9	6 ± 6
m80-109	16:17:00.1	-23:00:44	16.86	0.232	4.034	+14.1 ± 0.6	$\leq$ 7
m80-83	16:17:17.9	-22:58:27	16.57	0.270	3.988	+10.0 ± 1.1	10 ± 5
m80-1149	16:17:03.3	-23:00:17	18.15	0.095	4.249	+18.3 ± 1.4	9 ± 6
m80-454	16:17:11.8	-22:58:05	18.70	0.034	4.370	-0.7 ± 1.0	$\leq$ 9

Star	α_{2000}	δ_{2000}	*V*	(*B-V*)	**log (T_{eff})**	v_{rad} (km/s)	v**sin**i (km/s)
m15-1813	21:30:03.8	12:10:26	16.04	0.124	3.930	-98.7 ± 1.0	10 ± 5
m15-5516	21:30:01.0	12:11:18	16.28	0.076	3.952	-99.0 ± 1.2	12 ± 4
m15-6143	21:29:59.1	12:08:37	16.21	0.084	3.954	-101.7 ± 0.8	$\leq$ 10
m15-2700	21:30:00.1	12:10:34	16.66	-0.031	4.131	-148.0 ± 0.9	7 ± 6
m15-2917	21:29:57.9	12:11:08	15.98	0.119	3.926	-109.7 ± 0.7	7 ± 5
m15-3333	21:30:04.0	12:09:49	16.17	0.127	3.933	-91.9 ± 1.6	12 ± 5
m15-4047	21:29:59.0	12:11:10	16.15	0.110	3.935	-93.1 ± 1.5	$\leq$ 10
m15-4536	21:30:00.0	12:11:05	17.08	0.023	4.023	-101.9 ± 1.2	$\leq$ 9
m15-5168	21:30:00.0	12:08:45	16.88	-0.022	4.108	-102.9 ± 0.9	6 ± 6
m15-768	21:30:03.8	12:10:46	16.94	-0.011	4.086	-102.6 ± 0.9	$\leq$ 8
m15-817	21:30:02.8	12:10:30	17.04	-0.010	4.078	-110.8 ± 1.3	$\leq$ 9
m15-b130	21:29:54.8	12:12:15	15.96	0.150	3.954	-113.9 ± 0.6	5 ± 3
m15-b218	21:29:45.6	12:11:25	15.99	0.160	3.908	-94.6 ± 0.5	13 ± 3
			V	(*V-I*)			
m15-1048	21:30:03.3	12:12:02	16.79	0.027	4.058	-101.2 ± 0.6	11 ± 4
m15-699	21:29:47.0	12:09:51	16.63	0.064	4.035	-103.2 ± 2.7	23 ± 4
m15-788	21:29:49.5	12:12:37	15.94	0.239	3.904	-103.0 ± 0.7	7 ± 5

TABLE 5.1— Positions, photometric information, effective temperature and velocity measurements of target stars.

star	log He	log Mg	log Si	log P	log Ca	log Ti	log Cr	log Mn	log Fe	Y[/H]
m79-209	...	6.5±0.2	6.3±0.2	...	5.3±0.2	3.9±0.2	4.5±0.2	6.1±0.2	6.1±0.2	...
m79-281	...	6.9±0.3	7.0±0.4	...	...	4.2±0.4	5.0±0.3	6.5±0.3	6.3±0.3	...
m79-354	11.5±0.6	6.2±0.6	7.4±0.6	...	3.2±0.6	5.0±0.4	...	...	7.1±0.6	...
m79-389	...	7.9±0.3	7.2±0.3	7.4±0.3	...	5.1±0.4	...	7.7±0.5	7.9±0.3	...
m79-363	...	7.3±0.5	...	...	...	5.0±0.3	...	...	7.7±0.2	...
m79-392	10.6±0.4	5.9±0.2	5.6±0.2	...	3.9±0.2	4.7±0.2	4.9±0.3	6.4±0.2	7.8±0.2	3.8±0.4
m79-434	...	8.2±0.2	6.9±0.5	...	5.7±0.5	5.5±0.4	6.1±0.5	...	7.9±0.5	...
m79-469	9.9±0.3	7.1±0.3	6.7±0.3	...	5.7±0.1	5.7±0.4	5.8±0.5	8.4±0.3	8.0±0.3	...
m79-535	10.5±0.3	7.7±0.3	7.2±0.1	...	...	5.1±0.3	...	...	8.0±0.3	...
m79-489	10.6±0.3	7.3±0.2	6.5±0.3	6.8±0.3	...	5.9±0.3	7.1±0.3	8.1±0.3	7.7±0.3	...

TABLE 5.2— Summary of chemical abundance log ϵ for program stars.

star	[He/H]	[Mg/H]	[Si/H]	[P/H]	[Ca/H]	[Ti/H]	[Cr/H]	[Mn/H]	[Fe/H]	Y[/H]
m79-209	...	-1.1±0.2	-1.3±0.2	...	-1.0±0.2	-1.2±0.2	-1.1±0.2	+0.7±0.2	-1.4±0.2	...
m79-281	...	-0.5±0.3	-0.5±0.4	...	...	-0.8±0.4	-0.7±0.3	+1.1±0.3	-1.2±0.3	...
m79-354	+0.6±0.6	-1.4±0.6	-0.2±0.6	...	-3.1±0.6	-0.1±0.4	...	...	-0.4±0.6	...
m79-389	...	+0.3±0.3	-0.3±0.3	+1.9±0.3	...	+0.1±0.4	...	+2.3±0.5	+0.4±0.3	...
m79-363	...	-0.2±0.5	...	...	...	-0.1±0.3	...	...	+0.2±0.2	...
m79-392	-0.3±0.4	-1.6±0.2	-1.9±0.2	...	-2.4±0.2	-0.3±0.2	-0.8±0.3	+1.0±0.2	+0.3±0.2	+1.5±0.4
m79-434	...	+0.6±0.2	-0.6±0.5	...	-0.6±0.5	+0.5±0.4	+0.4±0.5	...	+0.4±0.5	...
m79-469	-1.0±0.3	-0.5±0.3	-0.8±0.3	...	-0.6±0.1	+0.8±0.4	+0.1±0.5	+3.0±0.3	+0.5±0.3	...
m79-535	-0.5±0.3	+0.1±0.3	-0.4±0.1	...	...	+0.1±0.3	...	...	+0.5±0.3	...
m79-489	-0.3±0.3	-0.3±0.2	-1.0±0.3	+1.3±0.3	...	+0.9±0.3	+1.4±0.3	+4.5±0.3	+0.2±0.3	...

TABLE 5.3— Summary of chemical abundance results, relative to solar, for program stars.

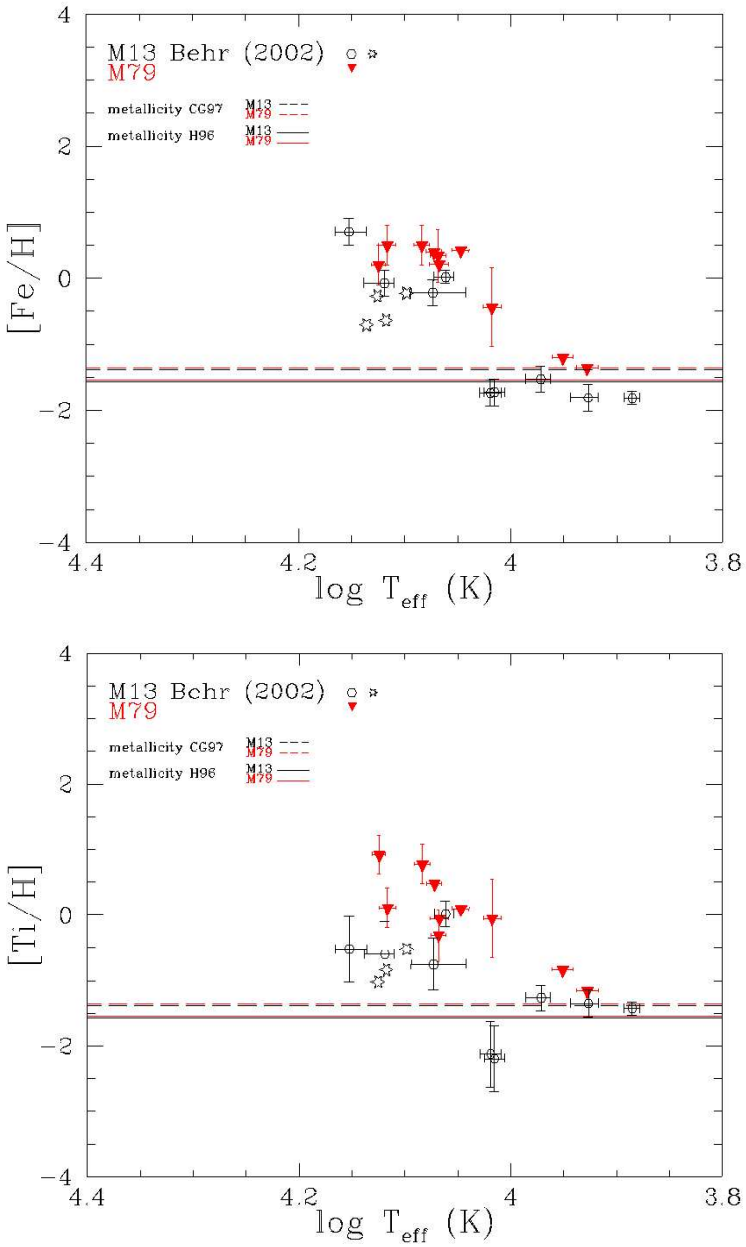


FIGURE 5.5— Abundance values for iron and titanium as a function of T_{eff} as log offsets from the solar abundances. The abundance values from Behr et al. (2002) for M13 are also plotted for comparison as black circles and black stars. The last ones are data with an error in the effective temperature higher than 2000 K. The horizontal lines represent the expected value of [metal/H] from solar for M79 (in red) and M13 (in black), both in the Carretta & Gratton (1997) scale: dashed lines at -1.37 and -1.39, respectively; and in the Harris (1996) scale: solid lines at -1.54 and -1.57.

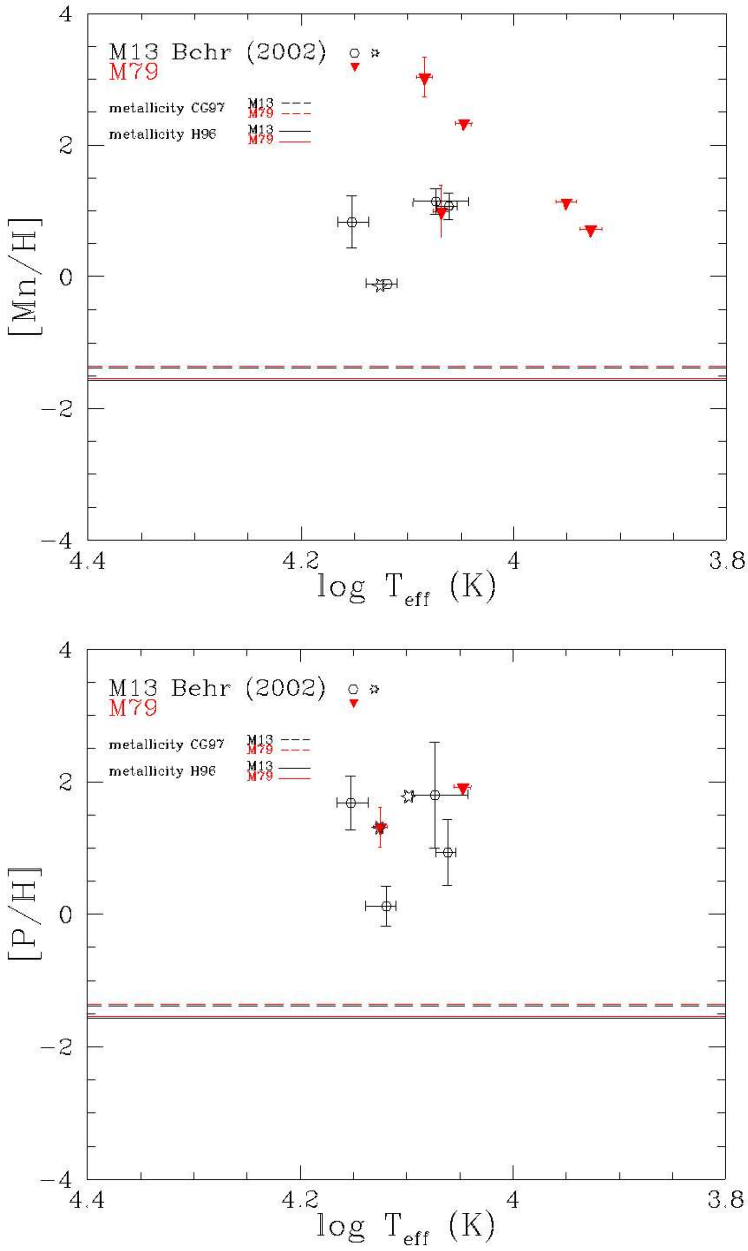


FIGURE 5.6— Same as Figure 5.5 but for manganese and phosphorus.

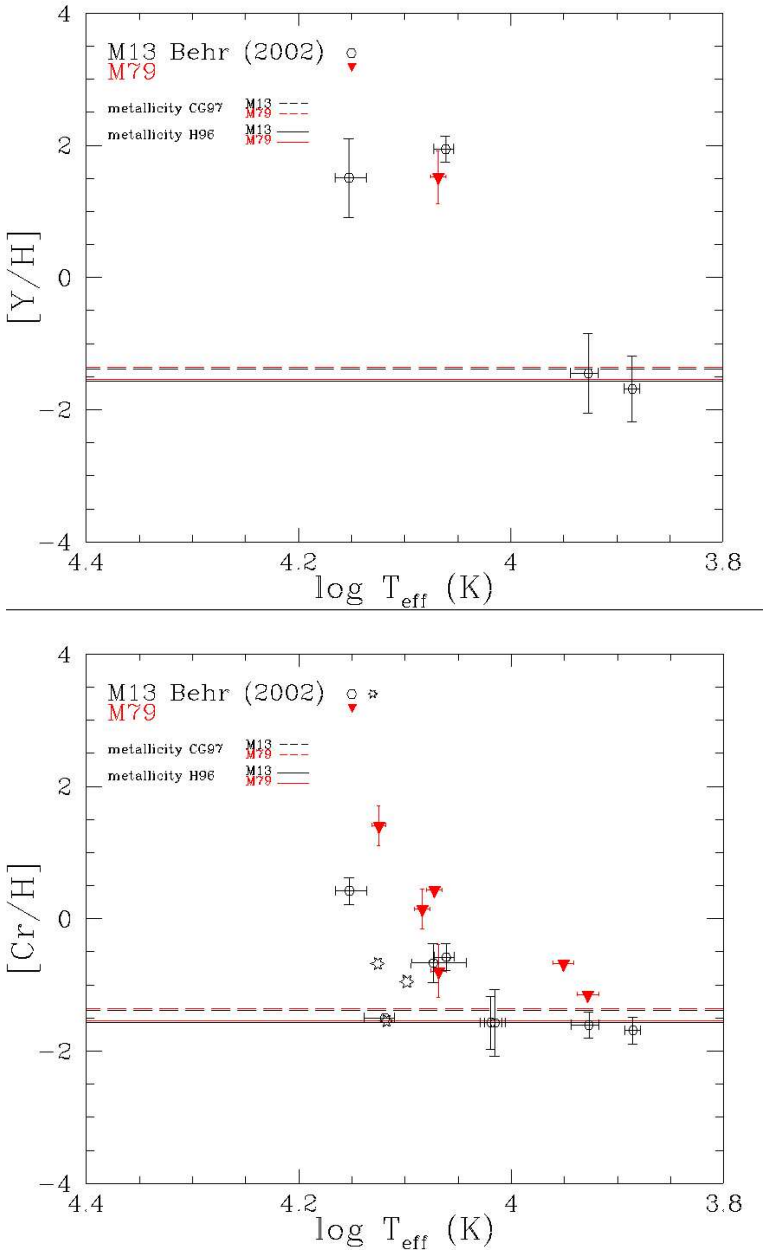


FIGURE 5.7— Yttrium and chromium abundances.

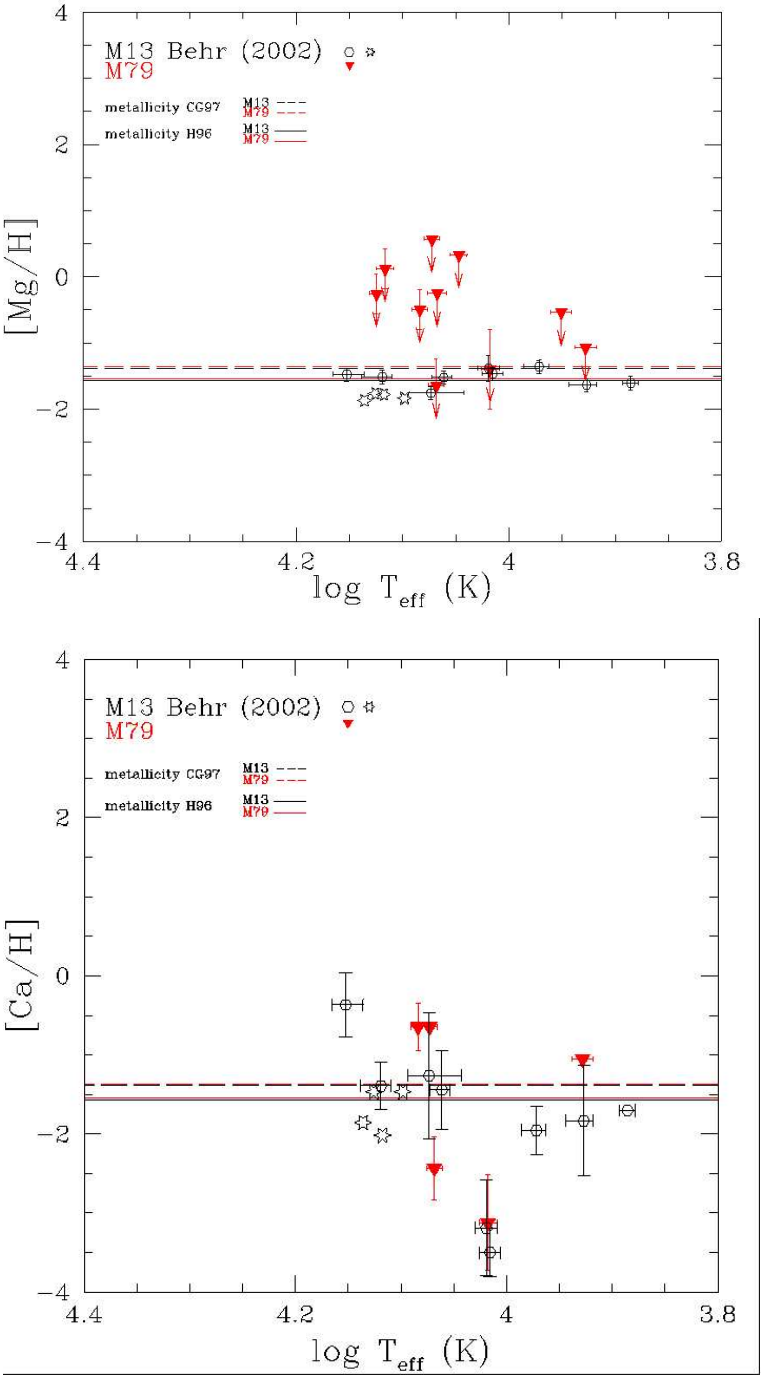


FIGURE 5.8— Magnesium and calcium abundances.

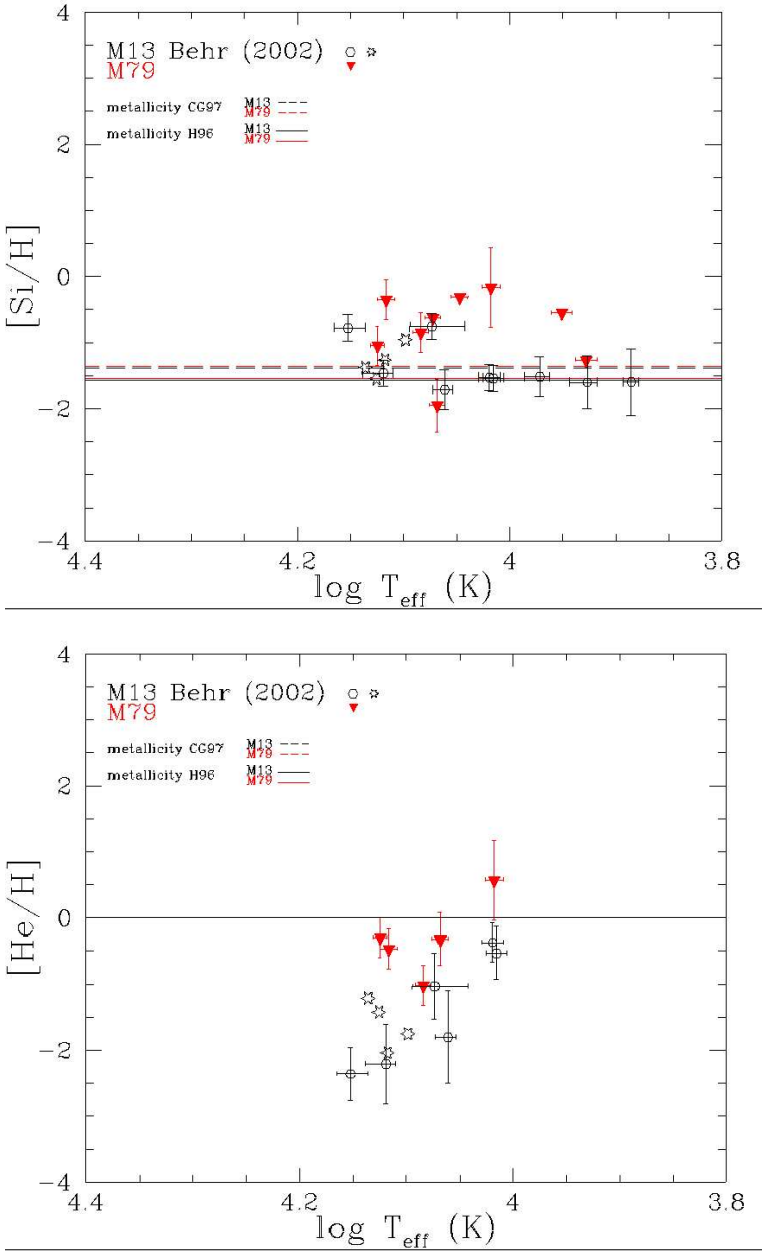


FIGURE 5.9— Silicon and helium abundances.

Part III

Photometric Properties of Hot Horizontal Branch Stars

6

HST data: searching for the second parameter.

THE second part of this thesis analyzes the photometric properties of hot HB stars in Galactic GCs and how these characteristics change from cluster to cluster. To this purpose, I have been given the opportunity to participate in a *Hubble Space Telescope* snapshot program aimed at mapping the cores of all GCs with (m-M)$_B$ < 18.0, using the Wide Field/ Planetary Camera 2 (WFPC2) of HST. Due to the severe stellar crowding, the excellent resolving power of HST is crucial for the photometrical studies of the globular cluster central regions, where accurate ground based observations are precluded. Moreover, for GCs near the Galactic center, only the central regions are sufficiently uncontaminated by field stars to allow a good study of the colour-magnitude diagram. The complete database, a total of 74 GCs (53 snapshot plus 21 archive data), measured and reduced in an uniform way, represents an exceptional opportunity, from the statistical point of view, to investigate how HB morphology depends on globular cluster properties: metallicity, concentration, distance to the Galactic center, total mass, etc. In other words, to search for the so called HB second parameter(s). In our investigation, we will concentrate on the properties of the HB blue tails, with the aim of unveiling the origin the hot horizontal branch stars.

6.1 The database.

The data set presented here has already been shown to be extremely valuable in attacking a number of still-open topics on evolved stars in GCs. In particular, Piotto et al. (1999a) investigated the problem of BT stellar distribution

(in a subset of the present day data); Raimondo et al. (2002) analyzed the properties of red HB in metal-rich clusters; Zoccali et al. (1999) and Bono et al. (2001) throughly discussed the RGB bump, and compared the predicted position and dimension of this feature with the observed ones; Zoccali et al. (2000) used the star counts on the HB and on the RGB to gather information on the helium content and on the dependence of the helium content on the cluster metallicity; Zoccali & Piotto (2000) made the most extensive comparison so far available between the model evolutionary times away from the main sequence and the actual star counts on the subgiant branch (SGB) and RGB; Cassisi et al. (2001) compared the observed and theoretical properties of the asymptotic giant branches; Piotto et al. (2000) used the CMDs in our database for the study of the Galactic GC relative ages, and, finally, in Piotto et al. (1999b), started to investigate the GC blue straggler (BS) population, and have shown how the BS CMD and luminosity function can differ in clusters with rather different morphologies. The HST snapshot survey has led to the unexpected discovery of hot horizontal branch blue tails in some metal rich GCs NGC6388, NGC6441 (Rich et al. 1997), and in NGC2808 (Sosin et al. 1997) and NGC 6273 (Piotto et al. 1999b).

We have presented the complete database in a recent paper (Piotto et al. 2002). It has to be mentioned that this HST snapshot photometry not only provides a unique database for the study of BTs, but has also played an important role in the target selection for the spectroscopic analysis of hot HB stars described in the previous chapters.

Figure 6.1 shows an image of the center of NGC 6441, taken in the F555W band with the Planetary Camera of HST. The squares are centered on the BT stars.

6.2 Observations and pre-reduction of the images

All the photometric data for the 74 GCs come from HST/WFPC2 observations in the F439W and F555W bands, the WFPC2 equivalents of the B and V filters, which are suited for a generic survey and constitute the best choice to identify new anomalous HBs. In all cases, the PC camera was centered on the cluster center. Tables 6.1 and 6.2 list the observed clusters (Col. 1); the origin of the observations (Col. 2), and the exposure times in F555W (Col. 3) and F439W (Col. 4) bands. Tables 6.3 and 6.4 give a few relevant parameters (from the Harris, 1996 compilation). Fig. 6.2 shows the spatial distribution of the target clusters within the Galaxy.

After the snapshot observations (or, for 10 archive clusters, after the public release date), the images were retrieved via ftp from the HST archive in

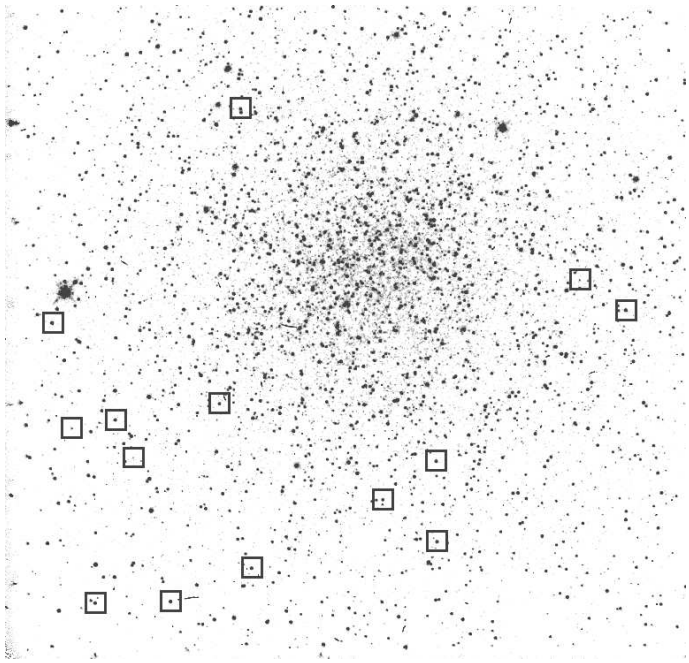


FIGURE 6.1— The central 30×30 arcsec^2 of the GC NGC 6441. The 1×1 arcsec^2 squares are centered on the target HB stars.

Cluster	Program ID	Exp. Time F555W [s]	Exp. Time F439W [s]
NGC 104	GO6095	1, 7	7, 2x(50)
NGC 362	GO6095	3, 18	18, 2x(160)
NGC 1261*	GO7470	10, 40	40, 2x(160)
NGC 1851	GO6095	6, 40	40, 2x(160)
NGC 1904	GO6095	7, 40	40, 2x(160)
NGC 2419*	archive	10, 2x(100)	2x(260)
NGC 2808	GO6095	7, 50	50, 2x(230)
NGC 3201*	GO8118	3, 2x(30)	40, 2x(100)
NGC 4147*	GO7470	10, 40	40, 2x(160)
NGC 4372	GO8118	3, 2x(30)	40, 2x(100)
NGC 4590*	GO7470	5, 40	40, 2x(100)
NGC 4833	GO8118	3, 2x(30)	40, 2x(100)
NGC 5024	GO8118	5, 40	40, 2x(160)
NGC 5634	GO7470	10, 40	40, 2x(160)
NGC 5694	archive	10, 4x(60)	120, 3x(500)
IC 4499*	GO8723	10, 40	40, 2x(160)
NGC 5824	archive	2x(10), 5x(60)	120, 3x(500)
NGC 5904	GO8118	3, 2x(30)	40, 2x(100)
NGC 5927	GO6095	10, 50	50, 2x(160)
NGC 5946*	GO7470	10, 40	40, 2x(160)
NGC 5986*	GO7470	10, 40 ec	40, 2x(160)
NGC 6093*	archive	2x(2), 4x(23)	2x(30)
NGC 6139	GO7470	10, 40	40, 2x(160)
NGC 6171*	GO7470	5, 40	40, 2x(100)
NGC 6205*	archive	4x(1), 4x(8)	2x(14)
NGC 6229	GO8118	10, 40	40, 2x(160)
NGC 6218	GO8118	3, 2x(30)	40, 2x(100)
NGC 6235	GO7470	10, 40	40, 2x(160)
NGC 6256*	GO7470	10, 40	40, 2x(160)
NGC 6266	GO8118	3, 2x(30)	40, 2x(100)
NGC 6273	GO7470	10, 40	40, 2x(160)
NGC 6284*	archive	4, 4x(40)	30, 6x(160)
NGC 6287*	archive	2x(5), 3x(50) 3x(1000)	60, 230
NGC 6293	archive	2, 5x(40)	20, 6x(160)
NGC 6304*	GO7470	10, 40	40, 2x(160)
NGC 6316*	GO7470	10, 40	40, 2x(160)
NGC 6325*	GO7470	10, 40	40, 2x(160)

TABLE 6.1— Observation log. Asterisks indicate clusters reduced by using Stetsons PSFs.

Cluster	Program ID	Exp. Time F555W [s]	Exp. Time F439W [s]
NGC 6342	GO7470	10, 40	40, 2x(160)
NGC 6356	GO7470	10, 40	40, 2x(160)
NGC 6355*	GO7470	10, 40	40, 2x(160)
IC 1257*	GO8723	30, 100	160, 2x(300)
NGC 6362*	GO7470	5, 40	40, 2x(100)
NGC 6380	GO7470	10, 40	40, 2x(160)
NGC 6388	GO6095	12, 50	50, 2x(160)
NGC 6402	GO8118	7, 40	40, 2x(160)
NGC 6401	GO7470	10, 40	40, 2x(160)
NGC 6397*	archive	1, 8, 6x(40)	2x(10), 2x(80) 16x(400), 4x(500)
NGC 6440*	GO8723	10, 40	40, 2x(160)
NGC 6441	GO6095	14, 50	50, 2x(160)
NGC 6453	GO8118	10, 40	40, 2x(160)
NGC 6517*	GO8723	10, 40	40, 2x(160)
NGC 6522	GO6095	10, 50	50, 2x(160)
NGC 6539	GO8118	10, 40	40, 2x(160)
NGC 6540	GO8118	5, 40	40, 2x(160)
NGC 6544	GO8118	3, 2x(30)	40, 2x(100)
NGC 6569	GO8118	5, 40	40, 2x(160)
NGC 6584	GO8118	5, 2x(30)	40, 2x(100)
NGC 6624	archive	4x(10)	2x(50)
NGC 6638	GO8118	5, 40	40, 2x(160)
NGC 6637	GO8118	3, 2x(30)	40, 2x(100)
NGC 6642	GO8118	3, 40	40, 2x(160)
NGC 6652*	GO6095	10, 50	50, 2x(160)
NGC 6681*	GO8723	3, 2x(30)	40, 2x(100)
NGC 6712*	archive	60	160
NGC 6717	GO8118	3, 2x(30)	40, 2x(100)
NGC 6723	GO8118	3, 2x(30)	40, 2x(100)
NGC 6760*	GO8723	7, 40	40, 2x(160)
NGC 6838	GO8118	3, 2x(30)	40, 2x(100)
NGC 6864*	GO8723	7, 40	40, 2x(160)
NGC 6934*	GO7470	10, 40	40, 2x(160)
NGC 6981	GO7470	10, 40	40, 2x(160)
NGC 7078	archive	4x(8)	2x(40)
NGC 7089	GO8118	3, 2x(30)	40, 2x(100)
NGC 7099	archive	4x(4)	2x(40)

TABLE 6.2— Observation log (cont.).

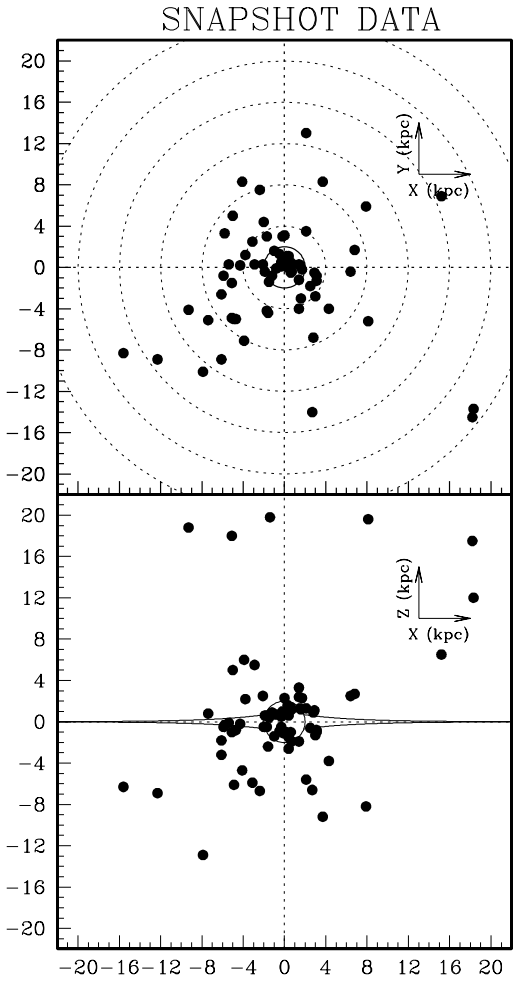


FIGURE 6.2— Spatial distribution of the target clusters within the Galaxy.

Baltimore, and they were furtherly processed following in part the recipe in Silbermann et al. (1996). As in Silbermann et al., the vignetted pixels, and bad pixels and columns, were masked out using a vignetting frame created by P. B. Stetson, together with the appropriate data-quality file for each frame. However, we did *not* correct for the pixel area map, since this correction is included in the calibration process described below. Finally the single-chip frames were extracted from the 4-chip-stack files, and analyzed separately. Frames obtained both at gain = $7e^-$/ADU and at $15e^-$/ADU were available, so care was taken to adjust the various parameters to the applicable gain value for each image.

6.3 Reduction procedures.

6.3.1 Instrumental magnitudes

The photometric reduction was carried out using the DAOPHOT II/ALLFRAME package (Stetson, 1987; Stetson, 1994). Preliminary photometry was carried out in order to construct an approximate list of stars for each single frame. This list was used to match the different frames accurately. With the correct coordinate transformations among the frames, we obtained a single image, combining all the frames, regardless of the filter. In this way we could eliminate all the cosmic rays and obtain the highest signal/noise image for star finding. We ran the DAOPHOT/FIND routine on the stacked image and performed PSF-fitting photometry in order to obtain the deepest list of stellar objects free from spurious detections. The subtracted image was searched again for objects missed in the first pass, and the new list was appended to the existing one. Finally, the entire star list was given as input to ALLFRAME, for the simultaneous PSF-fitting photometry of all the individual frames. In some cases we could not construct a PSF from our images, since there were not enough sufficiently isolated stars in any of the four chips. In those instances, the PSFs used were the high-S/N PSFs extracted by P. B. Stetson (private communication) from a large set of uncrowded and unsaturated WFPC2 images. The clusters for which Stetson PSFs have been used are marked with an asterisk in Tables 6.1,6.2. For each of the WFPC2 chips, the (typically two) F555W and (typically three) F439W magnitude lists were combined to create a raw colour-magnitude diagram (CMD). First a catalog of mean magnitudes was created for each of the two filters, and then they were combined to obtain the F439W−F555W colours. In this process, we used the programs DAOMATCH/DAOMASTER (kindly provided by P. B. Stetson), which yield magnitudes in the instrumental photometric system of the two F555W and F439W frames that were chosen as references.

ID	Name	R_{GC}	$E(B-V)$	$(m-M)_V$	M_{Vt}	[Fe/H]	c	r_t	$log(t_h)$	$log(\rho_0)$
NGC 104	47 Tuc	7.4	0.04	13.37	−9.42	−0.76	2.03	47.25	9.48	4.77
NGC 362		9.3	0.05	14.80	−8.40	−1.16	1.94c:	16.11	8.92	4.70
NGC 1261		18.2	0.01	16.10	−7.81	−1.35	1.27	7.28	9.20	2.96
NGC 1851		16.7	0.02	15.47	−8.33	−1.22	2.32	11.70	8.85	5.32
NGC 1904	M 79	18.8	0.01	15.59	−7.86	−1.57	1.72	8.34	9.10	4.00
NGC 2419		91.5	0.11	19.97	−9.58	−2.12	1.40	8.74	10.55	1.54
NGC 2808		11.0	0.23	15.56	−9.36	−1.15	1.77	15.55	9.11	4.61
NGC 3201		9.0	0.21	14.24	−7.49	−1.58	1.30	28.45	9.23	2.69
NGC 4147		21.3	0.02	16.48	−6.16	−1.83	1.80	6.31	8.67	3.48
NGC 4372		7.1	0.39	15.01	−7.77	−2.09	1.30	34.82	9.59	2.09
NGC 4590	M 68	10.1	0.05	15.19	−7.35	−2.06	1.64	30.34	9.29	2.54
NGC 4833		6.9	0.33	14.92	−8.01	−1.79	1.25	17.85	9.34	3.06
NGC 5024	M 53	18.8	0.02	16.38	−8.77	−1.99	1.78	21.75	9.69	3.04
NGC 5634		21.9	0.05	17.22	−7.75	−1.82	1.60	8.36	9.28	3.12
NGC 5694		29.1	0.09	17.98	−7.81	−1.86	1.84	4.29	9.15	4.03
IC 4499		15.7	0.23	17.09	−7.33	−1.60	1.11	12.35	9.66	1.49
NGC 5824		25.8	0.13	17.93	−8.84	−1.85	2.45	15.50	9.33	4.66
NGC 5904	M 5	6.2	0.03	14.46	−8.81	−1.29	1.83	28.40	9.53	3.91
NGC 5927		4.5	0.45	15.81	−7.80	−0.37	1.60	16.68	8.98	3.87
NGC 5946		7.4	0.54	17.21	−7.60	−1.38	2.50c	24.03	8.95	4.50
NGC 5986		4.8	0.27	15.94	−8.42	−1.58	1.22	10.52	9.23	3.30
NGC 6093	M 80	3.8	0.18	15.56	−8.23	−1.75	1.95	13.28	8.86	4.76
NGC 6139		3.6	0.75	17.35	−8.36	−1.68	1.80	8.52	9.04	4.66
NGC 6171	M 107	3.3	0.33	15.06	−7.13	−1.04	1.51	17.44	9.31	3.13
NGC 6205	M 13	8.7	0.02	14.48	−8.70	−1.54	1.51	25.18	9.30	3.33
NGC 6229		30.0	0.01	17.46	−8.07	−1.43	1.61	5.38	9.19	3.40
NGC 6218	M 12	4.5	0.19	14.02	−7.32	−1.48	1.39	17.60	9.02	3.23
NGC 6235		2.9	0.36	16.11	−6.14	−1.40	1.33	7.61	8.67	3.11
NGC 6256		2.1	1.03	17.31	−6.02	−0.70	2.50c	7.59	8.40	5.70
NGC 6266	M 62	1.7	0.47	15.64	−9.19	−1.29	1.70c:	8.97	9.19	5.14
NGC 6273	M 19	1.6	0.37	15.85	−9.08	−1.68	1.53	14.50	9.34	3.96
NGC 6284		6.9	0.28	16.70	−7.87	−1.32	2.50c	23.08	9.16	4.44
NGC 6287		1.7	0.60	16.51	−7.16	−2.05	1.60	10.51	8.66	3.85
NGC 6293		1.4	0.41	15.99	−7.77	−1.92	2.50c	14.23	8.91	5.22
NGC 6304		2.1	0.52	15.54	−7.32	−0.59	1.80	13.25	8.89	4.39
NGC 6316		3.2	0.51	16.78	−8.35	−0.55	1.55	5.93	9.00	4.21
NGC 6325		2.0	0.89	17.68	−7.35	−1.17	2.50c	9.49	8.92	5.40
NGC 6342		1.7	0.46	16.10	−6.44	−0.65	2.50c	14.86	8.66	4.77
NGC 6356		7.6	0.28	16.77	−8.52	−0.50	1.54	7.97	9.26	3.76
NGC 6355		1.0	0.75	16.62	−7.48	−1.50	2.50c	15.18	8.71	4.95
IC 1257		17.9	0.73	19.25	−6.15	−1.70				
NGC 6362		5.3	0.08	14.79	−7.06	−0.95	1.10	16.67	9.31	2.22
NGC 6380	Ton 1	3.2	1.17	18.77	−7.46	−0.50	1.55c:	12.06	8.87	3.70
NGC 6388		4.4	0.40	16.54	−9.82	−0.60	1.70	6.21	9.24	5.31
NGC 6402	M 14	3.9	0.60	16.61	−9.02	−1.39	1.60	33.24	9.36	3.30
NGC 6401		0.8	0.85	17.07	−7.62	−1.12	1.69	12.10	9.29	4.10
NGC 6397		6.0	0.18	12.36	−6.63	−1.95	2.50c	15.81	8.46	5.68
NGC 6440		1.3	1.07	17.95	−8.75	−0.34	1.70	6.31	8.76	5.28
NGC 6441		3.5	0.44	16.62	−9.47	−0.53	1.85	8.00	9.13	5.23
NGC 6453		3.3	0.61	17.13	−7.05	−1.53	2.50c	21.50	8.36	4.72
NGC 6517		4.3	1.08	18.51	−8.28	−1.37	1.82	4.10	8.88	5.20
NGC 6522		0.6	0.48	15.94	−7.67	−1.44	2.50c	16.44	8.90	5.31
NGC 6539		3.1	0.97	17.63	−8.30	−0.66	1.60	21.46	9.37	3.62
NGC 6540	Djorg 3	4.4	0.60	14.68	−5.38	−1.20	2.50c	9.49	7.08	5.92
NGC 6544		5.4	0.73	14.33	−6.56	−1.56	1.63c:	2.05	8.35	5.75
NGC 6569		1.2	0.56	16.43	−7.88	−0.86	1.27	6.95	9.17	3.76

TABLE 6.3— Main Parameters of the Clusters: Cols. 1 and 2 give the cluster identification number and other commonly used cluster name, Cols. 3 and 4 the Galactic longitude and latitude (degrees), Col. 5 gives the distance from the Galactic center (kpc), assuming $R_0 = 8.0$ kpc, Col. 6 the foreground reddening, Col. 7 the apparent visual distance modulus, Col. 8 the absolute visual magnitude, Col. 9 the metallicity [Fe/H], Col. 10 the central concentration ($c = \log(r_t/r_c)$, a "c" denotes a core-collapsed cluster), Col. 11 the logarithm of core relaxation time (log (years)), Col. 12 the logarithm of relaxation time at the half-mass radius (log (years)), Col. 13 the logarithm of central luminosity density ($L_\odot \mathrm{pc}^{-3}$).

ID	Name	R_{GC}	$E(B-V)$	$(m-M)_V$	M_{Vt}	[Fe/H]	c	r_t	$\log(t_h$	$\log(\rho_0)$
NGC 6584		7.0	0.10	15.95	−7.68	−1.49	1.20	9.37	9.09	2.92
NGC 6624		1.2	0.28	15.37	−7.50	−0.42	2.50c	20.55	8.74	5.25
NGC 6638		1.6	0.40	15.85	−6.83	−0.99	1.40	6.63	8.51	4.05
NGC 6637	M 69	1.6	0.16	15.16	−7.52	−0.71	1.39	8.35	8.79	3.81
NGC 6642		1.6	0.41	15.70	−6.57	−1.35	1.99	10.07	8.49	4.72
NGC 6652		2.4	0.09	15.19	−6.57	−0.96	1.80	4.48	8.55	4.54
NGC 6681	M 70	2.1	0.07	14.98	−7.11	−1.51	2.50c	7.91	8.83	5.41
NGC 6712		3.5	0.45	15.60	−7.50	−1.01	0.90	7.44	8.98	3.14
NGC 6717	Pal 9	2.3	0.20	14.95	−5.67	−1.29	2.07c:	9.87	8.26	4.65
NGC 6723		2.6	0.05	14.87	−7.86	−1.12	1.05	10.51	9.30	2.81
NGC 6760		4.8	0.77	16.74	−7.86	−0.52	1.59	12.96	9.39	3.84
NGC 6838	M 71	6.7	0.25	13.75	−5.56	−0.73	1.15	8.96	8.41	3.05
NGC 6864	M 75	12.8	0.16	16.87	−8.35	−1.32	1.88	7.28	9.08	4.51
NGC 6934		14.3	0.09	16.48	−7.65	−1.54	1.53	8.37	9.07	3.37
NGC 6981	M 72	12.9	0.05	16.31	−7.04	−1.40	1.23	9.15	9.20	2.35
NGC 7078	M 15	10.4	0.10	15.37	−9.17	−2.25	2.50c	21.50	9.35	5.38
NGC 7089	M 2	10.4	0.06	15.49	−9.02	−1.62	1.80	21.45	9.32	3.90
NGC 7099	M 30	7.1	0.03	14.62	−7.43	-2.12	2.50c	18.34	8.95	5.04

TABLE 6.4— Main Parameters of the Clusters (continued).

6.3.2 The correction for CTE

In order to calibrate our photometry, we followed the procedure outlined in Dolphin (2000). This accounts for both the charge transfer (in)efficiency (CTE) and the variation of the effective pixel area across the WFPC2 field of view, and it yields final calibrated magnitudes in either the Johnson photometric system or the HST one. As a first step, a softened background was calculated from the actual output of ALLFRAME (after multiplying by the gain value $G = 7$ or 15, so counts are expressed in electrons) as follows. Negative values of the background were set to zero, and then the background counts (B) were replaced by $\sqrt{(1+B^2)}$. The counts in electrons $D = G \times 10^{-0.4\,(m-25)}$ were then computed for each star magnitude. (Note that DAOPHOT sets a star magnitude to $m = 25$ for stars with a flux corresponding to one count above the sky background.) The B and D values were then used to find the CTE (and pixel area) correction to magnitude m, which is computed as $m = m - C$, where $C = Y + X$ and

$$\mathrm{X}=\frac{x}{800}(0.024 + 0.002 \cdot yr) \cdot \exp\left[-0.196(\ln D - 7) - 0.126(\ln B - 1)\right]$$

$$\mathrm{Y}=\frac{y}{800}\{0.018 + (0.097 + 0.041 \cdot yr) \cdot (0.088 + \exp\left[-0.507(\ln D - 7)\right])\cdot$$
$$\cdot \exp\left[-0.035(\ln B - 1) - 0.042 \cdot B\right]$$

The CTE correction depends on the epoch of the observations (yr), which is expressed, in the D00 equations, relative to the reference epoch 1996.3. The coefficients of the equations were taken from Table 1 of D00, which is appropriate for observations made after April 23, 1994, when the camera was cooled

from $-76°$C to $-88°$C. The corrected magnitudes were then calibrated to both the Johnson and HST flight systems, going through the steps described in the following Section.

6.3.3 Transformation to the standard photometric systems

The first step was to find the aperture corrections from ALLFRAME magnitudes to the reference aperture of $0.5''$ used by Holtzman et al. (1995). A set of bright isolated objects was selected, all their neighbors were subtracted, and aperture photometry was performed within the chosen set of radii. The aperture corrections were then defined as $AC = m_{\rm PSF} - m_{0.5''}$, and median values were computed. Generally the agreement between the zero points of the four chips is good ($\Delta m < 0.01$ magnitudes), but in some cases the procedure gave poor aperture corrections. This normally happened for the more crowded PC chip. In such cases, the aperture corrections were changed by a few hundredths of a magnitude in order to bring the PC photometry into agreement with the WF zero points. This procedure will of course erase any true magnitude offset introduced by a patchy reddening on arcmin scales, so we warn the readers that these data are not suitable for mapping the reddening within the sky area covered by the WFPC2.

Once the aperture corrections had been applied, the following procedure was followed. First, the aperture corrections AC_{555} and AC_{439}, and the interstellar absorptions A_{555} and A_{439} were subtracted from the instrumental magnitudes. Since the absorptions depend on the true colours, which are not known at the beginning, we started with null values for A_{555} and A_{439}. From the corrected instrumental magnitudes m_{555} and m_{439} the provisional flight magnitudes were computed, as given by the D00 equations:

$$F555W = m_{555} + 21.734 + \Delta Z_{\rm CG}$$

$$F439W = m_{439} + 20.086 + \Delta Z_{\rm CG}.$$

In these equations, the filter- and temperature-dependent zero-points were taken from Table 6 of D00 (*Cold* $Z_{\rm FG}$ column), and the chip to chip zero-point differences $\Delta Z_{\rm CG}$ were in turn taken from Table 5. Explicitly, for gain 7 the values are 0.701, 0.761, 0.749, and 0.722 for the PC, WF2, WF3 and WF4 chips, respectively. For gain 15 the values are, in the same order of chips, -0.044, 0.007, -0.007, and -0.005.

The determination of the Johnson B and V magnitudes is complicated by the fact that they depend on the true colour of the star, so we followed an iterative procedure. Assuming $(B - V) = 1$, we computed the provisional

magnitudes as prescribed by D00:

$$V = F555W - 0.060 \times (B-V) + 0.033 \times (B-V)^2$$

$$B = F439W + 0.003 \times (B-V) - 0.088 \times (B-V)^2.$$

We then computed an updated value of $(B-V)$ and iterated until the difference between successive values of the magnitudes dropped below 0.001.

At this stage we are still ignoring interstellar absorption. However, we now have an estimate of the Johnson magnitudes, so we can compute a first provisional value of A_{555} and A_{439}. They can be subtracted, together with the aperture corrections, from the instrumental magnitudes, and the previous cycle can be repeated until new values for the absorptions are obtained. Indeed, the cycle was repeated until again the differences between successive values of V and B were smaller than 0.001.

The absorptions were computed in the following manner. The absorptions for two stars of spectral type K5 and O6 are given in H95 for the different HST filters, as a function of the reddening $E_{(B-V)}$. In order to compute the absorption for a star of any spectral type, two fiducial $(B-V)$ colours were assigned to the two reference types, $(B-V) = 1.15$ and $(B-V) = -0.32$, respectively. The absorptions for stars of intermediate colours were computed as linear interpolations between the values at the two colour extremes. Since the range in colour of our stellar populations is not extreme, the same linear interpolation was used also to compute the absorptions for stars falling outside the preferred colour range. The average reddening of each globular cluster was taken from the Harris (1996) catalog.

Table 6.5 shows an example of the final photometric file. Typically from a few thousands to about 47,000 (e.g. in NGC 6388) stars have been measured in each cluster. Figure 6.4 shows the final CMDs for the GCs NGC 6388 and NGC 6441, in the F439W and F555W HST flight system. This two blue tail metal rich clusters clearly exemplify the second parameter problem.

6.4 What determines the HB morphology in globular clusters?

The main contribution of the HST snapshot program to the objective of this thesis is the analysis of HB morphology for the clusters in the data set. As globular clusters span a large range in many of their properties, such as luminosity, density, etc., in order to reveal the possible complex correlations hidden in the HB second parameter problem, we decided to apply a multivariate statistical analysis. In other words, as we are dealing with a multidimensional data set,

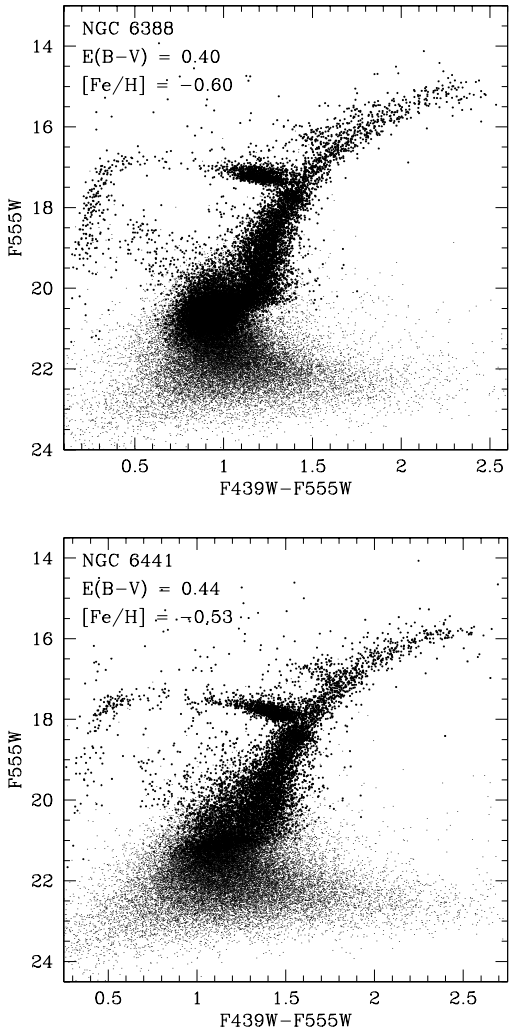


FIGURE 6.3— The HST snapshot CMDs of the metal rich blue tail clusters NGC 6388 and NGC 6441.

we decided to apply a multivariate statistical analysis to disentangle how HB morphology depends on cluster parameters.

6.4.1 Determination of effective temperature along the HBs.

The first step in this work consists in the evaluation of the cluster's HB morphology. In order to have a quantitative measure of their extension, we determined the highest effective temperature reached by the stars in the HBs of all the clusters in our data set by fitting a ZAHB model to the observed CMDs. In this way, we can study how the extension of the horizontal branch varies with cluster parameters. It is worth to point out, however, that HB bimodality, i.e. the presence of both a red HB and a blue tail as in NGC2808, is not been taken into account with this approach.

Distance modulus and reddening in flight system.

In order to accurately fit ZAHB models to our $[F439W, F555W]$ CMDs, we have first derived a value of distance modulus and reddening for each of the clusters in the data set. The distance modulus in the $F555W$ band was determined by calculating the ZAHB apparent and absolute magnitude, via the following procedure:

- **Low-intermediate metallicity clusters**:

  1. The RR-Lyrae level in the V band was first determined for 5 blue HB clusters in our sample, which have low reddening, accurate photometry and a high number of RR-Lyrae taken from the literature. To do this, we overlapped their snapshot $[V, (B-V)]$ CMDs with their corresponding literature CMDs as in Figure 6.4. The histogram of the observed RR-Lyrae (plotted in magenta) allowed us to establish the RR-Lyrae level. The selected clusters and their literature references were: NGC 6362 (Walker, 2001, private communication), NGC 1851 (Walker, 1998), NGC 5904 (Caputo et al., 1999), and NGC 4590 (Walker, 1994), with [Fe/H] equal to -0.96, -1.20, -1.11, and -1.99 respectively (Carretta & Gratton, 1997). To these four clusters, we added NGC 1904 ([Fe/H]= -1.37) by comparing its CMD with that of NGC 5272 ([Fe/H]= -1.41) by Buonanno et al. (1994). Finally, we identified each of these five template cluster's RR-Lyrae level in their snapshot flight system CMDs.

  2. The RR-Lyrae magnitude in $F555W$ was then established for the other low-intermediate metallicity clusters in our sample using the above 5 template clusters. The CMD in flight system of the template with the most similar metallicity was shifted in magnitude and colour, over the

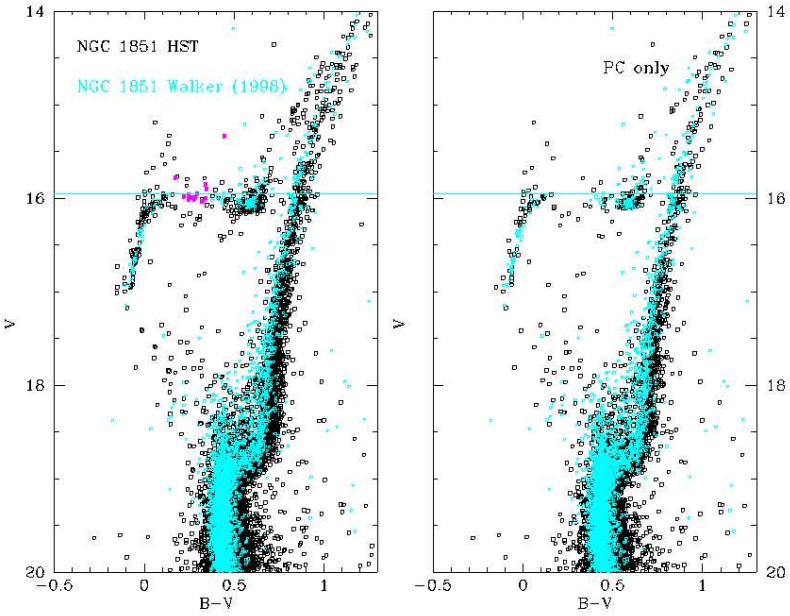


FIGURE 6.4— Determination of the RR-Lyrae V magnitude for the cluster NGC1851, using the Walker (1998) ground based photometry as a template. RR-Lyrae are plotted in magenta.

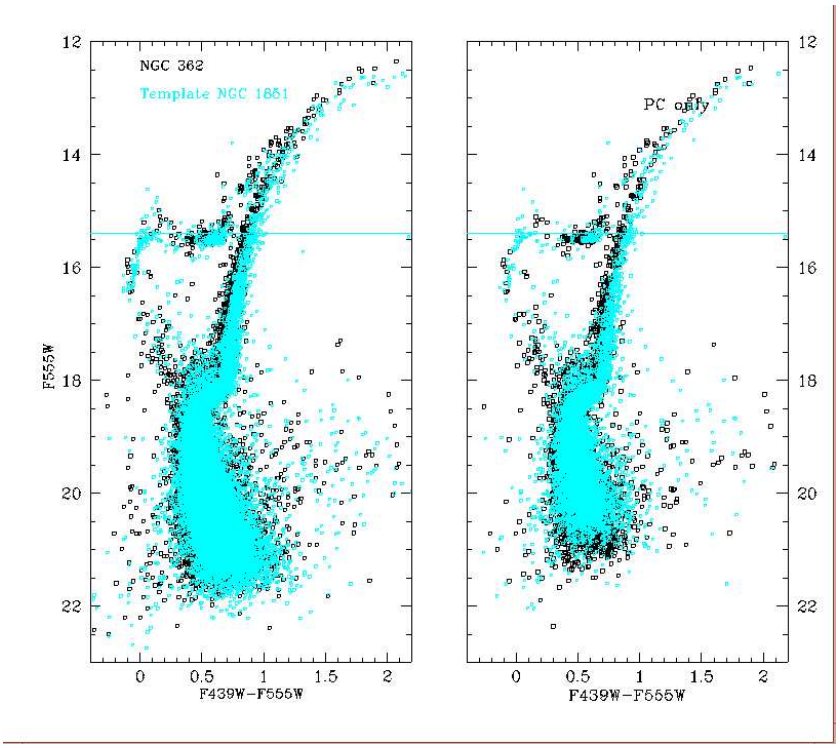


FIGURE 6.5— Determination of the RR-Lyrae $F555W$ magnitude of the cluster NGC0362 using the NGC 1851 as a template.

CMD of the cluster we wanted to measure, until their HBs overlapped, as illustrated in Figure 6.6. In particular, we carefully matched the blue HBs at the point where HB becomes vertical in the $[F555W, (F439W - F555W)]$ plane. This point depends only on bolometric correction, and is independent on metallicity (Brocato et al. 1998). This procedure allowed us to obtain the $m_{F555W}^{RR-Lyrae}$ magnitude and the $E(F439W - F555W)$ reddening for each cluster.

3. We calculated each cluster's apparent ZAHB magnitude via the formula by Cassisi & Salaris (1996):

$$m_{F555W}^{ZAHB} = m_{F555W}^{RR-Lyrae} + 0.152 + 0.041[M/H]$$

with : $[M/H] = [Fe/H] + log(0.638f + 0.362)$; logf= $[\alpha/H]$

We have adopted $[\alpha/H] = 0.3$ for these clusters with [Fe/H] < -1.0 (Carney, 1996).

- **High metallicity clusters**:

  For clusters with [Fe/H] $\geq$ -1.0, in general with a red HB and no RR-Lyrae, the magnitude m_{F555W}^{ZAHB} was derived following the method by Fullton et al. (1995) and Zoccali et al. (1999), :

$$m_{F555W}^{ZAHB} = m_{F555W}^{le} - 3\sigma_v + 0.1$$

  Where m_{F555W}^{le} is the magnitude of the lower envelope or lower limit of the Red HB, previously determined by evaluating the horizontal branch histogram as shown in Figure 6.7. σ_v is the photometric error estimated through the artificial star experiments at the HB magnitude interval, being, in general, quite small with the corresponding deviations in magnitude, negligible. A cross-check of this method with the previous one gives consistent results.

The absolute ZAHB magnitude was then derived from (Cassisi, 1996):

$$M_{F555W}^{ZAHB} = 0.9824 + 0.3008[M/H] + 0.0286[M/H]^2$$
$$[M/H] = [Fe/H] + log(0.638f + 0.362)$$

In this case ([Fe/H] > -1.0) we adopted $[\alpha/H] = 0.2$ (Cassisi & Salaris, 1996).

Finally, the corresponding distance moduli were calculated by subtracting (m_{F555W}^{ZAHB} - M_{F555W}^{ZAHB}). Table 6.6 shows the distance moduli and reddenings obtained for our data set. Note that we have only worked with 61 of the 74 clusters in the snapshot sample, rejecting those high reddened clusters for which the above procedure introduced considerable errors.

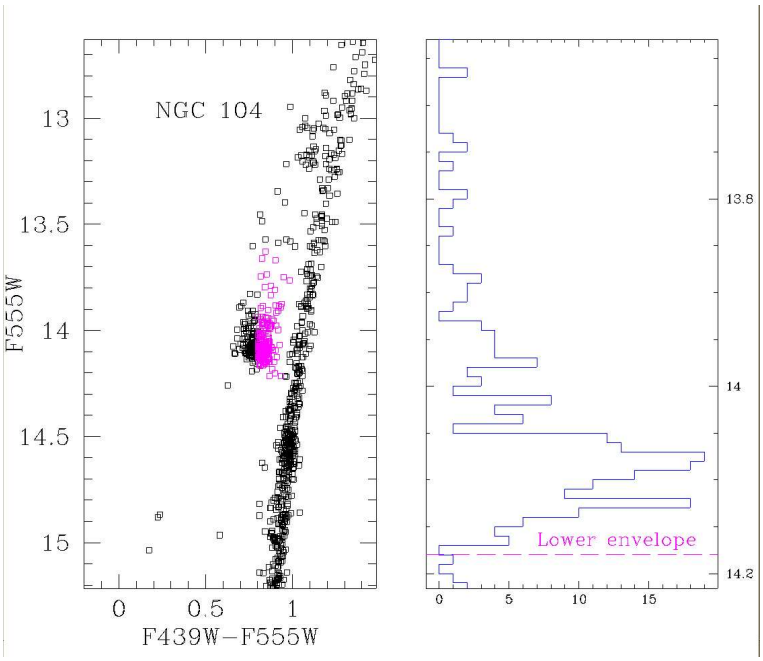


FIGURE 6.6— Determination of the RR-Lyrae F555W magnitude for the metal rich cluster NGC 104. Note that the magnitude scale of the right panel is different from that of the left one. The right panel shows the histogram only of the part of the HB plotted in magenta.

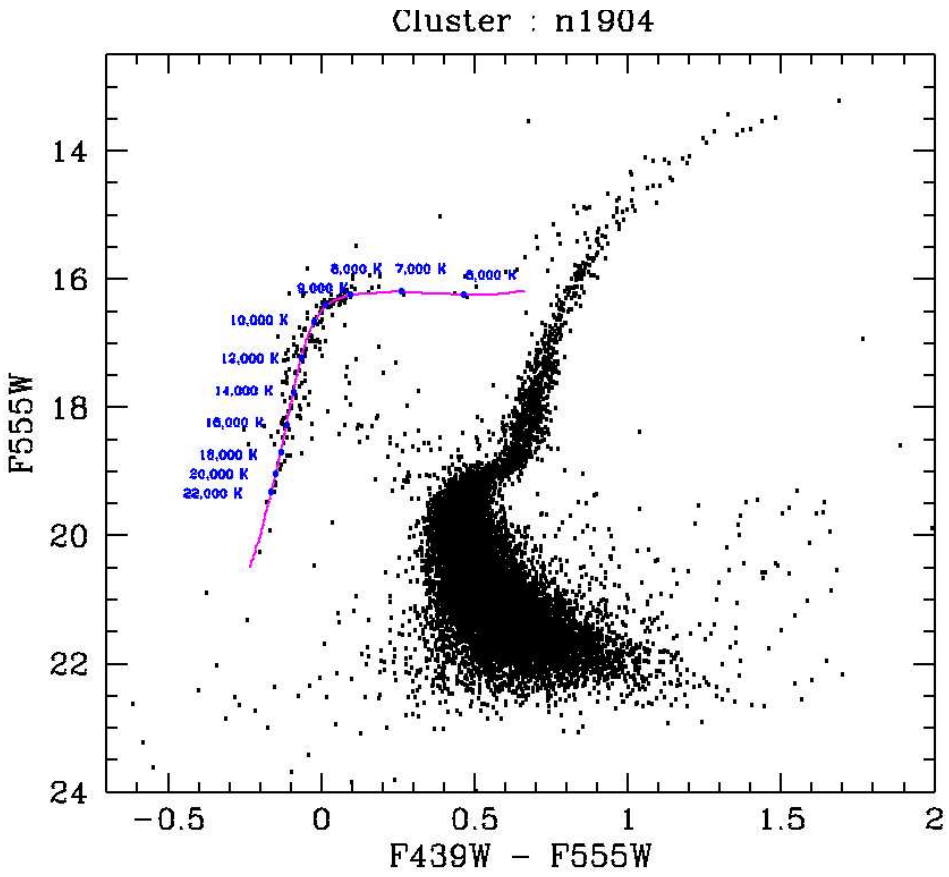


FIGURE 6.7— ZAHB model by Cassisi et al. (1999) fitted to NGC 1904 colour-magnitude diagram. The effective temperature variation along the HB is also shown.

Fitting ZAHB models to the observed HBs.

Using the distance moduli and the reddening previously determined, we fitted ZAHB models by S. Cassisi to the colour-magnitude diagrams. This procedure allowed us to evaluate the highest $T_{\rm eff}$ reached by the globular cluster HB and therefore its temperature extension, as illustrated in Figure 6.8. The errors in this temperature determination are difficult to estimate as they depend not only on the errors in (m^{ZAHB}_{F555W} - M^{ZAHB}_{F555W}) and reddening, but also on the number of stars in the HB and the temperature range we have to deal with. As a consequence, the largest errors occurred for the smallest low central concentrated clusters, and for the most extended HBs, where the large bolometric correction in these photometric bands precludes an accurate estimation of $T_{\rm eff}$.

However, although the errors can be rather important, the general trend of HB morphology with cluster parameters is not dramatically affected, as we will see in section 6.4.6. Figure 6.8 shows the ZAHB model fit to the NGC 1904 CMD. The corresponding temperatures along the HB are marked.

Table 6.7 gives the values of the different cluster parameters. The second column is the logarithm of the calculated HB highest effective temperature, $\log(\mathrm{Teff}_{HB})$, the collisional parameter, listed in column 5, is defined as the number of collisions per unit time and it was derived via the formula (King, 2002):

$$\Gamma_{col} = log[5 \cdot 10^{-15}\sqrt{\sigma^3 \cdot r_c}]$$

where σ is the central surface brightness in units of $\mathrm{L}_{\odot}/\mathrm{pc}^2$:

$$\sigma = 10^{[-0.4\cdot(\mu_V - 26.41)]}$$

The other quantities in Table 6.7 (see table's caption) are taken from Harris (1996).

6.4.2 Considered cluster parameters.

In order to disentangle the dependence of the HB morphology on as many cluster parameters as possible, we have first considered the 14 quantities listed in Table 6.7: the logarithm of the hottest temperature in the HB ($\log(\mathrm{Teff}_{HB})$), cluster metallicity ($[Fe/H]$), absolute V magnitude (Mv_t), collisional parameter(Γ_{col}), central concentration (ρ_0), logarithm of central luminosity density (c), distance from Galactic center (R_{GC}), Galactic longitude (L) and latitude (B), core radius (r_c), half-mass radius (r_h), the logarithm of core relaxation time (t_{rc}), the logarithm of relaxation time at half-mass radius (t_{rh}) and the central surface brightness (mu_V).

After evaluating the most important monovariate correlations between the hottest temperature reached on HB and the previously mentioned cluster parameters, we ignore the 5 derived quantities (c, r_c, r_h, t_{rc}, t_{rh}), and we take only a subset of 8 quantities measured independently: $\log(\mathrm{Teff}_{HB})$, $[Fe/H]$, Mv_t, Γ_{col}, ρ_0, R_{GC}, B and r_h. The galactic longitude, L, has also been excluded because it can be derived from R_{GC} and B. With this parameter set we start a multivariate approach of the problem. We will show that the analysis reflects a dimensionality of the set of at least 4 or 5, suggesting to work with a smaller subsample of parameters, as a more profitable approach to explore the HB morphology dependences. Therefore, we finally study the bivariate and trivariate correlations of $\log(\mathrm{Teff}_{HB})$ with those parameters that presented the highest monovariate

correlations with HB morphology, discussing their theoretical implications and statistical significance.

In this analysis we could not forget an important parameter for HB morphology as it is cluster age. For this reason, although age it is not included in the initial set of parameters, due to the lack of a complete and uniform age estimate for all our sample clusters, we have evaluated its correlation with HB morphology in a subsample of 19 clusters in common with Rosenberg et al. (1999). The result of this analysis, together with the other parameter's influence on cluster HB extension, is presented in the following sections.

6.4.3 Monovariate correlations.

We first explore the simple, pairwise correlations between the HB extension and a number of selected globular cluster properties, via the Pearson correlation coefficient, **r**.

This coefficient gives the ratio between the observed covariance and the maximum possible positive covariance for the two evaluated quantities, **x** and **y** . Therefore, the value of **r** goes from perfect negative correlation (r=-1) to perfect positive correlation (r=+1). The midpoint of this range, r=0.0, corresponds to a complete absence of correlation.

The coefficient of determination, $\mathbf{r}^2$, represents the correlation strength. The value of $\mathbf{r}^2 \cdot 100$ is the percentage of variability in **y** associated with variability in **x**, in other words, the percentage of variation in **y** explained by a variation in **x**.

Table 6.8 lists the Pearson linear regression correlation coefficients, **r**, for the 14 quantities explored. Columns in table 6.8 list the same quantities as in table 6.7.

As we have said, only 8 parameters are measured independently. In general, correlations of any of the derived quantities with any of their constituent quantities or combinations do not provide new information. On the other hand, Table 6.8 immediately suggests some interesting correlations that we will try to analyze next.

- **Metallicity: the first parameter.**

  The first correlation to be explored is the HB morphology-metallicity dependence. As explained in Chapter2, metallicity is the so called first parameter regulating the extension of the horizontal branch. This dependence can be derived naturally from canonical stellar evolution models. Figure 6.9 shows the trend of $\log(\mathrm{Teff}_{HB})$ with [Fe/H]. Clearly, there is a correlation among both quantities in the sense that the less metallic the

cluster is, the more extended its HB tends to be (and, hence, the higher in log(Teff$_{HB}$)), as expected from theoretical models. However, the data indicate, as we already knew, that variation of log(Teff$_{HB}$) from cluster to cluster is not completely explained by the [Fe/H] parameter. This observational evidence is the core of the second parameter problem, already introduced in Chapter 2. The value of the Pearson correlation coefficient for these two quantities is r $\simeq$ -0.57, indicating that metallicity explains the 32% of the total variation of log(Teff$_{HB}$). A simple least-square fit is also plotted in Figure 6.9, giving a rms value of 0.18.

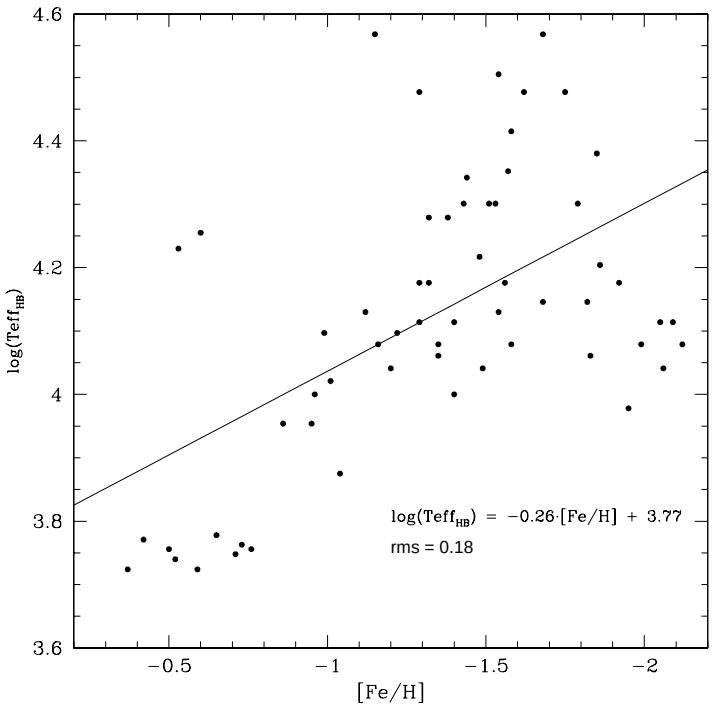


FIGURE 6.8— Correlation of HB morphology with metallicity (the first parameter). HB morphology is parameterized via the highest effective temperature reached in the HB, log(Teff$_{HB}$).

- **Absolute V magnitude**

  Probably one of the most interesting results of this simple correlation approach is the finding of a clear correlation between HB morphology and total luminosity of the cluster. This correlation, never noticed before, apparently is of importance slightly smaller than the one observed with

the first parameter. The Pearson coefficient relating these two variables is r $\simeq$ -0.44. Therefore, variation of total luminosity is responsible for the 19% of the HB morphology variation. Graphically, this trend is shown in Figure 6.9, upper panel. in which the correlation of log(Teff$_{HB}$) with absolute V magnitude for 3 different metallicity intervals is presented. More luminous clusters, tend to have hotter (bluer) horizontal branches. Interestingly, the highest correlation is observed for intermediate metallicity clusters (green dots) where the first parameter effect is less important. On the other hand, if we calculate the Pearson coefficient between absolute V magnitude and log(Teff$_{HB}$) only for the subsample of clusters with the more extended HBs, log(Teff$_{HB}$) $>$ 4.3, we find a much more clear correlation, reaching a value of r= -0.85. The bottom panel of Figure 6.10 shows again the trend of log(Teff$_{HB}$) with metallicity, but using different point sizes depending on the value of absolute V magnitude. Clearly, some of the dispersion in the first parameter correlation can be explained by M$_V$. That is the case of the metal-rich blue tail clusters NGC6388 and NGC6441, which have M$_V$ $<$ -9, and are among the more luminous clusters in the sample.

On the other hand, as all globular clusters have similar colour indices and hence similar bolometric corrections, M$_V$ is a good estimation of total luminosity. In addition, luminosity is perhaps the most fundamental observed quantity characterizing a stellar system, and for a set of old stellar systems it is a good relative measure of its baryonic mass. Therefore, the observed trend seems to suggest that, for some reason, more massive clusters tend to have bluest horizontal branches. We will come back to this point in section 6.5, where we will discuss its possible theoretical implications.

- **Collisional parameter**

  Quite significant is also the correlation among log(Teff$_{HB}$) and the collisional parameter (r$\simeq$0.39, 15% of the total HB morphology variance). The highest the probability of stellar collisions, the hottest the HB is. This trend is presented in Figure 6.11, on the upper left panel. Note that this parameter, is sensibly correlated with absolute V magnitude too (see Table 6.8), with more luminous clusters having a highest value of Γ_{col}. However, formally, the collisional parameter is independent on M$_V$, as it has been calculated using the μ_V and the r$_c$ parameters. The connection between M$_V$ and μ_V might therefore also explain the correlation of Γ_{col} with M$_V$.

The role of Γ_{col} is important to explain for example, the difference in the HB extension of the clusters NGC5634 and NGC 5694 (4.14, and 4.21], which have very similar metallicities (-1.82 and -1.86 respectively) and total luminosities (-7.7 and -7.81) but differ in their Γ_{col} values (-8.8 and -8.3). The cluster with the highest collisional probability (NGC 5694) is the one with the bluest HB.

Finally, it is important to note that the high value of the correlation between log(Teff$_{HB}$) and μ_V (see Table 6.8) could be a consequence of the log(Teff$_{HB}$)-Γ_{col} correlation, as μ_V is included in the formula of Γ_{col}, or it could be reflecting the log(Teff$_{HB}$)-M$_V$ correlation, as μ_V and M$_V$ are highly correlated.

- **Central density**

  Figure 6.11, upper right panel shows the trend of HB morphology with the central concentration of the cluster. Our analysis indicates a very weak correlation among both quantities (r$\simeq$0.16, 2.6% of the total HB morphology variance). Contrary to previous studies (Fusi Pecci et al. 1993), our sample indicates that cluster density is not a "good" second parameter, as it has a very little influence in HB morphology. Close encounters and tidal stripping, also suggested by Fusi Pecci et al. (1993) as a possible origin of bluer HB stars, are probably better represented by the collisional parameter.

- **Other simple correlations**

  Other quantities with which HB morphology seems to have a little but, may be still significant correlations are the distance to the Galactic center, R$_{GC}$ (r$\simeq$0.19, 4% of the total log(Teff$_{HB}$) variance) and half mass radius (r$\simeq$0.18, 3%). The first one, may also be a secondary effect of the first parameter, as [Fe/H] has an already known trend with R$_{GC}$.

- **Age**

  Finally, although globular cluster age was not included among the initial parameters explored in our sample, we have evaluated this very important HB morphology dependence in a subsample of 19 clusters, in common with the Rosenberg et al. (1999) data base (see the Table 6.9 and Figure 6.11, bottom left panel). The relative ages of the 19 clusters go from 0.77 for the youngest cluster in the sample (NGC 1261) to 1.04 for the oldest one (NGC6093). These relative ages are normalized to the average age of the oldest clusters as explained by Rosenberg et al. The derived Pearson correlation coefficient between log(Teff$_{HB}$) and age is r= 0.22 (5% of

the HB morphology variance of the cluster's subsample), with the oldest clusters having the bluest horizontal branches, as expected from theoretical models. This result, however, confirms the fact, already pointed out by Rosenberg et al. (1999), that age can not be the only explanation for the second parameter problem. But our results go further. The correlations discovered here indicate that total luminosity and collisional parameter play a more important role than age defining the extension of the HB.

6.4.4 A multivariate approach.

While the simple approach of examining individual monovariate correlations of $\log(\mathrm{Teff}_{HB})$ with cluster parameters gives us a good first look at the problem of HB morphology, the complexity of the situation calls for a more sophisticated strategy. We are dealing with a multidimensional data set, in which sets of several observables may be connected in multivariate correlations. Simple, monovariate correlations are only a special and rare case. In particular, the different trends of $\log(\mathrm{Teff}_{HB})$ illustrated above indicate that the problem of GC HB morphology is intrinsically statistically multidimensional, and that must be attacked using a multivariate approach.

Some useful concepts in multivariate analysis.

Before presenting the multivariate analysis results, we will briefly explain the principal concepts of multidimensional techniques for data treatment (see also Djorgovski & Meylan, 1994). The data points occupy a volume in an N-dimensional parameter space, where N is the number of input quantities (in this case, N=14). If any of the input quantities are derived from the others, the data will occupy a volume of dimension M, where M is the number of *independent* input quantities (in this case, M=8, as we have seen in Section 6.4.2). If, in addition, any correlations are present in the data, the dimensionality of the volume occupied by the data points, also called the data manifold, would be $D \leq M$, and gives the number of independent factors which fully describe the data. For example, if all the input quantities are perfectly correlated, D=1. This minimum number of dimensions needed to account for the spread in the data may reflect the number of physical processes or controlling parameters which determine the observable properties of objects being studied. If there are no correlations, the data points will spread over the full M-dimensional volume of the parameter space. The dimensionality of the data manifold is thus a sensitive indicator of whether any correlations are present, regardless of their complexity.

Subsets of input variables, or even all of them, may be mutually connected in a set of K-variate correlations, i.e., each variable can be correlated, within the measurement errors, with combinations of K others. Some of the input quantities may be uncorrelated with any of the others, and would thus automatically increase the dimensionality of the data manyfold. Finding a subset of the data for which a non trivial reduction of dimensionality occurs is the process by which the correlations may be inferred.

The procedure by which this can be accomplished is principal component analysis (PCA). In its simplest form, it consists in diagonalizing a matrix of pairwise correlation coefficients (e.g. those given in Table 6.8). It is the eigensolution of the data ellipsoid in the N-dimensional parameter space of measured quantities. The data should be properly linearized first; for most astronomical applications, where correlations are power laws, this is usually accomplished by taking logarithms (as in the case of $\log(\mathrm{Teff}_{HB})$). Ideally, every input quantity should have a Gaussian distribution; if not, the derived correlations may be biased, but the dimensionality will still be right. Typically the input data are renormalized by subtracting the mean and dividing by the sigma in each of the input variables. The renormalization does not affect the qualitative nature of the PCA solutions, but it may affect the statistical significance of the higher data dimensions.

The principal axes (eigenvectors) of the data ellipsoid may be tilted with respect to any of the observables. Their mutual relations are usually represented through correlation vector diagrams, which show the projections of input variables' axes to the principal planes given by the eigenvectors. The number of the significant eigenvalues, i.e., those larger than expected from the measurement errors, gives the dimensionality of the data manifold, D. Each of the eigenvectors also accounts for a fraction of the total sample variance. It is generally agreed that eigenvalues >1 are statistically significant, but somewhat lower ones may be as well, depending on how the data were normalized. Usually, a steep drop in the successive eigenvalues or in the fractional contributions to the sample variance indicates where the number of statistically significant dimensions stops, and where the noise begins. But the case is not always so clearcut. Finally, if any correlations are present, their equations can be deduced from the transformations connecting the eigenvector components and input variables.

The global manifold

First of all, we performed the PCA on our dataset, using all independent input variables. We ignored the derived quantities, ρ_0, t_{rc}, t_{rh}, as they do not add to the dimensionality of the data manifold. In addition, of the three related

variables R_{GP}, l and b, we chose only R_{GP} and B. In the same way, among the group of variables formed by Γ_{col}, μ_V and r_c, we took only Γ_{col}, as it contains the other two parameters in its formula. The monovariate correlations for the 8 independent quantities explored are presented in Table 6.10. We point out, once again, that cluster age is not considered for the moment in this general set of parameters. It will be taken into account later for a subset of clusters.

Table 6.11 presents the eigenvalues (e_i), fractional (V_i) and cumulative (C_i) contributions to the total sample variance, in percent, for the obtained PCA solution. Figure 6.11 shows the results of the PCA, as applied to the entire above set of independent input variables, in the form of correlation-vector diagrams. There are at least four, but probably as many as eight statistically significant dimensions in this data set, although the possible significativity of the last four eigenvectors is masked by the noise in the data. The first four eigenvectors account for the 79.4% of the total sample variance. They define a natural coordinate system for this data set. Projections of the input axes to the principal planes given by the eigenvectors (ξ_1, ξ_2), (ξ_1, ξ_3) and (ξ_1, ξ_4) are the correlation-vector diagrams as shown in Figure 6.11. In this representation, vectors corresponding to well-correlated variables define sharp or plane angles; uncorrelated quantities have orthogonal vectors in this projection. It is important to notice again that we are now considering a new coordinate system, where the new variables are the eigenvectors, which, in general, do not coincide with the original variables, the cluster parameters.

Bivariate and trivariate correlations: the role of M_V and cluster age.

Obviously, the situation is quite complex, reflecting the statistical multidimensionality of the entire manifold of globular cluster properties (c.f. Djorgovski 1991). Given the limited data set, a more profitable approach is to consider only a subset of variables. To illustrate the point, we will consider only $\log(\mathrm{Teff}_{HB})$, $[Fe/H]$ and M_V. We find that for this data subset of three input variables (see Table 6.12), at least two statistical dimensions are necessary. The first two eigenvectors account for the 57% and the 33% of the total sample variance, respectively. The remaining 10% could be accounted by the errors, which are quite difficult to evaluate as explained in the previous sections. If this is true, a weighted vector sum of [Fe/H] and M_V vectors could correlate much better with $\log(\mathrm{Teff}_{HB})$ than [Fe/H] or M_V alone. This is shown in Figure 6.12 where the bivariate correlation involving this 3 input quantities is shown. Clearly, the dispersion is now smaller than the one observed in any of the monovariate correlations for the total cluster sample. This bivariate correlation works specially well for clusters with $\log(\mathrm{Teff}_{HB}) > 3.8$ ($\mathrm{Teff}_{HB} \geq 6000$ K), that is, clusters

with at least some blue HB stars. In fact, if we perform the previous bivariate analysis considering only these clusters, we find a very clear correlation, as shown in Figure 6.13.

On the other hand, we have also explored the trivariate correlation of HB morphology with $[Fe/H]$, M_V and Age for the subsample of 19 clusters in common with Rosenberg et al. (1999), in order to possibly reduce the scatter in the previous bivariate relation, due to possible effects of age. The corresponding PCA results are presented in Table 6.13 and Figure 6.14. The third eigenvector significance, 14.1%, increases with respect to the combination of $[Fe/H]$ and M_V. Now, the first three eigenvectors account for the 92.4 % of the total variance. The residual scatter is, therefore, of the order of the measurement errors. After all, age might also influence the HB morphology. The spread of the clusters, NGC 104, NGC 362, NGC 1851, known to be younger than the mean (Rosenberg et al. 1999), is, in fact, smaller than for the bivariate relation (Figure 6.12). The cluster NGC 7078 (plotted in red) is suspected to be related to a stream (Yoon & Lee, 2002). On the other hand, NGC 104 is still very far from the general trend of the clusters, indicating that some other mechanism has to be invoked, to explained its horizontal branch morphology.

Bivariate and trivariate correlations: the role Γ_{col}.

Collisional parameter, as illustrated in Section 6.4.3, shows a correlation with HB temperature extension almost comparable to that of total luminosity. In addition, this parameter has a direct theoretical interpretation, as more stellar collisions could imply an increase in mass loss by tidal stripping, and therefore bluer HB stars. For this reason, we have also performed the bivariate correlation between $\log(\mathrm{Teff}_{HB})$ and the optimized combination of metallicity and Γ_{col}. The PCA results are presented in Table 6.14 and Figure 6.15 illustrates the resulting correlation. Clusters with a central concentration value $c > 1.7$ are plotted as squares. As for the case of a combination of metallicity and absolute V magnitude, this bivariate correlation improves significantly the interpretation of HB temperature extension. The remaining spread, again, could be considered to be due to the errors in the involved parameters, specially if we note that those clusters with a higher deviation from the general trend are those with higher central concentration, that is, clusters which have already undergone core collapse or which are closer to it (see Figure 6.15, square points). In those cases the value of the collisional parameter is probably not a good estimate of the collisional probability in their cores.

Although most of the information on HB temperature extension is already contained in the bivariate correlations involving either $[Fe/H]$ and M_V or

$[Fe/H]$ and Γ_{col}, and the remaining spread in both relations is probably mainly due to the parameter errors, we finally consider a set of four input quantities: $\log(\mathrm{Teff}_{HB})$, $[Fe/H]$, M_V and Γ_{col}, which are the independent parameters with the highest monovariate correlations with HB morphology. Table 6.15 shows the PCA results. The statistical significance of the third eigenvector marginally increases: the first three eigenvectors account for the 93% of the total sample variance. This result would suggest a trivariate correlation between $\log(\mathrm{Teff}_{HB})$ and a combination of $[Fe/H]$, M_V and Γ_{col}, very near to the complete description of the problem, given the finite measurement errors.

Figure 6.16 shows the final trivariate correlation. As expected, the spread for clusters with redder HBs decreases with respect to the bivariate correlation. At this point, very few exceptions remain which have a deviation, from the general trend of the clusters, bigger than what is probably the spread due to measurement errors. Figure 6.17 indicates (in red) the already known clusters with ages younger than the mean (from Rosenberg et al. 1999), plus some clusters suspected to be related to satellite dwarf galaxy streams (Fusi Pecci et al. 1995; Lynden-Bell & Lynden-Bell, 1995; and Yoon & Lee, 2002). The dispersion of the trivariate correlation clearly decreases if those clusters are not considered. This result could indicate that the GCs accreted from satellite dwarf galaxies somehow differ from the clusters originally born in the Galactic halo. However, the sample is too small to allow any firm conclusion. Nevertheless, it is quite important to note, once again, that all these "deviating" clusters, have considerably high central concentrations. This is clearly observed in the distribution of clusters with $c > 1.7$, plotted as squares in Figure 6.16. In addition, NGC 362, NGC 7099 and NGC 7078 are core collapsed. As a consequence, we can also think that the determination of the collisional parameter for these clusters, can be somehow overestimated, producing the observed spread.

6.5 Summary and discussion: theoretical implications.

In this section, we will try to organize the results of the multivariate analysis presented above, and to shed some light in their possible theoretical meaning.

As it has been well discussed by Djorgovski et al. (1993) the GC manyfold is rather complex, and this is perfectly true also when we focus our attention on the problem of the GC HB morphology and of its dependence on the cluster parameters. In the previous section, we have shown that at least three parameters, but probably up to eight, are needed to reproduce the HB extension in temperature. As Fusi Pecci, Buonnanno and collaborators (see for example Fusi Pecci et al; 1993), among others, have been saying in the last 20 years or so, there is no single "second parameter" which can explain the HB anomalies,

but a combination of parameters.

The present analysis, based on 63 GCs of the HST snapshot catalogue, has given a few interesting new results which are worth of further discussion.

At least one new interesting conclusion can be derived: *the importance of total cluster luminosity (or collisional parameter), and therefore of total mass (or stellar collisions), on the horizontal branch morphology.* This effect, combined with the first parameter, can explain probably the major part of the Galactic globular cluster horizontal branch morphologies. More massive clusters (i.e. more luminous) tend to have more extended horizontal branches. Clusters with a higher collisional parameter tend also to have more extended HBs. Although these two parameters, M_V and Γ_{col} are partially correlated (see Table 6.8) they are not completely equivalent: less massive (luminous) clusters can present a high collisional probability if they are highly concentrated (see Γ_{col} defition in Section 6.4.1).

In general, metal-rich clusters with anomalously extended HBs, as NGC6388 and NGC6441, are more massive, or have higher collisional probability, than metal-rich clusters with redder HBs. In the same way, metal-poor clusters with shorter HBs, seem to be the less massive ones or those with lower values of Γ_{col}.

Taking into account the above descrived results, the most direct implication is to relate close encounters and tidal stripping in the bigger and more concentrated clusters (with a higher collisional parameter) to the origin of blue HB stars. In this scenario, clusters with a higher Γ_{col} would have an additional source of mass loss in the RGB phase, producing less massive and so bluer stars in the HB.

Another possible interpretation to the considerable influence of M_V and therefore, of cluster total mass, on HB morphology can be derived from the recent paper by D'Antona et al. 2002. As described in Chapter 2, they analyse the consequences, on HB morphology, of helium variation due to self-pollution among globular cluster stars. Self-pollution had already been proposed as an explanation for the chemical inhomogeneities (spread in the abundances of CNO, O - Na and Mg anticorrelation) observed in GC members from the main sequence to the RGB (see for example Gratton et al. 2001). The ejecta of massive asymptotic giant branch stars, which would be the origin of the self pollution, would not only be CNO processed, but also helium enriched. D'Antona et al. (2002) models take into account this possible helium enhancement with respect to the primordial value. They find that a spread in the helium content does not affect the morphology of the main sequence, turn off and RGB in an easily observable way. However, the difference in the evolving mass may play a role in the formation of blue tails, as higher helium structures are able to populate much bluer HB regions. If this is correct, self-polution and so helium

enrichment would be higher in more massive clusters, as they would be able to retain the material from the ejecta better than less massive clusters. On the other hand, even within this scenario, higher mass loss is needed in metal-rich clusters than in metal-poor ones, to produce bluer HB stars. And that could explain the observed relative higher influence of collisional parameter at higher metallicities.

To the above scenario, we have to add the effect of age, evaluated here only for 19 clusters with already known relative ages. This effect is important only for a very small number of clusters, significantly younger than the relative mean (NGC104, NGC362, NGC1261, NGC1851, NGC2808, NGC6838), and can be evaluated comparing the spread in Figure 6.14, where HB mophology is described using metallicity, total luminosity and age, with the spread of triangles in Figure 6.12, where only the bivariate correlation involving [Fe/H] and M_V is considered.

In any case, whatever is the theoretical interpretation of the data, it remains clear from this analysis of more than sixty Galactic globular clusters, that cluster total mass and stellar collisions have an important role in the horizontal branch morphology, and that their effects are larger than those of age.

ID	x	y	V	B	F555W	F439W	σ_{F555W}	σ_{F439W}
4	506.598	59.980	17.97	18.74	18.00	18.79	0.10	0.10
7	200.220	60.927	18.94	19.28	18.96	19.29	0.24	0.08
8	235.644	61.244	16.49	17.15	16.52	17.19	0.15	0.07
9	545.239	61.390	14.68	15.62	14.70	15.70	0.08	0.04
5	688.846	61.697	21.49	21.90	21.51	21.91	0.26	0.43
15	736.285	61.745	19.66	20.30	19.68	20.34	0.15	0.10
5603	537.317	62.062	18.96	19.48	18.99	19.50	0.16	0.08
12	445.775	62.208	18.65	19.37	18.67	19.42	0.09	0.06
14	636.699	62.301	18.00	18.65	18.02	18.69	0.08	0.06
11	119.039	62.725	17.59	18.03	17.61	18.04	0.09	0.06

$V_{\rm nr}$	$B_{\rm nr}$	F555W$_{\rm nr}$	F439W$_{\rm nr}$	χ	sharp	chip
18.13	18.94	18.16	19.00	2.206	0.046	1
19.09	19.49	19.11	19.50	1.821	−0.032	1
16.65	17.35	16.67	17.39	6.213	0.157	1
14.83	15.82	14.86	15.90	9.128	0.040	1
21.64	22.10	21.66	22.12	1.015	−0.282	1
19.81	20.51	19.84	20.55	1.421	−0.041	1
19.12	19.68	19.14	19.71	2.239	0.162	1
18.80	19.57	18.83	19.62	1.677	0.079	1
18.15	18.85	18.18	18.90	2.230	0.108	1
17.75	18.23	17.77	18.25	1.887	−0.032	1

TABLE 6.5— Example of a photometry file (NGC 104, 47 Tuc): Col. 1 gives a star identification number, Cols. 2 and 3 give the position on the chip, Cols. 4 and 5 the V and B standard magnitudes (reddening corrected), Cols. 6 and 7 the F555W and F439W magnitudes in the HST flight system (reddening corrected), Cols. 8 and 9 the photometric errors given by ALLFRAME, Cols. 10 and 11 the V and B standard magnitudes (before the reddening correction), Cols. 12 and 13 the F555W and F439W flight magnitudes (before the reddening correction), Cols. 14 and 15 the χ and sharp parameters as given by ALLFRAME, and Col. 16 the chip number (1 for PC, and 2, 3, 4 for WF2, WF3, WF4 respectively).

ID	m(ZAHB)$_{F555W}$	M(ZAHB)$_{F555W}$	(m-M)$_{F555W}$	E(F439W-F555W)
ic1257	20.20	0.60	19.60	0.71
n0104	14.26	0.81	13.35	0.07
n0362	15.51	0.72	14.78	0.005
n1261	16.85	0.68	16.17	0.01
n1851	16.16	0.71	15.45	0.02
n1904	16.26	0.63	15.63	0.01
n2808	16.36	0.73	15.63	0.14
n3201	14.86	0.62	14.23	0.24
n4590	15.73	0.52	15.20	0.05
n4147	16.99	0.57	16.42	0.01
n4372	15.58	0.52	15.06	0.40
n4833	15.70	0.58	15.12	0.28
n5024	16.83	0.54	16.29	0.01
n5634	17.69	0.57	17.11	0.01
n5694	18.53	0.56	17.97	0.12
n5824	18.53	0.56	17.97	0.12
n5904	15.20	0.69	14.51	0.03
n5927	16.89	0.91	15.81	0.53
n5946	17.60	0.67	16.93	0.63
n5986	16.71	0.62	16.08	0.26
n6093	16.35	0.59	15.76	0.21
n6139	18.05	0.60	17.45	0.71
n6171	15.79	0.75	15.03	0.48
n6205	15.06	0.63	14.42	0.01
n6218	15.10	0.65	14.45	0.21
n6229	18.10	0.66	17.44	0.02
n6235	17.00	0.67	16.33	0.30
n6256	18.23	0.84	17.39	1.18
n6266	16.30	0.69	15.61	0.53
n6273	16.55	0.60	15.95	0.33
n6284	17.50	0.68	16.82	0.28
n6287	17.13	0.53	16.60	0.65
n6293	16.48	0.55	17.05	0.61
n6304	16.49	0.85	15.64	0.53
n6325	18.06	0.72	17.34	1.02
n6342	17.17	0.84	16.33	0.51
n6356	17.75	0.88	16.87	0.33
n6362	15.42	0.78	14.65	0.08
n6380	19.64	0.90	18.74	1.58
n6388	17.39	0.85	16.54	0.37
n6401	17.86	0.73	17.13	0.90
n6402	17.40	0.67	16.73	0.65
n6440	18.95	0.94	18.00	1.48
n6441	18.06	0.87	17.19	0.48
n6453	17.81	0.64	17.17	0.61
n6517	19.20	0.67	18.53	1.23
n6522	16.80	0.66	16.14	0.53
n6539	18.53	0.85	17.68	1.08
n6540	15.96	0.71	15.24	0.52
n6544	15.26	0.63	14.63	0.76
n6569	17.72	0.78	16.94	0.56
n6584	16.59	0.65	15.95	0.02
n6624	16.21	0.90	15.31	0.40
n6637	16.14	0.82	15.32	0.23
n6638	16.97	0.77	16.20	0.38
n6642	16.70	0.68	16.02	0.43
n6652	16.16	0.75	15.41	0.13
n6681	15.76	0.64	15.12	0.06
n6712	16.22	0.76	15.46	0.38
n6717	15.90	0.69	15.21	0.22
n6723	15.56	0.73	14.83	0.05
n6760	18.02	0.87	17.15	0.88
n6838	14.55	0.83	13.72	0.26
n6864	17.70	0.68	17.02	0.20
n6934	16.96	0.63	16.32	0.08
n6981	16.90	0.67	16.23	0.05
n7078	15.72	0.49	15.23	0.09
n7089	16.03	0.62	15.42	0.01
n7099	15.22	0.51	14.71	0.03

TABLE 6.6— Apparent and absolute ZAHB F555W magnitude (Col. 2 and 3), corresponding distance modulus in F555W (Col. 4) and reddening in flight system (Col. 5)

TABLE 6.7— Parameters for the clusters included in the correlation analysis: Col. 1 gives the cluster identification, Col. 2 indicates the logarithm of HB highest effective temperature, and Col. 3 the cluster metallicity, Col. 4 is the total cluster luminosity in V or absolute visual magnitude, Col. 5 gives the collisional parameter, Col. 6 shows the logarithm of central luminosity density (in Solar luminosities per cubic parsec), Col. 7 lists the central concentration ($c = \log(r_t/r_c)$), Col. 8, 9 and 10 give the distance from Galactic center in kpc (assuming R_0=8.0 kpc), the Galactic longitude and latitude (degrees), Col. 11 and 12 give core radius and half-mass radius in arcmin, Col. 13 and 14 indicate the logarithm of core relaxation time, and logarithm of relaxation time at the half-mass radius, in $\log_{10}$ (years), finally, Col. 15 lists the central surface brightness in V magnitudes per square arcsecond

Id	log(Teff$_{HB}$)	$[Fe/H]$	Mv$_t$	Γ_{col}	ρ_0	c	R$_{GC}$	L	B	r$_c$	r$_h$	t$_{rc}$	t$_{rh}$	mu$_V$
"n0104"	3.756	-0.760	-9.420	-7.223	4.770	2.030	7.400	305.900	-44.890	0.440	2.790	8.060	9.480	14.430
"n0362"	4.079	-1.160	-8.400	-7.532	4.700	1.940	9.300	301.530	-46.250	0.190	0.810	7.760	8.920	14.880
"n1261"	4.079	-1.350	-7.810	-8.908	2.960	1.270	18.200	270.540	-52.130	0.390	0.750	8.740	9.200	17.650
"n1851"	4.097	-1.220	-8.330	-7.277	5.320	2.320	16.700	244.510	-35.040	0.060	0.520	6.980	8.850	14.150
"n1904"	4.352	-1.570	-7.860	-8.300	4.000	1.720	18.800	227.230	-29.350	0.160	0.800	7.780	9.100	16.230
"n2808"	4.568	-1.150	-9.360	-7.562	4.610	1.770	11.000	282.190	-11.250	0.260	0.760	8.280	9.110	15.170
"n3201"	4.079	-1.580	-7.490	-9.484	2.690	1.300	9.000	277.230	8.640	1.430	2.680	8.810	9.230	18.770
"n4147"	4.061	-1.830	-6.160	-9.153	3.480	1.800	21.300	252.850	77.190	0.100	0.430	7.490	8.670	17.630
"n4372"	4.114	-2.090	-7.770	-10.407	2.090	1.300	7.100	300.990	-9.880	1.750	3.900	8.900	9.590	20.510
"n4590"	4.041	-2.060	-7.350	-9.487	2.540	1.640	10.100	299.630	36.050	0.690	1.550	8.670	9.290	18.670
"n4833"	4.301	-1.790	-8.010	-9.301	3.060	1.250	6.900	303.610	-8.010	1.000	2.410	8.710	9.340	18.450
"n5024"	4.079	-1.990	-8.770	-8.741	3.040	1.780	18.800	332.960	79.760	0.360	1.110	8.790	9.690	17.390
"n5634"	4.146	-1.820	-7.750	-8.834	3.120	1.600	21.900	342.210	49.260	0.210	0.540	8.610	9.280	17.490
"n5694"	4.204	-1.860	-7.810	-8.340	4.030	1.840	29.100	331.060	30.360	0.060	0.330	7.860	9.150	16.340
"n5824"	4.380	-1.850	-8.840	-7.629	4.660	2.450	25.800	332.550	22.070	0.050	0.360	7.880	9.330	15.080
"n5904"	4.176	-1.290	-8.810	-8.096	3.910	1.830	6.200	3.860	46.800	0.420	2.110	8.260	9.530	16.050
"n5927"	3.724	-0.370	-7.800	-8.801	3.870	1.600	4.500	326.600	4.860	0.420	1.150	8.290	8.980	17.450
"n5946"	4.279	-1.380	-7.600	-9.003	4.500	2.500	7.400	327.580	4.190	0.080	0.690	7.060	8.950	17.420
"n5986"	4.415	-1.580	-8.420	-8.766	3.300	1.220	4.800	337.020	13.270	0.630	1.050	8.940	9.230	17.560
"n6093"	4.477	-1.750	-8.230	-7.693	4.760	1.950	3.800	352.670	19.460	0.150	0.650	7.730	8.860	15.190
"n6139"	4.146	-1.680	-8.360	-8.795	4.660	1.800	3.600	342.370	6.940	0.140	0.820	7.560	9.040	17.300
"n6171"	3.875	-1.040	-7.130	-9.655	3.130	1.510	3.300	3.370	23.010	0.540	2.700	8.050	9.310	18.840
"n6205"	4.505	-1.540	-8.700	-8.409	3.330	1.510	8.700	59.010	40.910	0.780	1.490	8.800	9.300	16.800
"n6218"	4.217	-1.480	-7.320	-9.295	3.230	1.390	4.500	15.720	26.310	0.720	2.160	8.100	9.020	18.170
"n6229"	4.301	-1.430	-8.070	-8.614	3.400	1.610	30.000	73.640	40.310	0.130	0.370	8.360	9.190	16.990

Id	log(Teff$_{HB}$)	$[Fe/H]$	Mv$_t$	Γ_{col}	ρ_0	c	R$_{GC}$	L	B	r$_c$	r$_h$	t$_{rc}$	t$_{rh}$	mu$_V$
"n6235"	4.114	-1.400	-6.140	-9.722	3.110	1.330	2.900	358.920	13.520	0.360	0.840	8.110	8.670	18.980
"n6266"	4.477	-1.290	-9.190	-7.742	5.140	1.700	1.700	353.580	7.320	0.180	1.230	7.640	9.190	15.350
"n6273"	4.568	-1.680	-9.080	-8.414	3.960	1.530	1.600	356.870	9.380	0.430	1.250	8.500	9.340	16.820
"n6284"	4.279	-1.320	-7.870	-8.621	4.440	2.500	6.900	358.350	9.940	0.070	0.780	7.150	9.160	16.650
"n6287"	4.114	-2.050	-7.160	-9.363	3.850	1.600	1.700	0.130	11.020	0.260	0.750	7.850	8.660	18.330
"n6293"	4.176	-1.920	-7.770	-8.483	5.220	2.500	1.400	357.620	7.830	0.050	0.910	6.240	8.910	16.180
"n6304"	3.724	-0.590	-7.320	-8.912	4.390	1.800	2.100	355.830	5.380	0.210	1.410	7.380	8.890	17.340
"n6342"	3.778	-0.650	-6.440	-9.228	4.770	2.500	1.700	4.900	9.730	0.050	0.880	6.090	8.660	17.440
"n6356"	3.756	-0.500	-8.520	-8.619	3.760	1.540	7.600	6.720	10.220	0.230	0.740	8.330	9.260	17.090
"n6362"	3.954	-0.950	-7.060	-9.698	2.220	1.100	5.300	325.550	-17.570	1.320	2.180	9.070	9.310	19.190
"n6388"	4.255	-0.600	-9.820	-7.260	5.310	1.700	4.400	345.560	-6.740	0.120	0.670	7.900	9.240	14.550
"n6397"	3.978	-1.950	-6.630	-8.528	5.680	2.500	6.000	338.170	-11.960	0.050	2.330	4.900	8.460	15.650
"n6441"	4.230	-0.530	-9.470	-7.535	5.230	1.850	3.500	353.530	-5.010	0.110	0.640	7.720	9.130	14.990
"n6453"	4.301	-1.530	-7.050	-8.998	4.720	2.500	3.300	355.720	-3.870	0.070	0.370	6.870	8.360	17.350
"n6522"	4.342	-1.440	-7.670	-8.464	5.310	2.500	0.600	1.020	-3.930	0.050	1.040	6.320	8.900	16.140
"n6540"	4.041	-1.200	-5.380	-8.857	5.920	2.500	4.400	3.290	-3.310	0.030	0.240	5.010	7.080	16.400
"n6544"	4.176	-1.560	-6.560	-9.219	5.750	1.630	5.400	5.840	-2.200	0.050	1.770	5.050	8.350	17.130
"n6569"	3.954	-1.490	-7.680	-8.917	2.920	1.200	7.000	342.140	-16.410	0.590	0.800	9.010	9.090	17.790
"n6624"	3.771	-0.420	-7.500	-8.049	5.250	2.500	1.200	2.790	-7.910	0.060	0.820	6.620	8.740	15.420
"n6637"	3.748	-0.710	-7.520	-8.540	3.810	1.390	1.600	1.720	-10.270	0.340	0.830	8.150	8.790	16.830
"n6638"	4.097	-0.990	-6.830	-8.793	4.050	1.400	1.600	7.900	-7.150	0.260	0.660	7.930	8.510	17.270
"n6642"	4.061	-1.350	-6.570	-8.661	4.720	1.990	1.600	9.810	-6.440	0.100	0.730	6.940	8.490	16.680
"n6652"	4.000	-0.960	-6.570	-8.568	4.540	1.800	2.400	1.530	-11.380	0.070	0.650	6.660	8.550	16.310
"n6681"	4.301	-1.510	-7.110	-8.155	5.410	2.500	2.100	2.850	-12.510	0.030	0.930	5.620	8.830	15.280
"n6712"	4.021	-1.010	-7.500	-9.367	3.140	0.900	3.500	25.350	-4.320	0.940	1.370	8.860	8.980	18.650
"n6717"	4.114	-1.290	-5.670	-8.665	4.650	2.070	2.300	12.880	-10.900	0.940	1.370	6.610	8.260	16.480
"n6723"	4.130	-1.120	-7.860	-9.002	2.810	1.050	2.600	0.070	-17.300	0.940	1.610	8.990	9.300	17.920
"n6760"	3.740	-0.520	-7.860	-9.564	3.840	1.590	4.800	36.110	-3.920	0.330	2.180	7.940	9.390	18.790
"n6838"	3.763	-0.730	-5.560	-9.981	3.050	1.150	6.700	56.740	-4.560	0.630	1.650	7.640	8.410	19.220
"n6864"	4.176	-1.320	-8.350	-7.866	4.510	1.880	12.800	20.300	-25.750	0.100	0.470	7.850	9.080	15.550
"n6934"	4.130	-1.540	-7.650	-8.732	3.370	1.530	14.300	52.100	-18.890	0.250	0.600	8.430	9.070	17.260
"n6981"	4.000	-1.400	-7.040	-9.566	2.350	1.230	12.900	35.160	-32.680	0.540	0.880	8.930	9.200	18.900
"n7078"	4.477	-2.250	-9.170	-7.290	5.380	2.500	10.400	65.010	-27.310	0.070	1.060	7.020	9.350	14.210
"n7089"	4.477	-1.620	-9.020	-7.961	3.900	1.800	10.400	53.380	-35.780	0.340	0.930	8.540	9.320	15.920
"n7099"	4.079	-2.120	-7.430	-8.040	5.040	2.500	7.100	27.180	-46.830	0.060	1.150	6.380	8.950	15.280

	$\log(\mathrm{Teff}_{HB})$	$[Fe/H]$	Mv_t	Γ_{col}	ρ_0	c	R_{GC}	l	b	r_c	r_h	t_{rc}	t_{rh}	mu_V
$\log(\mathrm{Teff}_{HB})$	1.00	-0.57	-0.44	0.39	0.16	0.14	0.19	0.24	0.09	-0.10	-0.23	0.06	0.18	-0.34
$[Fe/H]$	-0.57	1.00	0.01	0.04	0.09	-0.16	-0.36	-0.22	-0.21	-0.05	-0.02	0.02	-0.12	-0.02
Mv_t	-0.44	0.01	1.00	-0.64	-0.08	0.01	-0.19	-0.34	0.04	0.07	0.01	-0.42	-0.73	0.47
Γ_{col}	0.39	0.04	-0.64	1.00	0.66	0.50	0.15	0.13	-0.24	-0.55	-0.41	-0.21	0.10	-0.97
ρ_0	0.16	0.09	-0.08	0.66	1.00	0.80	-0.23	-0.05	-0.23	-0.73	-0.36	-0.83	-0.47	-0.80
c	0.14	-0.16	0.01	0.50	0.79	1.00	-0.01	0.04	-0.06	-0.65	-0.32	-0.77	-0.33	-0.65
R_{GC}	0.19	-0.36	-0.19	0.15	-0.23	-0.01	1.00	0.22	0.25	-0.12	-0.28	0.26	0.29	-0.10
l	0.24	-0.22	-0.34	0.13	-0.05	0.04	0.22	1.00	0.15	0.04	-0.01	0.21	0.27	-0.07
b	0.09	-0.21	0.04	-0.24	-0.23	-0.06	0.25	0.15	1.00	-0.01	-0.04	0.14	0.12	0.25
r_c	-0.10	-0.05	0.07	-0.55	-0.73	-0.65	-0.12	0.04	-0.01	1.00	0.71	0.59	0.33	0.64
r_h	-0.23	-0.02	0.01	-0.41	-0.36	-0.32	-0.28	-0.01	-0.04	0.71	1.00	0.19	0.34	0.42
t_{rc}	0.06	0.02	-0.42	-0.21	-0.83	-0.77	0.26	0.21	0.14	0.59	0.19	1.00	0.70	0.43
t_{rh}	0.18	-0.12	-0.73	0.10	-0.47	-0.33	0.29	0.27	0.12	0.33	0.34	0.70	1.00	0.08
mu_V	-0.34	-0.02	0.47	-0.97	-0.80	-0.65	-0.10	-0.07	0.25	0.64	0.42	0.43	0.08	1.00

TABLE 6.8— Pearson linear regression correlation coefficients, **r**, for the 14 quantities in table 6.7.

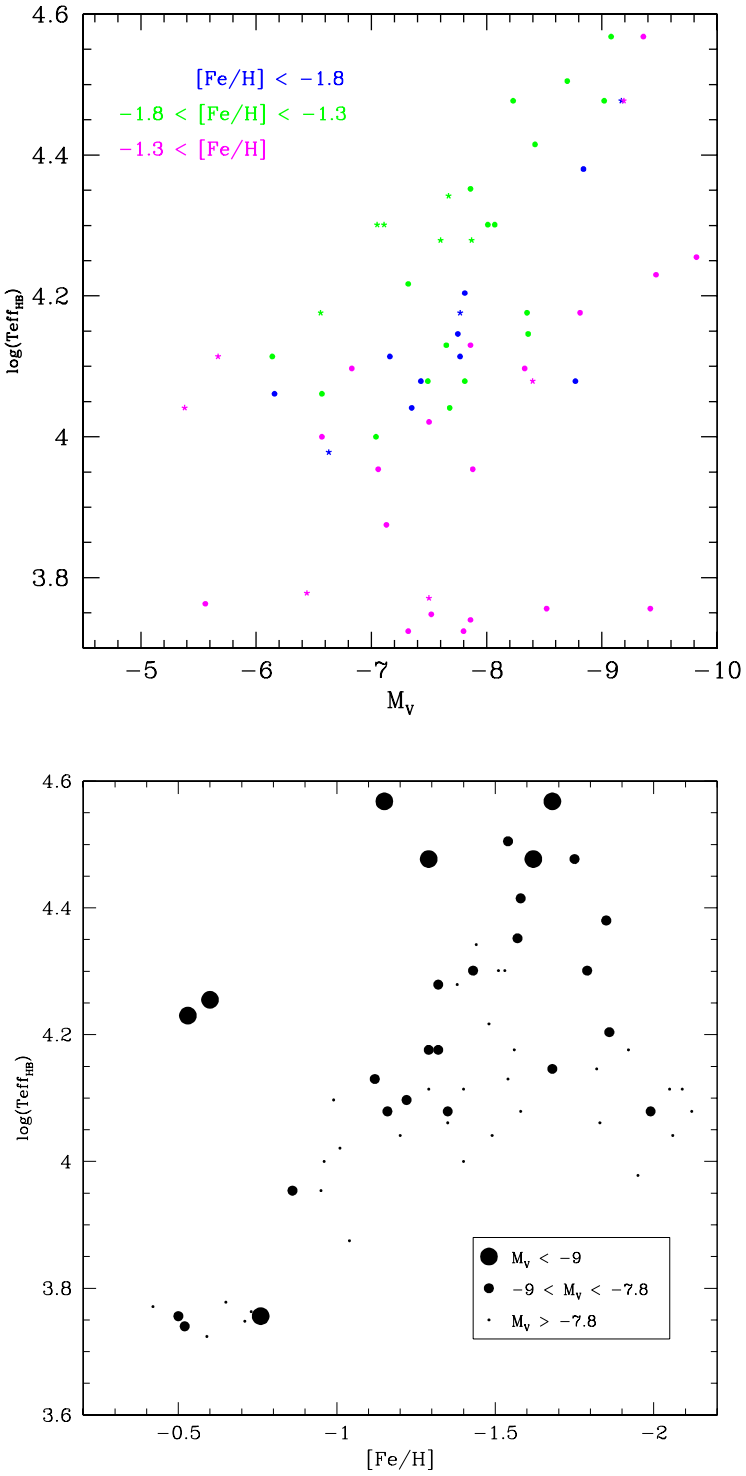


FIGURE 6.9— Upper panel: correlation of log(Teff$_{HB}$) with absolute V magnitude, for 3 different metallicity intervals. The highest correlation is observed for intermediate metallicity clusters (green dots) and for the more extended HBs. Core collapsed clusters are plotted as asterisks, and follow the same trend as non-core collapsed clusters. Bottom panel: HB morphology-metallicity correlation with different symbol sizes depending on total luminosity, M_V. Note the better correlation of clusters of intermediate luminosity. The smallest clusters (M_V > -7.8) do not reach the bluest HB morphologies, and they all have log(Teff$_{HB}$) < 4.35.

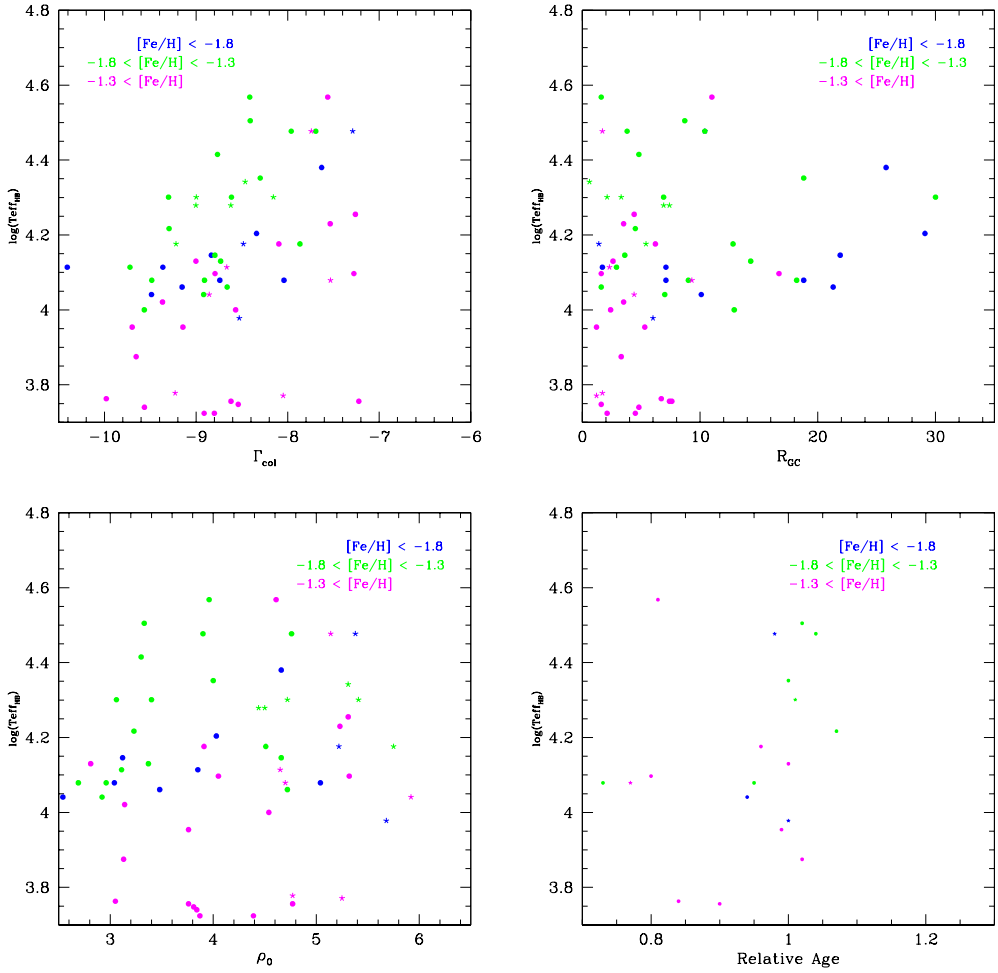


FIGURE 6.10— Correlation of $\log(\mathrm{Teff}_{HB})$ with (from upper left to bottom right) collisional parameter, central density, Galactocentric distance and age.

Cluster	log(Teff$_{HB}$)	Age	Cluster	log(Teff$_{HB}$)	Age
n0104	3.756	0.90	n6171	3.875	1.02
n0362	4.079	0.77	n6205	4.505	1.02
n1261	4.079	0.73	n6218	4.217	1.07
n1851	4.097	0.80	n6362	3.954	0.99
n1904	4.352	1.00	n6397	3.978	1.00
n2808	4.568	0.81	n6681	4.301	1.01
n3201	4.079	0.95	n6723	4.130	1.00
n4590	4.041	0.94	n6838	3.763	0.84
n5904	4.176	0.96	n7078	4.477	0.98
n6093	4.477	1.04			

TABLE 6.9— Relative ages from Rosenberg et al. (1999) for the subsample of 19 clusters we have in common.

	log(Teff$_{HB}$)	$[Fe/H]$	M$_V$	Γ_{col}	r$_h$	c	R$_{GC}$	B
log(Teff$_{HB}$)	1.00	-0.57	-0.44	0.39	-0.23	0.14	0.19	0.09
$[Fe/H]$	-0.57	1.00	0.01	0.04	-0.02	-0.16	-0.36	-0.21
M$_V$	-0.44	0.01	1.00	-0.64	0.01	0.01	-0.19	0.04
Γ_{col}	0.39	0.04	-0.64	1.00	-0.41	0.50	0.15	-0.24
r$_h$	-0.23	-0.02	0.01	-0.41	1.00	-0.32	-0.28	-0.04
c	0.14	-0.16	0.01	0.50	-0.32	1.00	-0.01	-0.06
R$_g c$	0.19	-0.36	-0.19	0.15	-0.28	-0.01	1.00	0.25
B	0.09	-0.21	0.04	-0.24	-0.04	-0.06	0.25	1.00

TABLE 6.10— Pearson linear regression correlation coefficients, **r**, for the 8 independent quantities.

i	e$_i$	V$_i$	C$_i$
1	2.49	31.2	31.2
2	1.66	20.7	51.9
3	1.21	15.1	67.0
4	0.99	12.4	79.4
5	0.73	9.1	88.5
6	0.62	7.7	96.2
7	0.18	2.2	98.4
8	0.13	1.6	100.0

TABLE 6.11— Eigenvalues (e$_i$), fractional (V$_i$) and cumulative (C$_i$) contributions to the total sample variance, in percent, for the obtained PCA solution for the set of 8 input independent parameters..

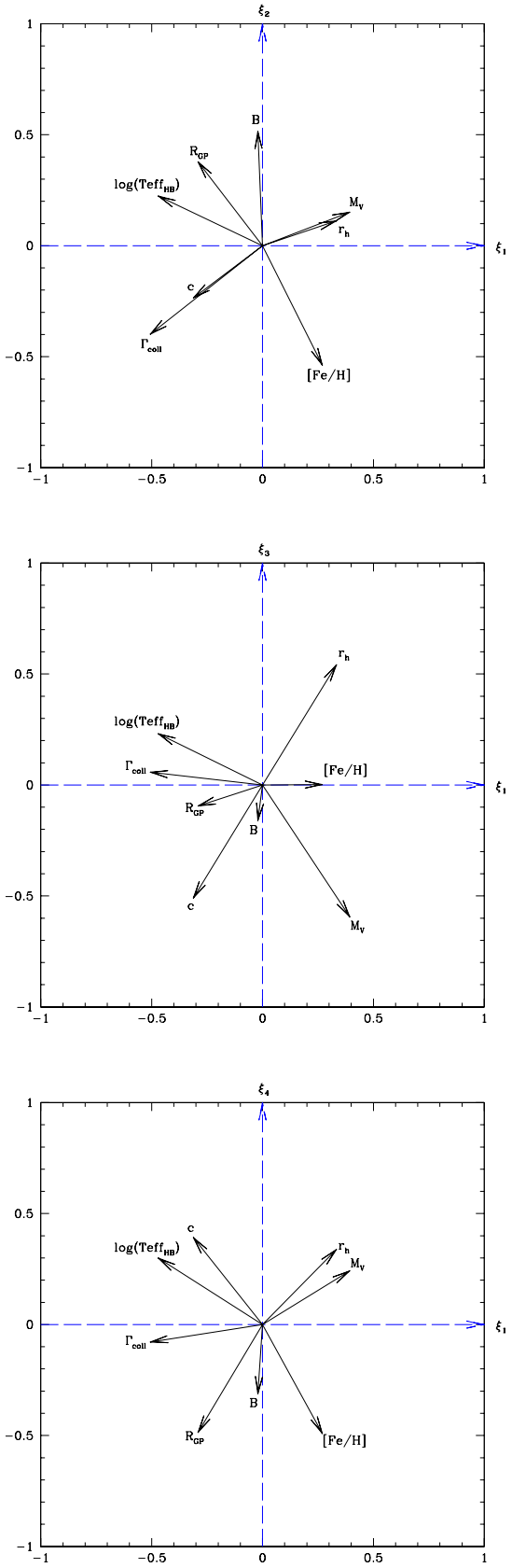


FIGURE 6.11— Projections of the input axes to the principal planes given by the eigenvectors (ξ_1, ξ_2), (ξ_1, ξ_3) and (ξ_1, ξ_4).

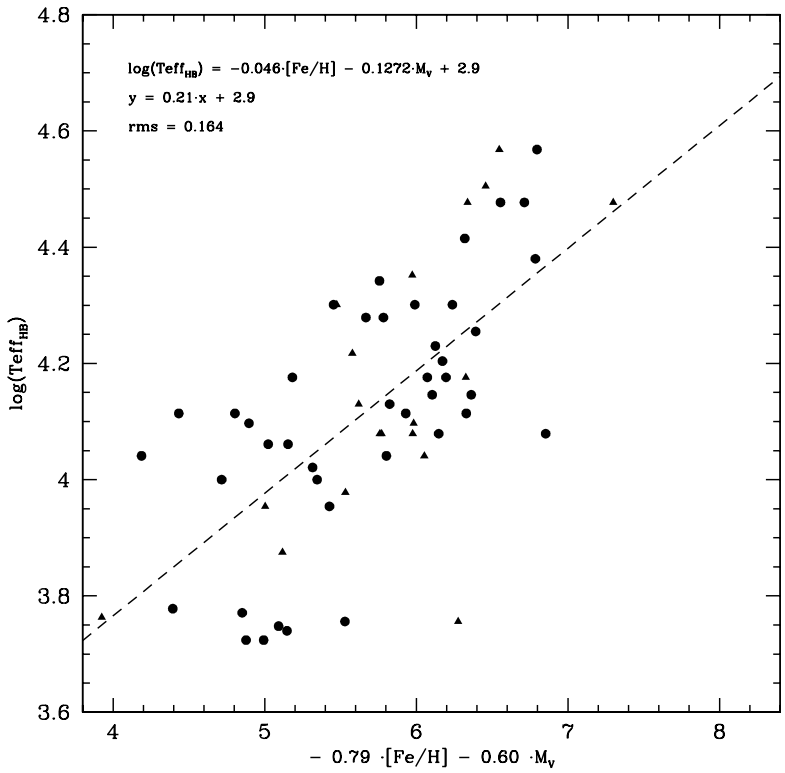


FIGURE 6.12— Bivariate correlation involving the variables log(Teff$_{HB}$), $[Fe/H]$ and M_V. Triangles are clusters in common with Rosenberg et al. (1999).

i	e_i	V_i	C_i
1	1.72	57.3	57.3
2	0.99	33.0	90.3
3	0.29	9.7	100.0

TABLE 6.12— PCA solutions for a subsample of 3 parameters : log(Teff$_{HB}$), $[Fe/H]$ and M_V.

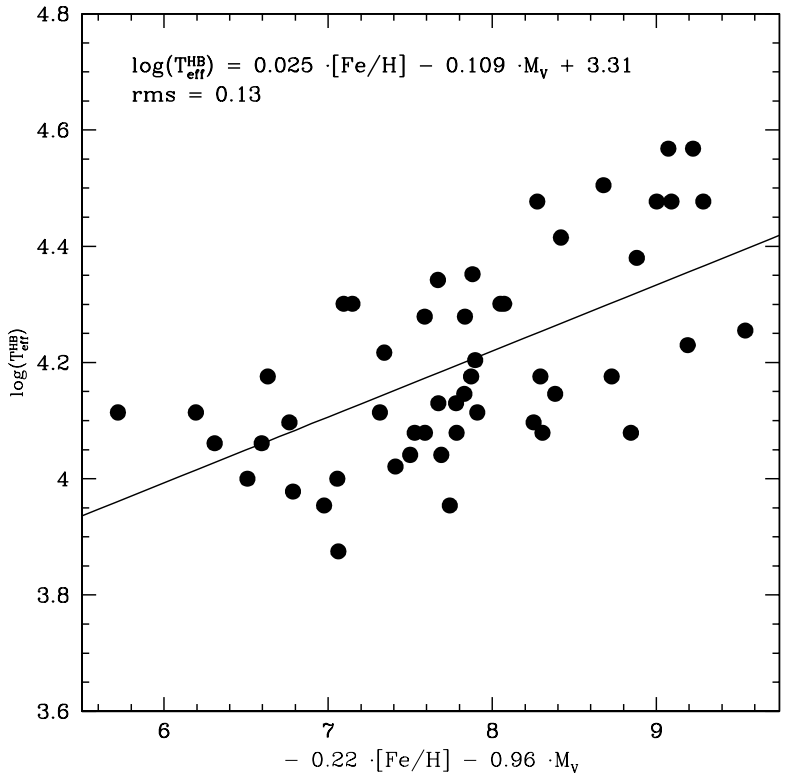


FIGURE 6.13— Bivariate correlation of HB morphology with optimized combinations of $[Fe/H]$ and M_V for clusters with $\log(\mathrm{Teff}_{HB}) > 3.8$.

i	e_i	V_i	C_i
1	1.86	46.6	46.6
2	1.27	31.7	78.3
3	0.56	14.1	92.4
4	0.31	7.6	100.0

TABLE 6.13— PCA solutions for the second subsample of 4 parameters : $\log(\mathrm{Teff}_{HB})$, $[Fe/H]$, M_V and Age.

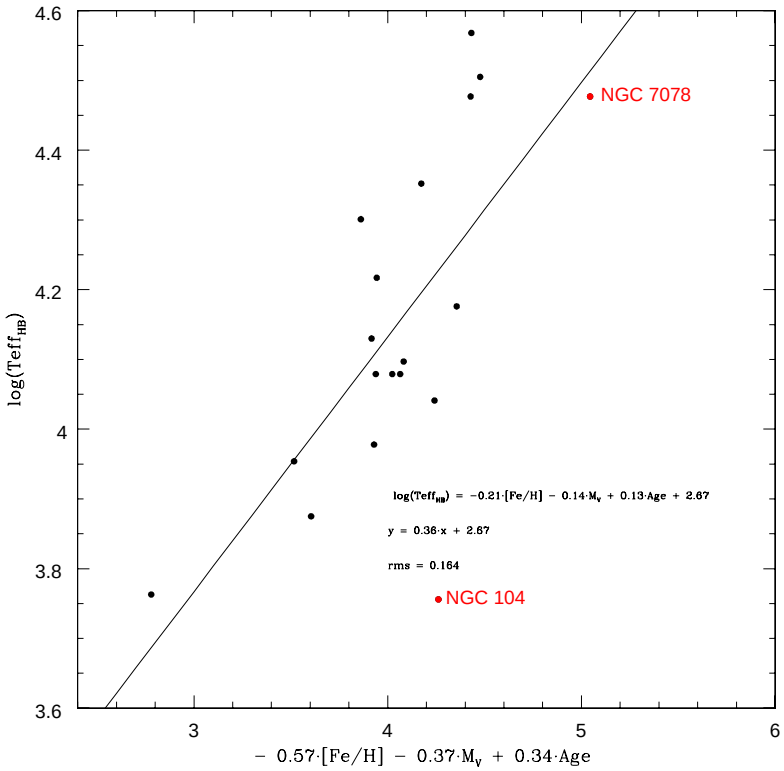


FIGURE 6.14— Trivariate correlations of HB morphology with optimized combinations of $[Fe/H]$, M_V and Age for a subsample of 19 clusters in common with Rosenberg et al. (1999).

i	e_i	V_i	C_i
1	1.67	55.7	55.7
2	1.04	34.7	90.4
3	0.29	9.6	100.0

TABLE 6.14— PCA solutions for a subsample of 3 parameters : $\log(\mathrm{Teff}_{HB})$, $[Fe/H]$ and Γ_{col}.

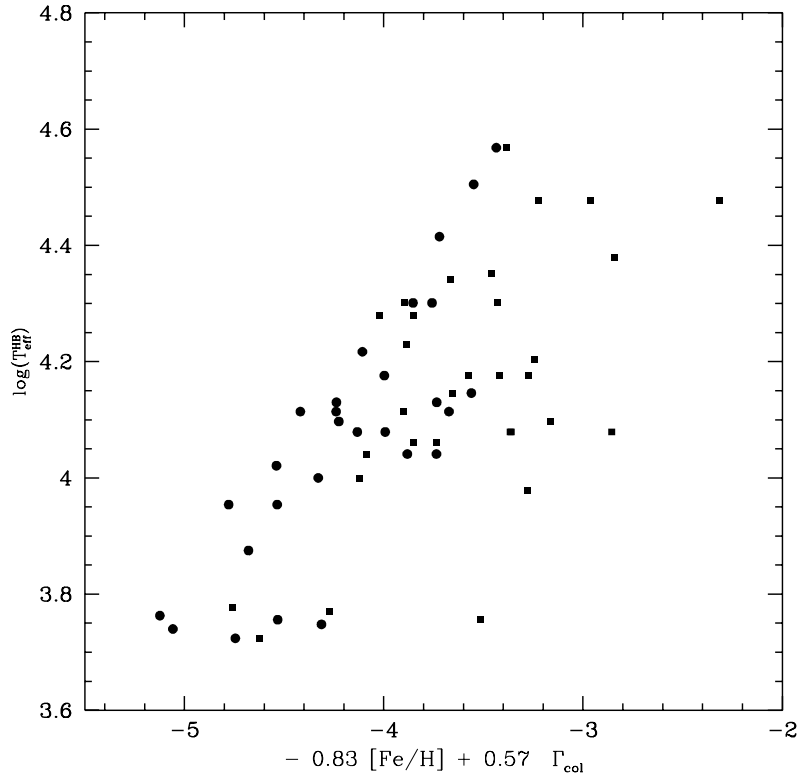


FIGURE 6.15— Bivariate correlation involving the variables log(Teff$_{HB}$), $[Fe/H]$ and M_V. Squares are clusters in with central concentration c > 1.7.

i	e_i	V_i	C_i
1	2.07	51.7	51.7
2	1.29	32.2	83.9
3	0.36	9.0	92.9
4	0.28	7.1	100.0

TABLE 6.15— PCA solutions for the first subsample of 4 parameters : log(Teff$_{HB}$), $[Fe/H]$, M_V and Γ_{col}.

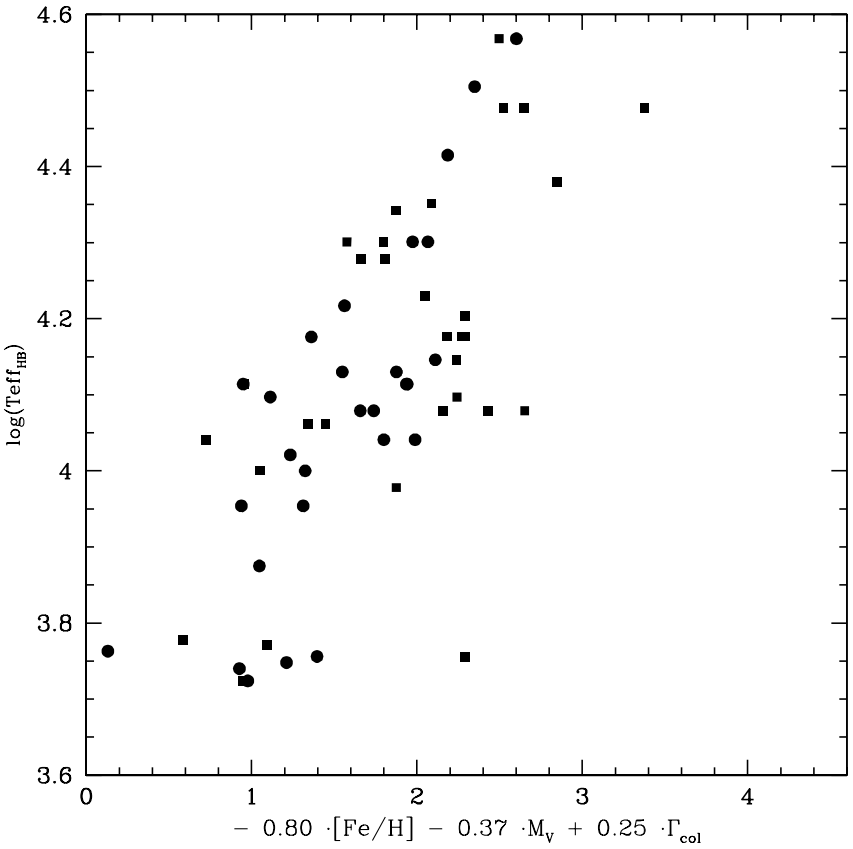


FIGURE 6.16— Trivariate correlation of HB morphology with optimized combinations of $[Fe/H]$, M_V and Γ_{col}. The spread for clusters with redder HBs decreases with respect to the bivariate correlation. Clusters with central concentration c > 1.7 are plotted as squares.

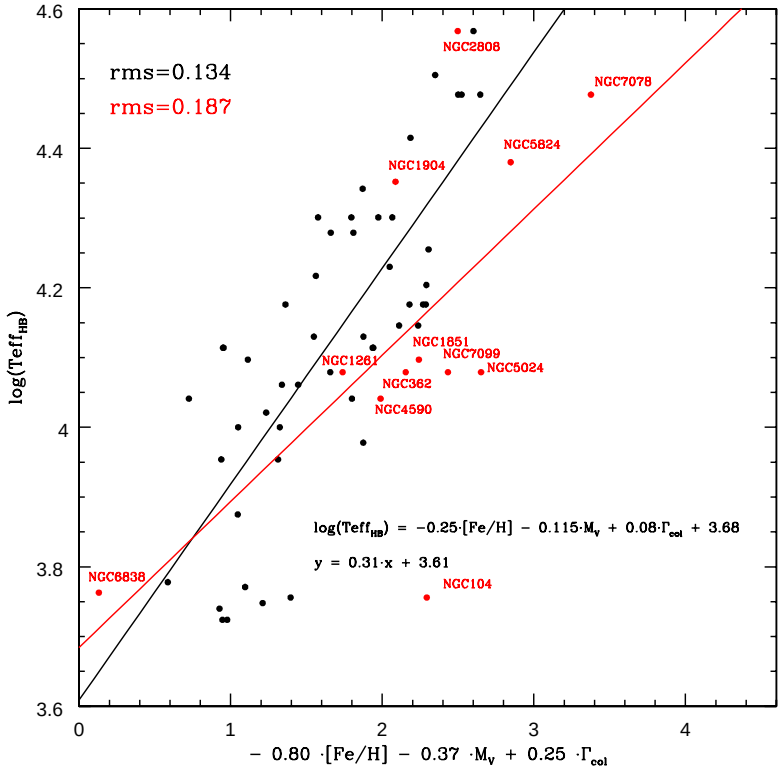


FIGURE 6.17— Similar to Figure 6.16 but separating the clusters with ages younger than the mean or clusters suspected to be related to satellite dwarf galaxy streams (red dots) and "normal" clusters (balck dots). A least square fit and their rms value are also indicated for each of the cluster subsets.

7

A new feature along the BT of NGC6752.

In order to identify the possible targets for the spectroscopic projects, we have reduced wide field images from the ESO WFI@2.2 camera of blue tail clusters. For one of them, NGC 6752, we had exceptionally high quality UBV images. The careful photometric analysis we have performed has brought us to the discovery which is discussed in the present Chapter, already published in an ApJ Letter (Momany et al. 2002). NGC 6752 is a nearby ($(m-M)_\circ = 13.05$, Renzini et al. 1996], low reddening [$E_{B-V} = 0.04$, Penny & Dickens 1986), intermediate metallicity ([Fe/H]$= -1.64$) cluster, with a complex HB extending to $T_{\rm e} \sim 32,000$K.

7.1 Observations and data reductions.

Images of NGC 6752 through U, B, and V filters were taken on July 25-26 2000, with the Wide-Field Imager (WFI) at the 2.2 m ESO-MPI telescope at La Silla, Chile. The WFI camera consists of eight 2048×4096 EEV-CCDs, with a total field of view of 34×33 arcmin^2. The exposure times (30s and 150s in U, 5s and 10s in B, and 3s and 7s in V) were chosen in order to sample both the bright RGB and the faint MS stars . Weather conditions were photometric, with good seeing (below 0.8 for all images). Basic reductions of the CCD mosaic was performed using the IRAF package MSCRED (Valdes 1998), while stellar photometry was performed using the DAOPHOT and ALLFRAME programs (Stetson 1994). Finally, instrumental magnitudes were calibrated to the UBV standard system on a chip to chip basis using a set of standard stars from Landolt (1992).

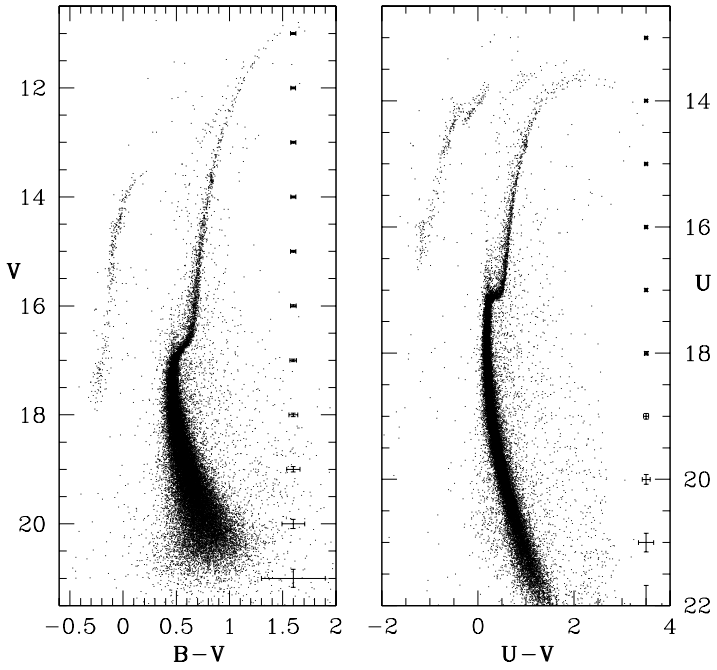


FIGURE 7.1— The (V, $B-V$) and (U, $U-V$) CMDs for stars with $0.3 < R < 13.9$, where R is the projected distance from the cluster center. Photometric errors, as calculated by ALLFRAME, are shown on the right side of the two CMDs.

7.2 The Colour-Magnitude Diagrams.

Figure 7.1 shows the (V, $B-V$) and (U, $U-V$) CMDs for stars with $0.3< R <13.9$, where R is the projected distance from the cluster center. All the sequences of the CMD, from below the turn-off up to the RGB tip are well defined and populated. The CMD shows an extended HB, which spans more than 4.5 magnitudes in V, and extends down to $V = 17.9$, i.e. ~ 1.5 magnitudes below the TO. The HB does not show any new feature in the V, $B-V$ plane (Fig. 7.1, *left panel*), apart from the gap at $B-V$=0 and $V = 14.2$ (Caloi 1999), and a sudden increase in the photometric dispersion below $V = 17$ which cannot be explained in terms of photometric errors alone. The HB itself is not homogeneously populated, with a clear underabundance of stars in the interval $17.0 \leq V \leq 15.7$.

It is surely more instructive to look at the U, $U-V$ CMD (Fig. 7.1, *right panel*; see also the zoomed version in Fig. 7.2, *upper panel*). In this plane, the distribution of HB stars is remarkably discontinuous. In particular: (i) We note

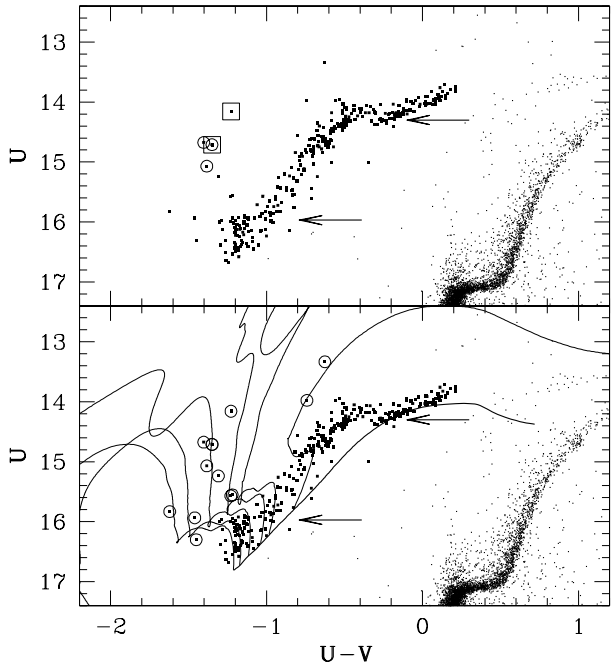


FIGURE 7.2— Upper panel shows a close look at the "jumps" in the HB of NGC 6752, indicated by arrows. The four open circles are post-HB stars from Moehler et al. (1998), while the open rectangle shows the star UIT1 of L96. The lower panel shows the same diagram with a canonical $Z = 0.0006$ ZAHB model (thick line). Thin lines are HB models for stars with masses M= 0.504, 0.505, 0.510, 0.515 0.520 and M= 0.540$M_{\odot}$. Open circles are the 13 post-HB candidates.

a *jump* in the stellar distribution at $U - V \sim -0.30$. This jump is analogous to the *jump* identified by B00 in the same bands in NGC 2808, and corresponds to the G99 jump. (ii) Most interestingly, at $U \sim 15.9$, $U - V \sim -1.0$ there is a "second jump" in the distribution of the stars along the HB. This feature has never been identified, though, a posteriori, a similar jump can be seen in the CMDs of M13 and NGC 6752 in G99, and, to a lesser extent, in the CMD of NGC 2808 of B00. The larger photometric dispersion and the smaller sample of G99 and B00 partly mask this feature in their CMDs. (iii) There are 13 stars significantly bluer and brighter than the bulk of HB stars (plotted as open circles in Fig. 7.2, *lower panel*). Most of them are the progeny of EHB stars.

Before turning our attention to the newly identified "second jump", we briefly comment on the post-HB candidates.

The evolution of extreme HB stars and their progeny have received spe-

cial attention from the community, since they are crucial to understanding the Spectral Energy Distribution (SED) of hot stellar populations in metal-poor and metal-rich stellar systems. In particular, we are interested in testing whether predicted evolutionary lifetimes are supported by empirical data since they have a significant impact on the SED of hot stellar populations. Previous investigation of NGC 6752 from UIT images (L96) showed a deficiency of a factor of 3 in the observed number of post-EHB stars with respect to the theoretical predictions. In Fig. 7.2 there are 13 post-HB candidates. Four stars (*circles* in Fig. 7.2, *upper panel*) have been classified as post-EHB (AGB-manquè) stars by Moehler, Landsman, & Napiwotzki (1998). Note that the double open circles (stars B852 and B4380 in Moehler et al. 1998) share almost identical magnitudes and colors in our catalog. A fifth post-HB candidate has been proposed by L96 (UIT1 in L96, *open square* in Fig. 7.2), and we confirm their result.

Figure 7.2 (*lower panel*) shows the comparison in the $U, U-V$ plane between the observed CMD and He-burning evolutionary models. The thick line shows the Zero-Age-Horizontal-Branch (ZAHB), while the thin lines display the off ZAHB evolution of selected AGB-manquè and Post-Early-AGB structures (Greggio & Renzini 1990). Evolutionary computations have been performed by adopting an initial He content of Y=0.23 and a metallicity Z=0.0006. The ZAHB models were computed by adopting the He core mass and He surface abundance given by an RGB progenitor with mass equal to $0.8M_{\odot}$. These models were constructed by neglecting atomic diffusion and radiative levitation (see Cassisi & Salaris 1997 for more details). The transformation to the observational plane was done by adopting the bolometric corrections and the color-temperature relations by Castelli, Gratton, & Kurucz (1997). The comparison of the observed CMD with the set of models in Fig. 7.2 allows us to isolate the HB stars that, after the end of the central He-burning phase, will eventually evolve into AGB-manquè structures. The M= $0.520M_{\odot}$ model is the coolest model able to produce AGB-manquè stars. In Fig. 7.2, there are 84 HB stars hotter than this track; only 11 of the 13 post-HB stars can be classified as AGB-manquè. The ratio between the two populations is 0.13, and it is consistent, within the uncertainties, with the predicted value of ~ 0.09, thus solving the discrepancy pointed out by L96. The 11 post-HB stars have been inspected by eye, one by one. Apart from one case, there are no obvious blends or CCD artifacts that could cause large photometric errors. We believe that the much higher resolution of our data can explain the difference in the number of post-HB stars identified in the two works.

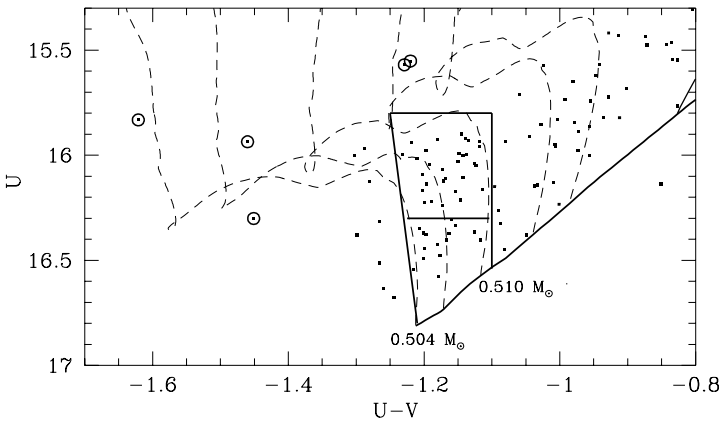


FIGURE 7.3— As in Fig. 7.2, but zooming around the EHB.

7.3 The second jump.

The most intriguing feature in the CMDs of Figs. 7.1 and 7.2 is the presence of the "second jump" around $U - V \approx -1.0$. The two arrows in Fig. 7.2 mark the position of the two jumps along the HB blue tail. The comparison with the models in Fig. 7.2 shows that the two jumps are located at $T_{\rm e} \sim 11,600$ and $T_{\rm e} \sim 23,000$K. The cooler part of the CMD is well reproduced by the models, but HB stars hotter than $T_{\rm e} > 11,600$K are systematically brighter than predicted by ZAHB models. However, the observed HB stars are steadily approaching the theoretical ZAHB when moving from $T_{\rm e} \sim 11,600$K to $T_{\rm e} \sim 23,000$K, where the "second jump" suddenly appears.

Figure 7.2 shows that the HB extends to $U = 16.8$, corresponding to a temperature $T_{\rm e} \sim 32,000$K. We can therefore exclude the possibility that the "second jump" is related to the presence of late helium flashers with envelope mixing (B01), as these stars are expected to be hotter than $T_{\rm e} \sim 32,000$K. Another possible explanation for the origin of the "second jump" could be related to the presence of binaries in the EHB stars of NGC 6752 (Peterson et al. 2002). Unresolved, equal mass binaries would appear brighter than single stars with the same temperature and luminosity, and this would mimic the observed "second jump". However, the "second jump" in the HB would imply a rather *ad hoc* binary distribution along the HB.

Figures 7.2 and 7.3 show that the evolutionary path of hot HB stars is almost vertical in the U, $U-V$ plane, while the ZAHB is not. It is interesting to investigate whether the "second jump" can be an artifact of post-HB evolution

in the photometric plane of Figs. 7.2 and 3. To this purpose, we have calculated the post-ZAHB evolutionary times for stars hotter than $T_{\rm e} = 23,000$K. We find that He-burning stars evolving from the ZAHB should spend 40% of their time at magnitudes $U > 16.3$, and about 50% of their time at $15.8 \leq U \leq 16.3$. The ratio between these two lifetimes is 0.8. On the other hand, we count 15 stars in the *lower box* of Fig. 7.3, and 30 stars in the *upper box*, to which we should add 3 more stars on the blue side of the *upper box*, that are very likely objects which started their post-ZAHB evolution from the *lower box*. The observed ratio is 0.46 ± 0.20. Therefore, the stellar distribution in the hottest portion of the HB in NGC 6752 can not be due *only* to the peculiar morphology of evolutionary tracks in the $U, U-V$ plane. Moreover, if we interpret all the stars in the two boxes of Fig. 7.3 simply as HB stars evolving from the ZAHB as expected from the canonical models, we are faced with a further anomaly: a sharp peak in the distribution of stellar masses. According to the models, all the stars with $T_{\rm e} > 23,000$K have a mass of $0.505 M_{\odot}$, with a dispersion of only $0.003 M_{\odot}$. It is difficult to understand the origin of such a peculiar distribution along the HB.

Since the stellar distribution across the hotter "second jump" resembles the G99's jump, one might wonder whether both features share similar physical origins. The occurrence of the G99's jump was explained as the aftermath of radiative levitation that causes a substantial increase in the metal content of the outermost layers. This finding confirms earlier results by Glaspey et al. (1989) in NGC 6752, and later investigations by Behr et al. (1999, 2000) for a few other clusters. Both groups find that hot HB stars present He depletion and a remarkable over-abundances of heavy elements (Fe, Ti, N, P, etc.), when compared with the cluster abundances. In particular, in NGC 6752, Glaspey et al. (1989) found an over-abundance of iron by a factor of 50 (and He depletion) in the star CL1083 ($T_{\rm e} = 16,000$K). Instead, no abundance anomalies were found in the star CL1007 with $T_{\rm e} = 10,000$K. The results by Moehler et al. (1997), who find strong He underabundances also for stars with $T_{\rm e} > 23,000$K, suggests that diffusion is present in the hottest stars, and might be related to the "second jump" anomaly.

Radiative levitation and diffusion are possible after the disappearance of the envelope convective layers located across the H and HeI ionization regions, at $T_{\rm e} \sim 10,000 - 11,000$K (Caloi 1999, Sweigart 2000). For $T_{\rm e} > 11,000$K, radiative levitation takes place in a thin radiative layer located between the surface and the second He ionization region (HeII). When moving toward hotter effective temperatures the radiative layer becomes thinner, since the increase in the effective temperature causes a systematic shift of the HeII region toward the surface (Sweigart 2000). Canonical stellar models predict that the

HeII convective region approaches the stellar surface in the ZAHB structures at $T_{\rm e} \sim 23,000$K. In addition, as expected on theoretical grounds (Vink & Cassisi 2002), the mass loss efficiency increases with effective temperature. Mass loss works as a competing process to diffusion (Michaud & Charland 1986), and indeed it decreases the efficiency of radiative levitation in producing large chemical over-abundances of heavy elements. As a result, radiative levitation is less and less effective in the effective temperature range $T_{\rm e} \sim 11,000-23,000$K, and the stars should steadily approach the canonical ZAHB luminosity, when moving toward hotter HB stars. This evidence is supported by the observed HBs (Fig. 7.2). At the same time, the over-abundance of heavy elements should decrease as well. Unfortunately, we still lack of observational data to support the latter hypothesis. For stars with $T_{\rm e} > 23,000$K, as a consequence of the larger surface gravity and longer central He-burning lifetime, one expects that the atomic diffusion becomes more and more efficient in decreasing the envelope He abundance, implying the quenching of the HeII convection. At the same time, the large increase in the effective temperature should enhance the capability of radiative levitation in producing a chemical separation in the stellar envelope. According to this working scenario, HB stars with $22,000 \leq T_{\rm e} \leq 24,000$K should present a change in the surface chemical composition in comparison to hotter and cooler structures. It is rather tempting to associate the "second jump" identified in this paper with this discontinuity in the chemical composition. It is possibly the combination of this discontinuity and the off ZAHB evolutionary path and timescales which produces the observed peculiar morphology of the hottest part of the HB in NGC 6752.

Even though this scenario is quite attractive, the results of Michaud, Vauclair & Vauclair (1983, M83) could somewhat challenge it. By modeling the change in the chemical stratification caused by atomic diffusion and radiative levitation, they found that the He abundance in the envelope of hot HB stars sharply decreases in a very short time scale (see their Figs. 7.1 and 7.2). This effect is due to the high efficiency of atomic diffusion. In particular, their computations suggest that for structures located at $T_{\rm e} \sim 20,000$K, the HeII convective zone should disappear after $\approx 10^4$yrs. If these predictions are correct, then our proposed scenario is ruled out. However, in the same investigation, M83 have qualitatively estimated also the effects of turbulent motions, and found that if the convective transport is particularly efficient it could limit the efficiency of atomic diffusion. This means that He, and in turn the convective region in the envelope, should not rapidly disappear in extreme HB structures. This evidence is further supported by the fact that HB models constructed by M83 which neglect both the mass loss (see Unglaub & Bues 2001 for a detailed discussion), and the effects of turbulence, predict He abundances lower than observed.

In order to estimate the minimum He abundance needed in the stellar envelope of hot HB stars to have a HeII convection zone, we have computed several models for different assumptions on the external abundance of He. We have found that for a He abundance of $Y \approx 0.1$, the envelope of extreme HB structures still presents a very thin convective layer across the HeII region. On the other hand, the spectroscopic investigation by Moehler et al. (2000) suggests that the He content in the EHB stars of NGC 6752 with $17,000 < T_{\rm e} < 22,000$K is lower: $0.01 < Y < 0.08$, with an uncertainty of ~ 0.02. However, to reach firm conclusions concerning the cut-off in the He abundance for the occurrence of a convective region one needs a new generation of evolutionary models that consistently account for all physical mechanism(s) affecting the chemical stratification of HB stars.

Nevertheless, if the suggested scenario is actually at work, the presence of a convective region (very close to to the surface in a narrow mass range in the EHB) would imply that the stars across the "second jump", when compared with the stars across the first jump, should show larger macroturbulence velocities and a larger spread in chemical abundances. This qualitative scenario is somehow supported by spectroscopic measurements of field sdB and sdO stars. As a matter of fact, there is evidence that He abundance steadily increases when moving from sdB to sdO. In these stars it has also been observed a strong depletion of silicon and a mild underabundance of Carbon (Lamontagne, Wesemael, & Fontaine 1987), while other elements are enriched even with respect to solar composition (Heber et al. 2002). Accurate abundance measurements of He and heavy elements along the hot portion of the HB in GCs, such as NGC 6752, could be crucial to constrain the theoretical framework. At the same time, new optical and UV spectroscopic data are needed to ascertain the occurrence and efficiency of mass-loss among EHB stars (Heber et al. 2002).

Part IV

Conclusions and Future Work.

8

Conclusions and Future Work.

8.1 Conclusions.

In this thesis, nature of hot horizontal branch stars in Galactic globular clusters has been explored, both investigating their physical characteristics (rotation, chemical abundances, luminosity...) and trying to disentangle their origin, liked to the second parameter problem. To this purpose, we have performed high resolution spectroscopy of 61 HB stars in 4 different clusters, and we have examine the HB temperature extension of 63 globulars and its dependence on cluster parameters, via their (V, B,V) colour-magnitude diagrams and the multidimensional analysis technique.

The main conclusions of this work can be summarized as follows:

1) *Fast rotation is a fairly common feature among horizontal branch stars.* Our study, which has almost doubled the number of previously observed globular cluster hot HB stars, has revealed the existence of fast HB rotators in M79 and confirmed their presence in M15. The reason why these low mass stars, with slow rotating progenitors like the Sun, are spinning so fast is not already clear. Maybe angular momentum from the stellar core, developed during the RGB phase as a consequence of core contraction and envelope expansion, is transferred to the external layers in the HB (Sills & Pinsonneault scenario). Or maybe HB stars re-acquire angular momentum, for example, by close tidal encounters in the high density environments of globular clusters or swallowing substellar objects. None of these possibilities, however, gives a conclusive answer to the problem.

2) *There seems to be a discontinuity in the rotation rate at the level of the*

luminosity jump, associated with the onset of diffusive processes in the stellar atmosphere, which cause overabundances of metals and helium depletion.. Stars with $T_{eff} < 11\ 000$ K show a range of $v\sin i$ values (the projected rotational velocity) up to 30 km/s. However, all the stars with $T_{eff} > 11\ 000$ K are slow rotators, with $v\sin i < 12$ km/s. The origin of this discontinuity could be the removal of angular momentum due to the enhanced mass loss expected for $T_{eff} > 11000$ K, or, if angular momentum is percolating from the core, a prevention of this transfer by a gradient in molecular weight.

3) *Apparently, the abundance of fast rotators is not the same in all clusters, although this can be an effect of the observational statistics.* In fact, the two target clusters for which no fast rotator has been found, M80 and NGC 2808 are also those with the lower number of stars observed at $T_{eff} < 11\ 000$ K.

4) *Radiative levitation of metals and helium depletion is detected for stars hotter than $\sim$ 11 000 K in M79, in coincidence with the Grundahl et al. luminosity jump.* Abundance of iron, titanium, chromium, and other metal species are enhanced up to supersolar values, while helium abundance appears below the expected solar He/H ratio. This measurements are very similar to those previously found in M13 by Behr et al. (1999), although slightly higher abundances in M79 than in M13 for some metal species and for helium could also be compatible with our results.

5) *Total mass and stellar collisions seem to influence the observed horizontal branch morphologies of Galactic globular clusters, with effects larger than those of age.* This dependence, combined with that of metallicity, the first parameter, can explain probably the major part of the HB extensions of the 63 clusters evaluated. More massive clusters (i.e. more luminous) tend to have more extended horizontal branches. Clusters with a higher collisional parameter tend also to have more extended HBs. On the other hand, although M_V and Γ_{col} are partially correlated, they are not completely equivalent.

6) Finally, we report on the detection of a new feature in the complex structure of the horizontal branch of the NGC 6752: a discontinuity ("jump") in the U versus (U-V)-plane for effective temperatures hotter than 23,000 K. This feature might be due to the combination of postzero-age HB evolution and diffusion effects.

Part V

Appendix : Abundance measurements

$\lambda(\AA)$	E.P.	log gf	log C6	log EW (m$\AA$)	log ϵ	σ_Σ
M79-0209						
MgII						
4481.34	8.86	0.57	-33.89	102.1	6.51	0.31
SiII						
3853.67	6.86	-1.60	-32.14	21.6	6.49	0.30
3862.59	6.86	-0.90	-32.15	35.2	6.08	0.30
CaI						
4454.79	1.90	0.26	-30.89	21.0	5.31	0.55
TiII						
3761.91 1.57	-0.52	-32.16	82.6	4.07	0.32	
CrII						
4558.65	4.07	-0.66	-32.07	42.8	4.53	0.31
MnII						
4260.47	1.85	-4.25	-32.51	19.2	6.11	0.31
FeI						
3765.55	3.24	0.48	-30.79	51.6	6.53	0.24
3767.20	1.01	-0.39	-31.76	61.8	6.04	0.24
3787.89	1.01	-0.86	-31.77	44.8	6.25	0.24
3820.44	0.86	0.12	-31.82	97.3	6.05	0.24
3821.19	3.27	0.20	-30.81	34.4	6.55	0.24
3824.45	0.00	-1.36	-32.04	69.3	6.44	0.24
3825.89	0.91	-0.04	-31.81	84.3	5.99	0.24
3827.83	1.56	0.06	-31.61	84.9	6.35	0.24
3859.92	0.00	-0.71	-32.04	93.9	6.22	0.24
3872.51	0.99	-0.93	-31.80	47.0	6.34	0.24
3878.58	0.09	-1.35	-32.03	65.0	6.42	0.24
3899.72	0.09	-1.53	-32.03	36.7	6.16	0.24
3920.27	0.12	-1.75	-32.03	28.9	6.23	0.24
3922.92	0.05	-1.65	-32.05	36.8	6.24	0.24
3927.93	0.11	-1.59	-32.04	41.1	6.29	0.24
4005.25	1.56	-0.61	-31.66	35.2	6.20	0.24
4071.75	1.61	-0.02	-31.66	54.4	5.96	0.24
4132.07	1.61	-0.68	-31.68	28.8	6.17	0.24
4187.81	2.42	-0.55	-31.41	21.5	6.44	0.24
4199.10	3.05	0.16	-31.12	25.8	6.25	0.24

$\lambda(\mathring{A})$	E.P.	log gf	log C6	log EW (m$\mathring{A}$)	log ϵ	σ_Σ
M79-0209	(Cont.)					
FeI						
4202.04	1.48	-0.71	-31.74	41.2	6.33	0.23
4250.80	1.56	-0.71	-31.73	31.2	6.22	0.23
4260.49	2.40	0.08	-31.44	23.4	5.84	0.23
4271.77	1.49	-0.16	-31.75	56.5	6.03	0.23
4325.77	1.61	0.01	-31.73	51.4	5.86	0.23
4383.56	1.48	0.20	-31.78	71.9	5.88	0.23
4404.76	1.56	-0.14	-31.76	72.5	6.29	0.23
4415.13	1.61	-0.62	-31.75	40.3	6.30	0.23
4957.61	2.81	0.23	-31.46	38.4	6.22	0.23
FeII						
3938.30	1.67	-3.89	-32.39	19.7	6.38	0.23
4178.86	2.58	-2.47	-32.33	44.3	6.04	0.23
4233.17	2.58	-2.00	-32.34	59.6	5.79	0.23
4385.39	2.78	-2.57	-32.34	45.6	6.28	0.23
4489.18	2.83	-2.97	-32.35	31.5	6.48	0.23
4508.29	2.85	-2.21	-32.35	50.2	6.04	0.23
4520.23	2.81	-2.61	-32.35	39.1	6.23	0.23
4522.64	2.84	-2.03	-32.35	50.6	5.85	0.23
4583.84	2.81	-2.02	-32.36	79.0	6.25	0.23
M79-0281						
MgI						
3829.36	2.71	-0.21	-31.04	91.5	6.47	0.31
3832.31	2.71	0.15	-31.04	142.6	7.12	0.31
MgII						
4481.14	8.86	0.73	-33.89	128.0	6.88	0.31
SiII						
3853.67	6.86	-1.60	-32.14	36.8	6.84	0.30
3856.03	6.86	-0.65	-32.14	134.9	7.64	0.30
3862.59	6.86	-0.90	-32.15	48.6	6.35	0.30
4128.10	9.83	0.31	-31.74	70.4	7.32	0.30

$\lambda(\AA)$	E.P.	log gf	log C6	log EW (m$\AA$)	log ϵ	σ_Σ
M79-0281	(Cont.)					
TiII						
3813.39	0.61	-2.02	-32.17	33.6	4.523	0.32
3900.54	1.13	-0.44	-32.11	91.3	4.21	0.32
3913.47	1.12	-0.53	-32.12	82.8	4.14	0.32
4028.35	1.89	-1.00	-32.03	47.9	4.57	0.32
4290.23	1.16	-1.12	-32.17	33.4	3.95	0.32
4300.05	1.18	-0.77	-32.17	106.2	4.82	0.32
4301.93	1.16	-1.16	-32.18	36.6	4.04	0.32
4395.04	1.08	-0.66	-32.20	65.6	3.94	0.32
4443.81	1.08	-0.71	-32.21	42.7	3.64	0.32
4468.50	1.13	-0.62	-32.20	48.5	3.67	0.32
4533.97	1.24	-0.77	-32.20	59.1	4.04	0.32
4563.77	1.22	-0.96	-32.21	37.6	3.89	0.32
CrII						
4558.65	4.07	-0.66	-32.07	59.8	5.00	0.31
MnII						
4282.49	5.52	-1.68	-32.08	37.8	6.52	0.31
FeI						
3787.89	1.01	-0.86	-31.77	48.4	6.76	0.24
3824.45	0.00	-1.36	-32.04	29.5	6.27	0.24
3827.83	1.56	0.06	-31.61	74.7	6.62	0.24
3849.98	1.01	-0.87	-31.78	56.1	6.89	0.24
3856.38	0.05	-1.29	-32.03	49.6	6.58	0.24
3872.51	0.99	-0.93	-31.80	32.4	6.54	0.24
3878.03	0.96	-0.91	-31.81	30.6	6.47	0.24
3899.72	0.09	-1.53	-32.03	42.6	6.74	0.24
3920.27	0.12	-1.75	-32.03	44.4	6.98	0.24
3922.92	0.05	-1.65	-32.05	64.9	7.16	0.24
3930.31	0.09	-1.59	-32.04	31.7	6.58	0.24
4132.07	1.61	-0.68	-31.68	35.3	6.72	0.24
4143.88	1.56	-0.51	-31.70	33.9	6.49	0.24
4202.04	1.48	-0.71	-31.74	36.6	6.69	0.24
4235.95	2.42	-0.34	-31.42	37.9	6.95	0.24
4260.49	2.40	0.08	-31.44	54.5	6.79	0.24
4271.77	1.49	-0.16	-31.75	48.0	6.34	0.24
4383.56	1.48	0.20	-31.78	64.7	6.22	0.24
4404.76	1.56	-0.14	-31.76	37.4	6.18	0.24

$\lambda(\AA)$	E.P.	log gf	log C6	log EW (m$\AA$)	log ϵ	σ_Σ
M79-0281	(Cont.)					
FeII						
4233.17	2.58	-2.00	-32.34	49.7	5.87	0.23
4303.18	2.70	-2.49	-32.34	50.4	6.44	0.23
4351.77	2.70	-2.10	-32.34	76.8	6.47	0.23
4508.29	2.85	-2.21	-32.35	35.9	6.02	0.23
4522.64	2.84	-2.03	-32.35	60.0	6.22	0.23
4923.93	2.89	-1.32	-32.40	109.4	6.43	0.23
M79-354						
HeI						
4471.50	20.97	0.05	-30.40	67.4	11.50	0.34
MgI						
3829.36	2.71	-0.21	-31.04	47.7	6.89	0.31
MgII						
4481.14	8.86	0.73	-33.89	79.1	6.18	0.31
4481.34	8.86	0.57	-33.89	136.7	7.51	0.31
SiII						
3853.67	6.86	-1.60	-32.14	74.5	7.60	0.30
4128.10	9.83	0.31	-31.74	44.0	6.71	0.30
4130.86	9.84	-0.84	-31.74	43.3	7.84	0.30
CaII						
3933.68	0.00	0.14	-33.56	95.4	3.24	0.55
TiII						
4395.04	1.08	-0.66	-32.20	49.0	4.55	0.32
4417.72	1.16	-1.43	-32.19	46.5	5.32	0.32
4443.81	1.08	-0.71	-32.21	50.3	4.62	0.32
4563.77	1.22	-0.96	-32.21	72.7	5.36	0.32
CrI						
4289.73	0.00	-0.36	-31.88	38.8	6.74	0.31

$\lambda(\AA)$	E.P.	log gf	log C6	log EW (m$\AA$)	log ϵ	σ_Σ
M79-354	(Cont.)					
FeI						
3856.38	0.05	-1.29	-32.03	52.9	7.93	0.23
4045.82	1.48	0.28	-31.70	44.0	7.00	0.23
4187.81	2.42	-0.55	-31.41	31.1	8.12	0.23
4199.10	3.05	0.16	-31.12	32.9	7.79	0.23
4383.56	1.48	0.20	-31.78	49.0	7.17	0.23
4957.61	2.81	0.23	-31.46	45.5	7.85	0.23
FeII						
3814.12	4.74	-2.41	-31.99	33.0	7.65	0.22
3918.53	5.91	-2.10	-31.83	33.9	7.99	0.22
4122.67	2.58	-3.38	-32.32	36.0	7.53	0.22
4178.86	2.58	-2.47	-32.33	57.5	7.04	0.22
4233.17	2.58	-2.00	-32.34	37.0	6.16	0.22
4416.83	2.78	-2.61	-32.34	31.5	6.78	0.22
4522.64	2.84	-2.03	-32.35	52.4	6.66	0.22
4555.89	2.83	-2.28	-32.36	41.5	6.70	0.22
M79-389						
MgII						
4481.14	8.86	0.73	-33.89	168.6	7.91	0.31
SiII						
3853.67	6.86	-1.60	-32.14	58.5	7.24	0.30
PII						
4178.46	9.64	-0.41	-31.23	44.0	7.37	0.31
TiII						
4395.04	1.08	-0.66	-32.20	57.1	4.83	0.32
4399.78	1.24	-1.27	-32.18	49.1	5.40	0.32
4443.81	1.08	-0.71	-32.21	43.0	4.64	0.32
4533.97	1.24	-0.77	-32.20	83.8	5.50	0.32
4563.77	1.22	-0.96	-32.21	42.0	4.95	0.32
4571.98	1.57	-0.52	-32.16	80.2	5.37	0.32
MnI						
4451.59	2.89	0.28	-31.09	32.2	7.35	0.30
4455.33	3.07	-0.25	-30.99	38.3	8.10	0.30

$\lambda(\AA)$	E.P.	log gf	log C6	log EW (m$\AA$)	log ϵ	σ_Σ
M79-389	(Cont.)					
FeI						
4063.60	1.56	0.06	-31.68	68.5	7.96	0.23
4383.56	1.48	0.20	-31.78	75.1	7.88	0.23
4957.61	2.81	0.23	-31.46	47.0	8.05	0.23
FeII						
4048.83	5.57	-2.47	-31.91	39.0	8.32	0.22
4178.86	2.58	-2.47	-32.33	75.2	7.45	0.22
4351.77	2.70	-2.10	-32.34	98.8	7.66	0.22
4385.39	2.78	-2.57	-32.34	75.1	7.65	0.22
4489.18	2.83	-2.97	-32.35	72.2	8.02	0.22
4491.41	2.85	-2.69	-32.34	70.1	7.71	0.22
4508.29	2.85	-2.21	-32.35	103.1	7.96	0.22
4520.23	2.81	-2.61	-32.35	76.1	7.73	0.22
4522.64	2.84	-2.03	-32.35	82.3	7.30	0.22
4541.52	2.85	-3.05	-32.35	60.3	7.89	0.22
4576.34	2.84	-2.90	-32.36	85.2	8.23	0.22
4583.84	2.81	-2.02	-32.36	129.1	8.33	0.22
4629.34	2.81	-2.38	-32.37	97.7	7.97	0.22
4635.31	5.95	-1.65	-31.94	51.8	8.01	0.22
M79-363						
MgI						
3829.36	2.71	-0.21	-31.04	76.6	6.87	0.31
4703.00	4.34	-0.47	-30.20	46.5	7.64	0.31
MgII						
4481.14	8.86	0.73	-33.89	150.2	7.41	0.31
TiII						
3900.54	1.13	-0.44	-32.11	104.6	5.00	0.32
4312.88	1.18	-1.16	-32.17	60.7	4.92	0.32
4394.07	1.22	-1.59	-32.18	47.5	5.18	0.32
4395.04	1.08	-0.66	-32.20	74.9	4.58	0.32
4399.78	1.24	-1.27	-32.18	50.3	4.91	0.32
4443.81	1.08	-0.71	-32.21	77.1	4.67	0.32
4468.50	1.13	-0.62	-32.20	70.6	4.50	0.32
4501.28	1.12	-0.75	-32.21	99.2	5.10	0.32
4533.97	1.24	-0.77	-32.20	105.8	5.32	0.32
4563.77	1.22	-0.96	-32.21	101.4	5.42	0.32

$\lambda(\AA)$	E.P.	log gf	log C6	log EW (m$\AA$)	log ϵ	σ_Σ
M79-363	(Cont.)					
MnI						
4451.59	2.89	0.28	-31.09	53.9	7.07	0.30
FeI						
3827.83	1.56	0.06	-31.61	77.6	7.40	0.23
3922.92	0.05	-1.65	-32.05	45.0	7.59	0.23
4143.88	1.56	-0.51	-31.70	68.1	7.74	0.23
4235.95	2.42	-0.34	-31.42	40.5	7.63	0.23
4250.80	1.56	-0.71	-31.73	47.8	7.60	0.23
4271.77	1.49	-0.16	-31.75	80.8	7.58	0.23
4383.56	1.48	0.20	-31.78	98.0	7.56	0.23
FeII						
4024.58	4.49	-2.48	-32.06	70.1	8.18	0.22
4128.74	2.58	-3.76	-32.32	46.3	7.92	0.22
4278.15	2.69	-3.82	-32.33	44.3	8.01	0.22
4351.77	2.70	-2.10	-32.34	110.4	7.52	0.22
4384.32	2.66	-3.50	-32.35	65.4	8.02	0.22
4385.39	2.78	-2.57	-32.34	97.6	7.77	0.22
4489.18	2.83	-2.97	-32.35	74.3	7.76	0.22
4491.41	2.85	-2.69	-32.34	92.0	7.82	0.22
4522.64	2.84	-2.03	-32.35	135.8	8.07	0.22
4541.52	2.85	-3.05	-32.35	86.5	8.07	0.22
4576.34	2.84	-2.90	-32.36	64.2	7.52	0.22
4583.84	2.81	-2.02	-32.36	112.2	7.53	0.22
4629.34	2.81	-2.38	-32.37	103.7	7.72	0.22
M79-392						
HeI						
4471.50	20.97	0.05	-30.40	68.3	10.61	0.34
MgI						
4057.51	4.34	-0.90	-29.32	17.9	8.59	0.31
MgII						
4481.34	8.86	0.57	-33.89	53.6	5.94	0.31
SiII						
4128.10	9.83	0.31	-31.74	16.4	5.76	0.30
CaII						
3968.49	0.00	-0.18	-33.56	69.4	3.93	0.55

$\lambda(\AA)$	E.P.	log gf	log C6	log EW (m$\AA$)	log ϵ	σ_Σ
M79-392	(Cont.)					
TiII						
3759.30	0.61	0.20	-32.16	53.0	4.22	0.32
3900.54	1.13	-0.44	-32.11	32.8	4.73	0.32
3913.47	1.12	-0.53	-32.12	36.8	4.90	0.32
4163.65	2.59	-0.39	-31.95	13.1	4.90	0.32
4300.05	1.18	-0.77	-32.17	19.5	4.76	0.32
4395.04	1.08	-0.66	-32.20	22.0	4.68	0.32
4443.81	1.08	-0.71	-32.21	17.2	4.59	0.32
4468.50	1.13	-0.62	-32.20	18.1	4.55	0.32
4501.28	1.12	-0.75	-32.21	19.2	4.70	0.32
4533.97	1.24	-0.77	-32.20	21.2	4.84	0.32
4571.98	1.57	-0.52	-32.16	26.4	4.89	0.32
CrII						
4242.38	3.87	-0.59	-32.05	10.3	4.55	0.31
4558.65	4.07	-0.66	-32.07	17.6	5.00	0.31
4588.20	4.07	-0.64	-32.07	21.2	5.09	0.31
MnI						
4451.59	2.89	0.28	-31.09	30.4	7.84	0.30
4455.33	3.07	-0.25	-30.99	26.3	8.36	0.30
MnII						
4282.49	5.52	-1.68	-32.08	12.5	6.38	0.30
FeI						
3758.25	0.96	-0.03	-31.77	36.7	7.67	0.23
3763.80	0.99	-0.24	-31.77	36.0	7.88	0.23
3765.55	3.24	0.48	-30.79	9.5	7.52	0.23
3787.89	1.01	-0.86	-31.77	12.6	7.90	0.23
3815.85	1.48	0.24	-31.63	33.0	7.59	0.23
3820.44	0.86	0.12	-31.82	44.6	7.63	0.23
3821.19	3.27	0.20	-30.81	13.9	8.01	0.23
3825.89	0.91	-0.04	-31.81	39.4	7.71	0.23
3827.83	1.56	0.06	-31.61	25.4	7.63	0.23
3840.45	0.99	-0.51	-31.79	12.4	7.52	0.23
3849.98	1.01	-0.87	-31.78	9.5	7.76	0.23
3872.51	0.99	-0.93	-31.80	11.6	7.91	0.23
3878.03	0.96	-0.91	-31.81	15.2	8.02	0.23
4005.25	1.56	-0.61	-31.66	18.6	8.12	0.23
4063.60	1.56	0.06	-31.68	30.3	7.74	0.23

$\lambda(\AA)$	E.P.	log gf	log C6	log EW (m$\AA$)	log ϵ	σ_Σ
M79-392	(Cont.)					
FeI						
4132.07	1.61	-0.68	-31.68	12.0	7.97	0.23
4199.10	3.05	0.16	-31.12	13.5	7.92	0.23
4202.04	1.48	-0.71	-31.74	13.4	8.00	0.23
4260.49	2.40	0.08	-31.44	13.1	7.66	0.23
4271.77	1.49	-0.16	-31.75	22.5	7.74	0.23
4383.56	1.48	0.20	-31.78	28.6	7.52	0.23
4920.51	2.83	0.07	-31.44	12.8	7.88	0.23
4957.61	2.81	0.23	-31.46	17.3	7.87	0.23
FeII						
3814.12	4.74	-2.41	-31.99	39.6	7.96	0.22
3821.94	2.34	-3.83	-32.30	24.4	7.87	0.22
3824.93	2.58	-3.40	-32.27	41.2	7.93	0.22
3906.03	5.57	-1.83	-31.88	46.1	7.94	0.22
3918.53	5.91	-2.10	-31.83	24.9	7.89	0.22
3938.30	1.67	-3.89	-32.39	41.4	7.97	0.22
3945.22	1.69	-4.25	-32.39	26.5	8.02	0.22
4002.08	2.78	-3.47	-32.28	21.3	7.65	0.22
4002.54	5.96	-1.71	-31.83	30.3	7.65	0.22
4048.83	5.57	-2.47	-31.91	28.9	8.20	0.22
4122.67	2.58	-3.38	-32.32	50.6	8.10	0.22
4124.79	2.54	-4.20	-32.33	15.2	8.07	0.22
4128.74	2.58	-3.47	-32.32	34.7	7.87	0.22
4273.33	2.70	-3.34	-32.33	31.6	7.73	0.22
4278.15	2.69	-3.82	-32.33	17.6	7.84	0.22
4296.58	2.70	-3.01	-32.33	47.8	7.73	0.22
4314.31	2.68	-3.48	-32.34	25.7	7.72	0.22
4357.58	6.09	-2.11	-31.88	22.8	7.96	0.22
4369.41	2.78	-3.66	-32.34	20.3	7.82	0.22
4384.32	2.66	-3.50	-32.35	21.2	7.62	0.22
4416.83	2.78	-2.61	-32.34	56.9	7.56	0.22
4489.18	2.83	-2.97	-32.35	40.6	7.62	0.22
4508.29	2.85	-2.31	-32.35	66.5	7.52	0.22
4580.06	2.58	-3.72	-32.39	16.8	7.68	0.22
4582.83	2.84	-3.09	-32.36	31.5	7.56	0.22
4596.02	6.23	-1.84	-31.89	27.6	7.89	0.22
4656.98	2.89	-3.61	-32.36	20.4	7.83	0.22
4666.75	2.83	-3.34	-32.37	23.8	7.62	0.22

$\lambda(\AA)$	E.P.	log gf	log C6	log EW (m$\AA$)	log ϵ	σ_Σ
M79-392	(Cont.)					
FeII						
4731.47	2.89	-3.37	-32.37	43.1	8.12	0.22
4908.15	10.33	-0.30	-30.96	15.5	8.00	0.22
4948.10	10.31	-0.32	-30.97	18.3	8.11	0.22
4948.79	10.35	-0.01	-30.96	17.0	7.77	0.22
YII						
4374.94	0.41	0.16	-32.05	14.8	3.51	0.32
4900.12	1.03	-0.09	-32.03	13.3	4.01	0.32
M79-434						
MgI						
3832.31	2.71	0.15	-31.04	52.3	7.46	0.31
MgII						
4481.14	8.86	0.73	-33.89	178.0	8.27	0.31
4481.34	8.86	0.57	-33.89	156.5	8.04	0.31
SiI						
3905.53	1.91	-1.09	-31.62	30.5	7.79	0.30
SiII						
3862.59	6.86	-0.90	-32.15	42.4	6.23	0.30
4130.86	9.84	-0.84	-31.74	43.0	7.62	0.30
CaII						
3933.68	0.00	0.14	-33.56	159.8	5.72	0.55
TiII						
3759.30	0.61	0.20	-32.16	94.0	5.20	0.32
3900.54	1.13	-0.44	-32.11	62.1	5.35	0.32
4417.72	1.16	-1.43	-32.19	53.8	6.18	0.32
4468.50	1.13	-0.62	-32.20	30.4	4.91	0.32
4501.28	1.12	-0.75	-32.21	36.4	5.15	0.32
4533.97	1.24	-0.77	-32.20	33.4	5.18	0.32
4563.77	1.22	-0.96	-32.21	44.1	5.56	0.32
4805.10	2.06	-1.12	-32.13	40.8	6.09	0.32
4911.20	3.12	-0.33	-31.98	37.2	5.78	0.32
CrII						
4616.63	4.07	-1.29	-32.08	50.6	6.39	0.31
4848.25	3.86	-1.13	-32.14	30.0	5.72	0.31

$\lambda(\AA)$	E.P.	log gf	log C6	log EW (m$\AA$)	log ϵ	σ_Σ
M79-434	(Cont.)					
FeI						
3815.85	1.48	0.24	-31.63	36.9	7.72	0.23
3821.19	3.27	0.20	-30.81	34.6	8.61	0.23
3856.38	0.05	-1.29	-32.03	45.3	8.70	0.23
3865.53	1.01	-0.98	-31.79	60.4	9.20	0.23
3899.72	0.09	-1.53	-32.03	76.4	9.66	0.23
3927.93	0.11	-1.59	-32.04	65.9	9.47	0.23
4005.25	1.56	-0.61	-31.66	46.0	8.79	0.23
4045.82	1.48	0.28	-31.70	30.4	7.54	0.23
4202.04	1.48	-0.71	-31.74	80.1	9.62	0.23
4235.95	2.42	-0.34	-31.42	39.9	8.83	0.23
4325.77	1.61	0.01	-31.73	41.3	8.10	0.23
4404.76	1.56	-0.14	-31.76	49.6	8.39	0.23
4415.13	1.61	-0.62	-31.75	34.5	8.58	0.23
4957.61	2.81	0.23	-31.46	64.8	9.02	0.23
FeII						
3938.97	5.91	-1.86	-31.83	40.9	8.03	0.22
4024.58	4.49	-2.48	-32.06	34.4	7.82	0.22
4128.74	2.58	-3.76	-32.32	32.3	8.12	0.22
4178.86	2.58	-2.47	-32.33	64.1	7.50	0.22
4233.17	2.58	-2.00	-32.34	57.7	6.89	0.22
4273.33	2.70	-3.34	-32.33	65.4	8.46	0.22
4314.31	2.68	-3.48	-32.34	37.1	8.00	0.22
4351.77	2.70	-2.10	-32.34	78.3	7.51	0.22
4385.39	2.78	-2.57	-32.34	32.3	7.03	0.22
4416.83	2.78	-2.61	-32.34	64.7	7.76	0.22
4489.18	2.83	-2.97	-32.35	64.4	8.14	0.22
4491.41	2.85	-2.69	-32.34	56.8	7.70	0.22
4508.29	2.85	-2.21	-32.35	73.0	7.59	0.22
4515.34	2.84	-2.48	-32.35	78.8	7.99	0.22
4520.23	2.81	-2.61	-32.35	33.0	7.12	0.22
4522.64	2.84	-2.03	-32.35	63.5	7.19	0.22
4541.52	2.85	-3.05	-32.35	86.0	8.73	0.22
4555.89	2.83	-2.28	-32.36	70.0	7.58	0.22

$\lambda(\AA)$	E.P.	log gf	log C6	log EW (m$\AA$)	log ϵ	σ_Σ
M79-434	(Cont.)					
FeII						
4582.83	2.84	-3.09	-32.36	51.4	7.99	0.22
4583.84	2.81	-2.02	-32.36	107.2	8.19	0.22
4596.02	6.23	-1.84	-31.89	33.0	8.03	0.22
4620.52	2.83	-3.29	-32.36	34.2	7.83	0.22
4629.34	2.81	-2.38	-32.37	47.8	7.19	0.22
4635.31	5.95	-1.65	-31.94	49.7	8.08	0.22
4656.98	2.89	-3.63	-32.36	56.0	8.65	0.22
4731.47	2.89	-3.37	-32.37	64.1	8.57	0.22
4923.93	2.89	-1.32	-32.40	73.3	6.74	0.22
4948.79	10.35	-0.01	-30.96	38.5	8.39	0.22
M79-469						
HeI						
4471.50	20.97	0.05	-30.40	43.5	9.92	0.34
MgI						
3832.31	2.71	0.15	-31.04	49.5	7.57	0.31
4057.51	4.34	-0.90	-29.32	52.4	9.46	0.31
4167.28	4.34	-0.75	-29.57	32.1	8.95	0.31
MgII						
4481.14	8.86	0.73	-33.89	105.7	6.86	0.31
4481.34	8.86	0.57	-33.89	119.2	7.31	0.31
SiII						
3853.67	6.86	-1.60	-32.14	31.3	6.70	0.30
CaII						
3933.68	0.00	0.14	-33.56	142.9	5.59	0.55
3968.49	0.00	-0.18	-33.56	139.6	5.84	0.55
TiII						
3759.30	0.61	0.20	-32.16	96.2	5.45	0.32
3900.54	1.13	-0.44	-32.11	43.4	5.13	0.32
3913.47	1.12	-0.53	-32.12	31.9	4.99	0.32
4287.88	1.08	-2.02	-32.18	32.8	6.46	0.32
4290.23	1.16	-1.12	-32.17	33.9	5.63	0.32
4301.93	1.16	-1.16	-32.18	34.6	5.68	0.32

$\lambda(\AA)$	E.P.	log gf	log C6	log EW (m$\AA$)	log ϵ	σ_Σ
M79-469	(Cont.)					
TiII						
4312.88	1.18	-1.16	-32.17	41.0	5.83	0.32
4320.96	1.16	-1.87	-32.18	59.1	6.88	0.32
4395.04	1.08	-0.66	-32.20	68.2	5.82	0.32
4399.78	1.24	-1.27	-32.18	65.8	6.45	0.32
4468.50	1.13	-0.62	-32.20	40.6	5.25	0.32
4501.28	1.12	-0.75	-32.21	45.5	5.47	0.32
4533.97	1.24	-0.77	-32.20	82.6	6.34	0.32
4563.77	1.22	-0.96	-32.21	60.1	6.02	0.32
4571.98	1.57	-0.52	-32.16	36.1	5.28	0.32
4805.10	2.06	-1.12	-32.13	32.5	6.05	0.32
CrII						
4558.65	4.07	-0.66	-32.07	32.1	5.47	0.31
4616.63	4.07	-1.29	-32.08	34.8	6.16	0.31
MnI						
4451.59	2.89	0.28	-31.09	33.0	8.09	0.31
4455.33	3.07	-0.25	-30.99	69.1	9.53	0.30
MnII						
4260.47	1.85	-4.25	-32.51	62.3	8.42	0.30
FeI						
3763.80	0.99	-0.24	-31.77	34.5	8.05	0.23
3765.55	3.24	0.48	-30.79	35.8	8.46	0.23
3767.20	1.01	-0.39	-31.76	45.0	8.43	0.23
3815.85	1.48	0.24	-31.63	39.7	7.92	0.23
3820.44	0.86	0.12	-31.82	75.7	8.57	0.23
3821.19	3.27	0.20	-30.81	49.1	9.04	0.23
3825.89	0.91	-0.04	-31.81	36.1	7.84	0.23
3849.98	1.01	-0.87	-31.78	44.0	8.89	0.23
3859.92	0.00	-0.71	-32.04	61.0	8.60	0.23
3878.03	0.96	-0.91	-31.81	57.8	9.21	0.23
3878.58	0.09	-1.35	-32.03	73.6	9.60	0.23
3899.72	0.09	-1.53	-32.03	30.6	8.81	0.23
4005.25	1.56	-0.61	-31.66	41.5	8.84	0.23
4045.82	1.48	0.28	-31.70	36.0	7.80	0.23
4063.60	1.56	0.06	-31.68	44.6	8.24	0.23
4143.88	1.56	-0.51	-31.70	44.6	8.81	0.23
4202.04	1.48	-0.71	-31.74	70.4	9.56	0.23
4260.49	2.40	0.08	-31.44	35.0	8.43	0.23

$\lambda(\AA)$	E.P.	log gf	log C6	log EW (m$\AA$)	log ϵ	σ_Σ
M79-469	(Cont.)					
FeI						
4271.77	1.49	-0.16	-31.75	40.6	8.34	0.23
4325.77	1.61	0.01	-31.73	46.7	8.36	0.23
4404.76	1.56	-0.14	-31.76	67.5	8.96	0.23
4920.51	2.83	0.07	-31.44	44.3	8.88	0.23
4957.61	2.81	0.23	-31.46	79.6	9.57	0.23
FeII						
3821.94	2.34	-3.83	-32.30	52.7	8.57	0.22
3827.08	4.73	-2.64	-31.99	34.3	8.14	0.22
3914.51	1.67	-4.05	-32.39	30.2	7.99	0.22
3938.97	5.91	-1.86	-31.83	57.6	8.46	0.22
4024.58	4.49	-2.48	-32.06	44.7	8.10	0.22
4048.83	5.57	-2.47	-31.91	33.9	8.37	0.22
4122.67	2.58	-3.38	-32.32	34.2	7.86	0.22
4128.74	2.58	-3.76	-32.32	36.0	8.27	0.22
4178.86	2.58	-2.47	-32.33	71.0	7.76	0.22
4233.17	2.58	-2.00	-32.34	78.0	7.45	0.22
4303.18	2.70	-2.49	-32.34	75.1	7.93	0.22
4351.77	2.70	-2.10	-32.34	90.8	7.93	0.22
4357.58	6.09	-2.11	-31.88	36.6	8.34	0.22
4369.41	2.78	-3.66	-32.34	36.2	8.27	0.22
4385.39	2.78	-2.57	-32.34	83.5	8.26	0.22
4489.18	2.83	-2.97	-32.35	60.9	8.14	0.22
4491.41	2.85	-2.69	-32.34	51.4	7.66	0.22
4508.29	2.85	-2.21	-32.35	99.2	8.33	0.22
4515.34	2.84	-2.48	-32.35	74.2	7.97	0.22
4520.23	2.81	-2.61	-32.35	64.1	7.85	0.22
4522.64	2.84	-2.03	-32.35	91.2	7.95	0.22
4541.52	2.85	-3.05	-32.35	30.8	7.59	0.22
4555.89	2.83	-2.28	-32.36	56.9	7.37	0.22
4582.83	2.84	-3.09	-32.36	57.7	8.20	0.22
4583.84	2.81	-2.02	-32.36	105.8	8.28	0.22
4596.02	6.23	-1.84	-31.89	77.2	9.13	0.22
4620.52	2.83	-3.29	-32.36	31.1	7.82	0.22
4629.34	2.81	-2.38	-32.37	66.5	7.67	0.22
4635.31	5.95	-1.65	-31.94	31.1	7.70	0.22
4656.98	2.89	-3.63	-32.36	43.9	8.50	0.22

$\lambda(\mathring{A})$	E.P.	log gf	log C6	log EW (m$\mathring{A}$)	log ϵ	σ_Σ
M79-469	(Cont.)					
FeII						
4666.75	2.83	-3.34	-32.37	42.0	8.11	0.22
4913.29	10.29	0.01	-30.97	31.6	8.16	0.22
4923.93	2.89	-1.32	-32.40	72.4	6.81	0.22
4948.79	10.35	-0.01	-30.96	36.8	8.35	0.22
M79-535						
HeI						
4120.81	20.97	-1.48	-30.10	44.2	10.46	0.34
MgI						
3832.31	2.71	0.15	-31.04	55.1	8.83	0.31
MgII						
4481.14	8.86	0.73	-33.89	124.0	7.71	0.31
SiII						
3853.67	6.86	-1.60	-32.14	53.4	7.32	0.30
3856.03	6.86	-0.65	-32.14	88.7	7.14	0.30
3862.59	6.86	-0.90	-32.15	78.5	7.16	0.30
4128.10	9.83	0.31	-31.74	79.3	7.24	0.30
4130.86	9.84	-0.84	-31.74	82.1	8.45	0.30
TiII						
3759.30	0.61	0.20	-32.16	40.4	5.13	0.32
FeI						
3815.85	1.48	0.24	-31.63	35.9	8.99	0.23
4132.07	1.61	-0.68	-31.68	14.4	9.36	0.23
4143.88	1.56	-0.51	-31.70	28.1	9.58	0.23
4187.81	2.42	-0.55	-31.41	26.0	9.93	0.23
FeII						
4233.17	2.58	-2.00	-32.34	55.2	7.60	0.22
4520.23	2.81	-2.61	-32.35	53.2	8.26	0.22
4522.64	2.84	-2.03	-32.35	68.7	8.09	0.22
M79-489						
HeI						
4471.50	20.97	0.05	-30.40	83.7	10.26	0.34
4713.14	20.97	-1.23	-30.55	43.1	11.01	0.34
MgI						
3832.31	2.71	0.15	-31.04	63.1	8.37	0.31

$\lambda(\AA)$	E.P.	log gf	log C6	log EW (m$\AA$)	log ϵ	σ_Σ
M79-535						
MgII						
4481.14	8.86	0.73	-33.89	110.6	7.21	0.31
4481.34	8.86	0.57	-33.89	114.0	7.44	0.31
SiII						
3856.03	6.86	-0.65	-32.14	49.3	6.19	0.30
3862.59	6.86	-0.90	-32.15	65.4	6.77	0.30
4128.10	9.83	0.31	-31.74	53.2	6.65	0.30
4130.86	9.84	-0.84	-31.74	91.6	8.68	0.30
PII						
4178.46	9.64	-0.41	-31.23	30.7	6.76	0.31
CaI						
4454.79	1.90	0.26	-30.89	150.7	12.35	0.55
CaII						
3933.68	0.00	0.14	-33.56	134.2	6.02	0.55
3968.49	0.00	-0.18	-33.56	48.0	4.24	0.55
TiII						
3759.30	0.61	0.20	-32.16	88.3	5.85	0.32
4571.98	1.57	-0.52	-32.16	33.0	5.67	0.32
4911.20	3.12	-0.33	-31.98	37.3	6.32	0.32
CrII						
4588.20	4.07	-0.64	-32.07	85.0	7.08	0.31
MnI						
4451.59	2.89	0.28	-31.09	53.7	9.14	0.30
4455.33	3.07	-0.25	-30.99	83.9	10.63	0.30
MnII						
4260.47	1.85	-4.25	-32.51	30.5	8.13	0.30
FeI						
3758.25	0.96	-0.03	-31.77	118.6	10.73	0.23
3899.72	0.09	-1.53	-32.03	60.1	10.09	0.23
3930.31	0.09	-1.59	-32.04	54.7	9.99	0.23
4260.49	2.40	0.08	-31.44	30.5	8.82	0.23
4404.76	1.56	-0.14	-31.76	40.5	8.89	0.23
FeII						
4128.74	2.58	-3.76	-32.32	32.6	8.47	0.22
4178.86	2.58	-2.47	-32.33	46.1	7.49	0.22
4233.17	2.58	-2.00	-32.34	68.8	7.57	0.22
4303.18	2.70	-2.49	-32.34	49.8	7.65	0.22

$\lambda(\AA)$	E.P.	log gf	log C6	log EW (m$\AA$)	log ϵ	σ_Σ
M79-535	(Cont.)					
FeII						
4351.77	2.70	-2.10	-32.34	51.7	7.30	0.22
4385.39	2.78	-2.57	-32.34	50.7	7.79	0.22
4489.18	2.83	-2.97	-32.35	36.0	7.87	0.22
4508.29	2.85	-2.21	-32.35	46.2	7.36	0.22
4515.34	2.84	-2.48	-32.35	66.3	8.12	0.22
4520.23	2.81	-2.61	-32.35	41.6	7.63	0.22
4522.64	2.84	-2.03	-32.35	64.0	7.60	0.22
4541.52	2.85	-3.05	-32.35	31.8	7.87	0.22
4555.89	2.83	-2.28	-32.36	58.3	7.70	0.22
4582.83	2.84	-3.09	-32.36	35.6	7.99	0.22
4583.84	2.81	-2.02	-32.36	48.9	7.21	0.22
4596.02	6.23	-1.84	-31.89	45.3	8.53	0.22
4629.34	2.81	-2.38	-32.37	35.1	7.26	0.22
4635.31	5.95	-1.65	-31.94	57.8	8.52	0.22
4913.29	10.29	0.01	-30.97	37.8	8.37	0.22
4923.93	2.89	-1.32	-32.40	64.5	6.95	0.22
4948.79	10.35	-0.01	-30.96	38.6	8.44	0.22

TABLE 8.1— Abundance measurements for target stars. Column 1 : line wavelength. Column 2 : excitation potential. Column 3 : oscillator strength. Column 4 : constant for the Unsöld formula. Column 5 : equivalent width (m$\AA$). Column 6 : element abundance. Column 7 : composite error= $\sigma^2_{log\epsilon}(\Delta W) + \sigma^2_{log\epsilon}(\Delta T) + \sigma^2_{log\epsilon}(\Delta g) + \sigma^2_{log\epsilon}(\Delta \xi) + \sigma^2_{log\epsilon}(\Delta z)$

Bibliography

Arp H. C., 1955, AJ, 60, 317

Bailyn, C. 1995, ARA&A, 33, 133

Bailyn, C. D., Sarajedini, A., Cohn, H., Lugger, P., & Grindlay, J. E. 1992, AJ, 103, 1564

Bard, A., Kock, M., 1994, A&A, 282,1014

Barnard E. E., 1900, ApJ, 12, 176

Baschek, B., 1975, Problems in stellar atmospheres and envelopes, New York, Springer-Verlag, 101

Bedin, L. R., Piotto, G., Zoccali, M., Stetson, P.B., Saviane, I., Cassisi, S., & Bono, G. 2000, A&A, 363, 159

Behr, B.B., Cohen, J. G., McCarthy, J. K., & Djorgovski, S. G. 1999, ApJ, 517,L31

Behr, B.B.,Djorgovski, S. G., Cohen, J. G., McCarthy, J. K., Côté, P., Piotto, G., & Zoccali, M. 2000, ApJ, 528, 849 [B00a]

Behr, B.B., Cohen, J. G., & McCarthy, J. K. 2000b, ApJ, 531,L37 [B00b]

Behr, B. B., 2002, private communication.

Benz, W., & Mayor, M. 1984, A&A, 138, 183

Bertola, F., Capaccioli, M., Holm, A. V., Oke, J. B., 1980, ApJ, 237L, 65

Bidelman, W. P., 1960, PASP, 72, 24

Biemont, E., Baudoux, M., Kurucz, R. L., Ansbacher, W., Pinnington, E. H., 1991, A&A, 249, 539

Bono, G., Caputo, F., Cassisi, S., Marconi, M., Piersanti, L. & Tornambe, A., 2000, ApJ, 543, 955.

Bragalia et al. 2001, AJ, 121, 327.

Brocato, E., Cassisi, S., Castellani, V., 1998, MNRAS, 295, 711

Brocato, E., Castellani, V., Raimondo, G., & Walker, A. 1999, ApJ, 527, 230

Brown, T. M., Ferguson, H. C., Davidsen, A. F., & Dorman, B. 1997, ApJ, 482, 685

Brown, T.M., Bowers, C.W., Kimble, R.A., & Ferguson, H.C., 2000, ApJ, 529, L89

Brown, T.M., Sweigart, A.V., Lanz, T., Landsman, W.B., Hubeny, I., 2001, ApJ, 562, 368

Buonanno R., Corsi C. E., Fusi Pecci F., 1985, AAP, 145, 97

Buonanno, R., Corsi, C. E., Buzzoni, A., Cacciari, C., Ferraro, F. R., & Fusi Pecci, F. 1994, A&A, 290, 69

Buonanno, R., Corsi, C. E., Bellazzini, M., Ferraro, F. R., & Fusi Pecci, F. 1997, AJ, 113, 706

Burstein, D., Bertola, F., Buson, L. M., Faber, S. M., & Lauer, T. R. 1988, ApJ, 328, 440

Caloi V., 1972, A&A, 20, 357

Caloi, V. 1999, A&A, 343, 904

Caloi V., 2001, A&A, 366, 91

Caputo et al. 1999, MNRAS, 306, 815

Carney, B. W., 1996, PASP, 108, 900

Carretta, E.; Gratton, R. G., 1997, A&AS, 121, 95

Carretta, E., Gratton, R., Clementini, G., & Fusi Pecci, F. 2000, ApJ, 533, 215

Cassisi, S. & Salaris, M. 1996, A&A, 305, 858

Cassisi, S., Castellani, V., Degl'Innocenti, S., Piotto, G., & Salaris, M. 2001, A&A, 366, 578

Cassisi, S. & Salaris, M. 1997, MNRAS, 285, 593

Cassisi, S., Castellani, V., degl'Innocenti, S., Salaris, M., & Weiss, A. 1999, A&As, 134, 103

Castelli, F., Gratton, R. G., & Kurucz, R. L. 1997, A&A, 324, 432

Catelan, M.,Sweigart, A. V., & Borissova, J. 1998, ASP Conference Series #135, p. 41.

Cayrel, R., 1988, proceedings of the 132nd Symposium of the International Astronomical Union, Paris, France, Kluwer Academic Publishers, Dordrecht, p.345

Charbonneau, P., & Michaud, G. 1988, ApJ, 327, 809

Charbonnel, C., Denissenkov, P. A., & Weiss, A. 2000, in The Galactic Halo: From Globular Clusters to Field Stars, Proc. 35th Lige International Astrophysical Colloq., ed. A. Noels, P. Magain, D. Caro, E. Jehin, G. Parmentier, & A. Thoul (Lige: IAP), 453

Code, A. D., & Welch, G. A. 1979, ApJ, 228, 95

Cohen, J. G., & Gillett, F. C. 1989, ApJ, 346, 803

Cohen, J. G., & McCarthy, J. K. 1997, AJ, 113, 1353

Cool, A. M., Grindlay, J. E., Cohn, H. N., Lugger, P. M., & Bailyn, C. D. 1998, ApJ, 508, L75

Cool, A. M., Piotto, G., & King, I. R. 1996, ApJ, 468, 655

Cottrell, P. L.& Da Costa, G. S., 1981, ApJL, 245,79

Crocker, D. A., Rood, R. T., & O'Connell, R. W. 1988, ApJ, 332, 236

D'Antona, F., Caloi, V., Montalbn, J., Ventura, P., Gratton, R., 2002, A&A, 395, 69.

D'Cruz, N. L., Dorman, B., Rood, R. T. & O'Connell, R. W. 1996,ApJ, 466, 359

de Boer, K. S., Schmidt, J. H. K., Heber, U., 1995, A&A, 303, 95.

Dekker, H., D'Odorico, S., Kaufer, A., Delabre, B., & Kotslowski, H, 2000, Proc. SPIE 4008

Dixon, W. V., Davidsen, A. F., Dorman, B., & Ferguson, H. C. 1996, AJ, 111, 1936

Dixon, W. V., Davidsen, A. F., & Ferguson, H. C. 1994, AJ, 107, 1388

Djorgovski S., 1991, in The formation and evolution of star clusters (A93-48676 20-90), p. 112-119.

Djorgovski S., 1993, ASP Conf. Ser. 50, 373.

Djorgovski S. & Meylan, G., 1994, AJ, 108, 1292

Dolphin, A.E. 2000, PASP, 112, 1397

Dorman, B. 1997, in ASP Conf. Ser. 116, The Nature of Elliptical Galaxies (2d Stromlo Symp.), ed. M. Arnaboldi, G. S. Da Costa, & P. Saha (San Francisco: ASP), 195

Dorman, B., Lee, Y.-W., & VandenBerg, D. A. 1991, ApJ, 366, 115

Dorman, B., O'Connell, R. W., & Rood, R. T. 1995, ApJ, 442, 105

Dorman, B., Rood, R. T., & O'Connell, W. O. 1993, ApJ, 419, 596

Dreizler, S., & Wolff, B. 1999, A&A, 348, 189

Dubath, P., Meylan, G., Mayor, M. et al. 1990, A&A, 239, 142

Fabbian, D., 2002, graduate thesis at the Astronomy Department of the Padova University (Italy).

Fall S., Rees M. J., 1985, ApJ, 298, 18.

Faulkner J., 1966, ApJ, 144, 978

Ferraro et al. 1997, ApJL, 484, L145

Ferraro, F. R., Paltrinieri, B., Fusi Pecci, F., Rood, R. T., & Dorman, B. 1998,ApJ, 500, 311 [F98]

Fontaine, G., & Chayer, P. 1997, in 3d Conf. on Faint Blue Stars, ed. A. G. D. Philip, J.

Fusi Pecci, F., Ferraro, F. R., Bellazzini, M., Djorgovski, S., Piotto, G., & Buonanno, R. 1993, ApJ, 105, 1145

Fusi Pecci, F., Ferraro, F. R., & Cacciari, C. 1993, in ASP Conf. Ser. 50, p. 217

Fusi Pecci, F., Bellazzini, M., Cacciari, C., Ferraro, F. R., 1995, AJ, 110, 1664

Gilliland, R., et al. 2000,ApJ , 545, 47

Gingold R. A., 1976, ApJ, 204, 116

Glaspey, J. W., Demers, S., Moffat, A. F. J., & Shara, M. 1985, ApJ, 289, 326

Glaspey, J. W., Demers, S., Moffat, A. F. J., & Michaud, G. 1986, PASP, 98, 1123

Glaspey, J.W., Michaud, G., Moffat, A. F. J. & Demers, S., 1989, ApJ, 339, 926

Gonzalez, G., Laws, C., 2000, AJ, 119, 390

Gonzalez, J.-F., LeBlanc, F., Artru, M.-C., Michaud, G., 1995,A&A, 297, 223

Graham, J. A., & Doremus, C. 1966, AJ, 73, 226

Gratton, R. G., et al. 2001, A&A, 369, 87

Gratton, R. G., 2002, private communication.

Greggio, L., & Renzini, A. 1990, ApJ, 364, 35

Greggio, L., & Renzini, A. 1999, Mem. Soc. Astron. Italiana, 70, 691

Grevesse, N. & Sauval, A. J, 1998, Space Science Reviews, 85, 161

Greenstein, G.S., Truran, J.W., & Cameron, A.G.W. 1967, Nature, 213, 871

Greenstein J. L., 1971, in IAU Symp. 42, White Dwarfs, ed. W. J. Luyten (Dordrecht:Reidel), 46

Grundahl, F., Vandenberg, D. A. & Andersen, M. I., 1998, ApJL, 500,179

Grundahl, F., Catelan, M., Landsman, W. B., Stetson, P. B., & Andersen, M. I. 1999,ApJ , 524, 242 [G99]

Hambly, N. C., Rolleston, W. R. J., Keenan, F. P., Dufton, P. L., Saffer, R. A., 1997, ApJS, 111, 419

Harris, H. C., Nemec, J. M., & Hesser, J. E. 1983, PASP, 95, 256

Harris, W.E., 1996, AJ, 112, 1487

Heber, U. 1986, A&A, 155, 33

Heber, U. 1987, IAU Colloq. 95: Second Conference on Faint Blue Stars, 79

Heber, U., Hunger, K., Jonas, G., & Kudritzki, R. P. 1984, A&A, 130, 119

Heber, U., Maxted, P. F. L., Marsh, T. R., Knigge, C., & Drew, J. 2002, Workshop on Stellar Atmosphere Modeling, Abstracts from a conference held 8-12 April 2002 in Tuebingen, Germany. Editors: I. Hubeny, D. Mihalas, K. Werner. To be published in the ASP Conference Series, 2003.

Heise, C. & Kock, M., 1990, A&A, 230, 244

Hill, R. S., Cheng, K. P., Smith, E. P., Hintzen, P. M. N., Bohlin, R. C., & O'Connell, R. W. 1996,AJ, 112,2909

Holtzman, J.A., Burrows, C.J., Casertano, S. et al. 1995, PASP, 107, 1065

Hoyle F., Schwarzschild M., 1955, ApJS, 2, 1

Hui-Bon-Hoa, A., LeBlanc, F., & Hauschildt, P. 2000, ApJ, 535, L43

Hut P., McMillan S., Goodman J., Mateo M., Phinney E. S., Pryor C., Richer, H. B, Verbunt F., Weinberg M., 1992, PASP, 104, 981.

Ibata, R. A., Gilmore, G., Irwin, M. J., 1994, Nature, 370, 194

Iben I. Jr., Rood R. T., 1970, ApJ, 161, 587

Iben, I., Jr., & Tutukov, A. V., 1984, ApJS, 54, 335

Iben, I., Jr., & Tutukov, A. V., 1993, ApJ, 418, 343

Kaluzny, J., & Udalski, A. 1992, Acta Astron., 42, 29

King, I. R., 2002, ISBN 5-354-00163-3

Kraft, R. P. 1994, PASP, 106, 553

Kraft, R. P., Sneden, C., Smith, G. H., Shetrone, M. D., Langer, G. E., & Pilachowski, C. A. 1997, AJ, 113, 279

Kurucz, R. L. 1992, in IAU Symp. 149, The Stellar Populations of Galaxies, ed. B. Barbuy & A. Renzini (Dordrecht: Kluwer), 225

Kurucz R. L., 1998, Highlights in Astronomy, 11, 646.

Kurucz R. L. & Bell, B., 1995, Atomic Line Data, Kurucz CD-ROM No. 23. Cambridge, Mass.: Smithsonian Astrophysical Observatory.

Lambert, D. L., McWilliam, A., & Smith, V. V. 1992, ApJ, 386, 685

Landolt, A. U. 1992, AJ, 104, 372

Landsman, W. B., Bohlin, R. C., Neff, S. G., O'Connell, R. W., Roberts, M. S., Smith, A. M., & Stecher, T. P. 1998, AJ, 116, 789

Landsman, W. B., Sweigart, A. V., Bohlin, R. C., Neff, S. G., O'Connell, R. W., Roberts, M. S., Smith, A. M., & Stecher, T. P. 1996, ApJ, 472, L93

Layden, A. C., Ritter, L. A., Welch, D. L., Webb, T. M. A., 1999, AJ, 117, 1313.

Lee, Y.-W., Demarque, P., & Zinn, R. 1994, ApJ, 423, 248

Lynden-Bell, D., Lynden-Bell, R. M., 1995, MNRAS, 275, 429

Livio, M., Soker, N., 2002, ApJ, 571L, 161

Liebert, J., Saffer, R. A., & Green, E. M. 1994, AJ, 107, 1408

Maxted, P. F. L., Heber, U., Marsh, T. R., North, R. C., 2001, MNRAS, 326, 1391

Melo, C. H. F., Pasquini, L. & De Medeiros, J. R 2001, A&A, 375, 851

Mengel, J.G., & Gross, P.G. 1976, APSS, 41, 407

Michaud, G., Vauclair, G., & Vauclair, S. 1983, ApJ, 267, 256 [M83]

Michaud, G. & Charland, Y. 1986, ApJ, 311, 326

Mihalas, D. M. 1966, ApJS, 13, 1

Moehler, S. 1999, Rev. Mod. Astron., 12, 281

Moehler, S., Heber, U., & de Boer, K. S. 1990, A&A, 239, 265

Moehler, S., Heber, U., & de Boer, K. S. 1994, in Hot Stars in the Halo, ed. S. J. Adelman, A. Upgren, & C. J. Adelman (Cambridge: Cambridge Univ. Press), 217

Moehler, S., Heber, U., & de Boer, K. S. 1995, A&A, 294, 65

Moehler, S., Heber, U., & Durrell, P. 1997, A&A, 317, L83

Moehler, S., Landsman, W., & Napiwotzki, R. 1998, A&A, 335, 510

Moehler, S., Heber, U., Napiwotzki, R., Koester, D., & Renzini, A. 2000a, A&A, 354, L7

Moehler, S., Heber, U., & Rupprecht, G. 1997, A&A, 319, 109

Moehler, S., Landsman, W., & Dorman, B. 2000, A&A, 361, 937

Moehler, S., Landsman, W., & Napiwotzki, R. 1998b, A&A, 335, 510

Moehler, S., Sweigart, A. V., & Catelan, M. 1999, A&A, 351, 519

Moehler, S., Sweigart, A. V., Landsman, W., & Heber, U. 2000c, A&A, 360, 120

Moehler, S., Landsman, W., & Napiwotzki, R. 1998, A&A, 335, 510

Moehler, S., Sweigart, A.V., Landsman, W. B. & Heber, U., 2000, A&A, 360, 120

Moehler S., 2001, PASP, 113, 1162

Momany, Y., Piotto, G., Recio-Blanco, A., Bedin, L. R., Cassisi, S., Bono, G., 2002, ApJ, 576L, 65

Momany et al. 2003, in preparation.

Moore, Charlotte E., Minnaert, M. G. J., Houtgast, J., 1966, National Bureau of Standards Monograph, Washington: US Government Printing Office (USGPO)

Newell, E. B. 1973, ApJs, 26, 37

Penny, A. J. & Dickens, R. J. 1986, MNRAS, 220, 845

Peterson, R. C. 1983,ApJ,275,737

Peterson, R. C., 1985a, ApJ, 289, 320,

Peterson, R. C., 1985b, ApJ, 294, L35

Peterson, R. C., Rood, R. T., & Crocker, D. A. 1995,ApJ, 453; 214

Peterson, R. J., Green, E. M., Rood, R. T., Crocker, D. A., & Kraft. R. P. 2002, ASP Conf. Ser. 265, ω Centauri: A Unique Window into Astrophysics, eds. van Leewen, F., Hughes, J., and Piotto, G.

Piotto G., Sosin, C., King, I.R. et al. 1997, in Advances in Stellar Evolution, eds. R. T. Rood & A. Renzini (Cambridge: Cambridge University Press), p. 84

Piotto, G., Zoccali, M., King, I.R. et al. 1999a, AJ, 117, 264

Piotto, G., Zoccali, M., King, I.R. et al. 1999b, AJ, 118, 1737

Piotto, G., & Zoccali, M. 1999, A&A, 345, 485

Piotto, G., Rosenberg, A., Saviane, I., Aparicio, A., & Zoccali, M. 2000, The Galactic Halo : From Globular Cluster to Field Stars, 471

Piotto, G. et al. 2002, A&A, 391, 945

Pritzl, B., Smith, H. A., Catelan, M., & Sweigart, A. V. 2000, ApJ, 530, L41

Raimondo, G.; Castellani, V., Cassisi, S., Brocato, E., Piotto, G., 2002, ApJ, 569, 975.

Reid, I. N., 2002, PASP, 114, 306

Renzini, A., et al. 1996, ApJ, 465, L23

Renzini, A. 1977; in Advanced Stages in Stellar Evolution, Geneva Observatory, p.149

Rich, R. et al. 1997,ApJ , 484, L25

Rood R., 1973, ApJ, 184, 815.

Rood R. & Seitzer, P. O., 1981, I.A.U.COLL.68: 1981, p.369,

Rood, R. T., Whitney, J., & D'Cruz, N. 1997, in Advances in Stellar Evolution, ed. R. T. Rood & A. Renzini (Cambridge Univ. Press), 74

Rosenberg, A., Saviane, I., Piotto, G., Aparicio, A., 1999, AJ, 118, 2306.

Rosenberg, A., Piotto, G., Saviane, I., & Aparicio, A. 2000,A&As,144,5

Saffer, R. A., Keenan, F. P., Hambly, N. C., Dufton, P. L., & Liebert, J. 1997, ApJ, 491, 172

Saffer, R. A., Green, E. M., Bowers, T., 2001, ASP Conf. Ser. 226: 12th European Workshop on White Dwarfs, 408.

Sandage A. R., Wallerstein G., 1960, ApJ, 131, 598

Sandage, A. & Wildey, R. 1967, ApJ, 150, 469

Sargent, W. L. W., Searle, L., 1968, ApJ, 152, 443

Searle, L., 1978, Science, Volume 199, Issue 4333, pp. 1061-1062.

Seaton, M. J., 1997, MNRAS, 289, 700

Shapley H., 1915a, Contrib. Mount Wilson, 115

Shapley H., 1915b, Contrib. Mount Wilson, 116

Siess, L., Livio, M., 1999, MNRAS, 308, 1133

Silbermann, N.A., Harding, P., Madore, B.F. et al. 1996, ApJ, 470, 1

Sills, A., & Pinsonneault, M. H. 2000,ApJ , 540, 489

Simmons, G. J., Blackwell, D. E., 1982, A&A, 112, 209

Soker, N. 1998,AJ,116,1308

Soker, N., & Harpaz, A. 2000, MNRAS, 317, 861

Soker, N., Hadar, R., 2001, MNRAS, 324, 213.

Soker, Noam, Rappaport, S., Fregeau, J., 2001, ApJ, 563L,87

Sosin, C. et al. 1997, ApJl, 480, L35

Stetson, P.B. 1987, PASP, 99, 191

Stetson, P. B. 1994, PASP, 106, 250

Stetson, P. B.& Harris, W. E., 1977, AJ, 82, 954

Stetson, P. B. et al. 1995,AAS,186,0604

Suntzeff, N. B., 1981, ApJS, 47,1

Sweigart, A. V., & Gross, P. G. 1974, ApJ, 190, 101

Sweigart A. V., Mengel J. G., Demarque P., 1974, A&A, 30, 13

Sweigart, A.V., 1997a,ApJ, 474, L23.

Sweigart, A.V. 1997b, in The 3^{rd} Conference on Faint Blue Stars, eds. Philip, A.G.D., Liebert, J.W., & Saffer, R.A, p. 3

Sweigart, A. 2000, Mixing and Diffusion in Stars: Theoretical Predictions and Observational Constraints, 24th meeting of the IAU, Joint Discussion 5, August 2000, Manchester, England., 5,

Sweigart, A.V., Brown, T.M., Lanz, T., Landsmann, W.B., & Hubeny, I. 2002, astro-ph,0203063

ten Bruggencate P., 1927, Sternhaufen, (Berlin: Springer)

Thévenin, F., Charbonnel, C., de Freitas Pacheco, J. A., Idiart, T. P., Jasniewicz, G., de Laverny, P., Plez, B., 2001, A&A, 373, 905

Tolstoy, E., Gallagher, J. S., Cole, A. A., Hoessel, J. G., Saha, A., Dohm-Palmer, R. C., Skillman, E. D., Mateo, M., Hurley-Keller, D., 1998, AJ, 116, 1244

Tonry, J., & Davis, M. 1979, AJ,84,1511

Unglaub, K. & Bues, I. 2001, A&A, 374, 570

Valdes, F. G. 1998, ASP Conf. Ser. 145: Astronomical Data Analysis Software and Systems VII, 7, 53

van den Bergh S., 1967, AJ, 72, 70

Ventura, P., D'Antona, F., Mazzitelli, I., 2002, A&A, 393, 215

Vink, J.-S., de Koter, A., & Lamers, H.J.G.L.M. 2000,A&A, 362, 295

Vink, J. S. & Cassisi, S. 2002, A&A, in press, astro-ph 0207037

Walker, A. R. 1994, AJ, 108, 555

Walker, A. R. 1998, AJ, 116, 220

Walker, A. R. 2001, private communication

Yong, H., Demarque, P., Yi, S., 2000, ApJ, 539, 928.

Yoon, Suk-Jin, Lee, Young-Wook, 2002, Science, 297, 578

Zinn R., West M.J., 1984, ApJS, 55, 45

Zinn R., 1985, ApJ, 293, 424

Zoccali, M., Cassisi, S., Piotto, G., Bono, G., & Salaris, M. 1999, ApJ, 518, L49

Zoccali, M., Cassisi, S., Bono, G. et al. 2000, ApJL, 538, L289

Zoccali, M., & Piotto, G. 2000, A&A, 358, 943